UNIVERSITY OF CALIFORNIA

Los Angeles

Magnitudes, Mechanisms, and Effects from Large-scale Lacustrine Changes

A dissertation submitted in partial satisfaction of the requirements for the degree Doctor of Philosophy in Geography

by

Austin Madson

2020

ABSTRACT OF THE DISSERTATION

Magnitudes, Mechanisms, and Effects

from Large-scale Lacustrine Changes

by

Austin Madson

Doctor of Philosophy in Geography

University of California, Los Angeles, 2020

Professor Yongwei Sheng, Chair

The mechanisms, magnitudes, and the effects of large-scale lacustrine changes can vary drastically over both time and space. These changes can alter the surrounding lithosphere, the interconnected natural systems, as well as the ever-growing connections to human water use. The timing of these changes can occur over several decades, or in some extreme cases these lacustrine changes can occur intra-annually (e.g. seasonal reservoir fluxes) or inter-annually (e.g. initial reservoir impoundments). The first portion of this dissertation work examines the magnitudes and effects of these changes at the Grand Ethiopian Renaissance Dam (GERD) in Ethiopia. Here, the mechanisms behind these changes are related to direct anthropogenic impacts (e.g. dam building and riverine impoundment). To this end, I examine the elastic deformation (Chapter 1) and subsurficial stress responses (Chapter 2) to several different

impoundment and seasonal operational cycles at the GERD. Large hydrologic loads can impart notable stress on the surrounding crust and upper mantle, and, as such, I examine these stresses at the GERD and discuss the main drivers of potential reservoir triggered seismic events. The spatial patterns and amplitudes of the stress tensors and hydrologic-induced deformation are closely linked to both the size and timing of reservoir fluxes, and an improved understanding of the magnitude and extent of the stresses and deformation provides useful information to water managers in order to better understand the effects from many different impoundment and operational strategies. Lastly, this work examines the magnitude of water level changes for all waterbodies >1 km^2 within the contiguous United States (CONUS) as derived from spaceborne lidar altimeter data products (Chapter 3). Here, the mechanisms behind these changes are related to both direct and indirect anthropogenic impacts and are quite diverse across the landscape. A more thorough understanding of the spatiotemporal differences in the magnitude of these changes provides the foundation needed to appropriately assess the varying mechanisms behind, and the effects of these changes. There is a notable spatial data gap of *in situ* water level measurements within the CONUS. To that end, remote sensing analysis provides a means to fill in those data gaps in order to glean a better understanding of the spatiotemporal water level changes across the entirety of the CONUS.

The dissertation of Austin Madson is approved.

Gregory S. Okin

Yongkang Xue

An Yin

Yongwei Sheng, Committee Chair

University of California, Los Angeles

2020

For Frank

Table of Contents

List of Figures

Chapter 1

Chapter 2

Chapter 3

List of Tables

Chapter 1

Supplementary Materials

Chapter 1

Chapter 2

Acknowledgments

I'd like to thank my committee members for providing guidance over the last several years. In particular, I'd like to thank Yongwei Sheng for the mentorship he has provided me since the fall of 2013. Further, I'd like to thank all of my UCLA colleagues that I was fortunate enough to have interacted with over these years. I'd particularly like to thank them for keeping (trying) me sane and providing friendship and guidance. I'd also like to provide thanks for all of the incredible experiences I have shared with friends during my time in graduate school. Thanks go out to Frank van der Wouden (scherp!) as well as Kelley Bark for her support during these last few years. Lastly, I'd like to thank my family for their long-distance support. In particular, my Mother and Father, Rye Guy, Prep, Hewy (a.k.a. Rickety), and Pearl. Long live RPHAL.

During my graduate studies I have received financial support from UCLA Graduate Division and NASA's Surface Water and Ocean Topography (SWOT) Program, grant number NNX16AH85G.

Chapter 1 is a version of: Madson, A., & Sheng, Y., Reservoir Induced Deformation Analysis for Several Filling and Operational Scenarios at the Grand Ethiopian Renaissance Dam Impoundment*, Remote Sensing 12.11 (2020)*. https://doi.org/10.3390/rs12111886. Y. Sheng provided paper edits.

Chapter 2 is a version of: Madson, A. & Sheng, Y., Reservoir induced stress analysis for several filling and operational scenarios at the Grand Ethiopian Renaissance Dam impoundment, *under review*. Y. Sheng provided paper edits.

Chapter 3 is a version of: Madson, A. & Sheng, Y., Automated Water Level Monitoring at the Continental Scale from ICESat-2 ATLAS Photons, *in preparation*. Y. Sheng provided paper edits.

Education

AUSTIN MADSON

University of California, Los Angeles

Ph.D. Candidate, Geography. Expected degree December 2020

M.A. Geography. March 2015

B.A. Geography, *magna cum laude* with Departmental Honors. 2012
Minor: Geospatial Information Systems & Technologies

Honors/Awards/Grants/Proposals

- Principal Investigator – ASI COSMO-SkyMed Proposal ID716: Lithospheric deflection from seasonal hydrologic loading and unloading at the Three Gorges Reservoir, 2019.
- Principal Investigator – DLR TanDEM-X Proposal HYDR2283: DEMs for Hydrologic and Cryospheric Volume, 2019.
- Departmental Teaching Award Recipient: Given annually to the top TA in the department as determined by a departmental honors' committee, 2018.
- Co - Principal Investigator – XSEDE Proposal TG-EAR160041: Remote Sensing for High Resolution Landslide & Glacier Kinematic Measurements Utilizing Vast Spaceborne and Airborne Radar Datasets, 2017.
- Principal Investigator – DLR TerraSAR-X Proposal LAN3344 & LAN3340: Seasonal Landslide Flow Rate Fluctuations on the Palos Verdes Peninsula in Southern California, 2017 & Landslide Kinematic Measurements from TSX Data in Southwest Colorado, 2016.
- UCLA Graduate Summer Research Mentor Program Recipient, 2015 & 2016.
- Highly Commended Paper: The Undergraduate Awards – Agricultural and Environmental Sciences, 2012.
- Blackman Family Award Recipient: Given to graduating undergraduates in the Geography and Geography/ Environmental Studies majors with the highest GPA, 2012.

Teaching Experience

Instructor – 2 Quarters of Experience

- Geog7 – Introduction to Geographic Information Systems **(x2)**
- Geog167 – Cartography **(x1)**

Teaching Assistant/Associate/Fellow – 18 Quarters of Experience

- Geog5 – People and Earth's Ecosystems **(x2)**
- Geog7 – Introduction to Geographic Information Systems **(x1)**
- Geog169 – Satellite Remote Sensing & Imaging Geographic Information Systems **(x1)**
- Geog170 – Advanced Geographic Information Systems **(x5)**
- Geog172– Remote Sensing: Digital Image Processing & Analysis **(x1)**
- Geog173 – Geographic Information Systems Programming & Development **(x6)**
- Geog174 – Advanced Remote Sensing **(x2)**

Publications

- **Madson, A.**, & Sheng, Y., Reservoir Induced Deformation Analysis for Several Filling and Operational Scenarios at the Grand Ethiopian Renaissance Dam Impoundment*, Remote Sensing 12.11 (2020)*. https://doi.org/10.3390/rs12111886
- Yuan, T., Lee, H., Yu, H., Jung, H., **Madson, A.**, Sheng, Y., & Beighley, E. Mapping forested floodplain topography using InSAR and radar altimetry. *IEEE Journal of Selected Topics in Applied Earth Observations and Remote Sensing*, (2020).
- Gillespie, T. W., **Madson, A.**, Cusack, C. F., & Xue, Y., Changes in NDVI and human population in protected areas on the Tibetan Plateau. *Arctic, Antarctic, and Alpine Research*, *51*(1), 428-439, (2019).
- **Madson, A.**, Fielding, E., Cavanaugh, K., Sheng, Y., High-resolution spaceborne, airborne, and in situ landslide kinematic measurements of the Slumgullion Landslide in Southwest Colorado. *Remote Sensing 11.3 (2019)*. https://doi.org/10.3390/rs11030265
- Sheng, Y., **Madson, A.**, Song, C., 2.02 GIS for Paleo-limnological studies, In Comprehensive Geographical Information Systems, edited by Bo Huang, Elsevier, Oxford, (2018), Pages 28-36, ISBN 9780128047934, https://doi.org/10.1016/B978-0-12-409548-9.09632-9.
- **Madson, A.**, Sheng, Y., Song, C., ICESat-derived lithospheric flexure as caused by an endorheic lake's expansion on the Tibetan Plateau and the comparison to modeled flexural responses. *Journal of Asian Earth Sciences,* (2017). https://doi.org/10.1016/j.jseaes.2017.08.028
- Song, C., Sheng, Y., Wang, J., Ke, L., **Madson, A.**, & Nie, Y. Heterogeneous glacial lake changes and links of lake expansions to the rapid thinning of adjacent glacier termini in the Himalayas. *Geomorphology*, (2017) pp. 280, 30-38. https://doi.org/10.1016/j.geomorph.2016.12.002

Presentations

- **Madson, A**., Low-cost landslide GNSS monitors and a ground-based all-wheel drive rover for precise surface elevation transects. *American Geophysical Union*, 2019 Fall Meeting, San Francisco, CA.
- **Madson, A**., A comparison of several of the latest high-resolution spaceborne, airborne, and in situ landslide kinematic measurement techniques utilizing the Slumgullion Earthflow Natural Laboratory in Southwest Colorado. *American Geophysical Union*, 2016 Fall Meeting, San Francisco, CA.
- **Madson, A**., ICESat derived crustal flexure as caused by the expansion of an endorheic lake on the Tibetan Plateau. *American Geophysical Union*, 2015 Fall Meeting, San Francisco, CA.
- **Madson, A**., Barron, S., Sehler, R., Sacramento-San Joaquin Delta disasters and water wesources: NASA radar remote sensing for levee health assessment. *Association of American Geographers*, 2013 Annual Meeting, Los Angeles, CA.
- **Madson, A**., RADAR Love – NASA DEVELOP students utilize airborne radar data for a variety of uses. 2012, *Ignite@AGU*, Infusion Lounge, San Francisco, CA
- **Madson, A**., Laygo, K., Gorelik. S., Central US disasters: visualizing the New Madrid Earthquake Seismic Zone for improved hazard assessments. 2012, *NASA DEVELOP Closeout Featured Presentation Session*, NASA Headquarters, Washington D.C.

Introduction

A complete understanding of the magnitudes of large-scale lacustrine changes is required in order to properly determine how the complex mechanisms affect those magnitudes of change as well as how the effects from those magnitudes vary over different scenarios. Quantifying these magnitudes of change requires a combination of unique approaches and is well suited towards modern-day remote sensing methodologies and techniques. Similarly, the different effects from these lacustrine changes, along with their complex mechanisms, are well suited to these techniques and methodologies. A combination of products derived from both *in situ* data and remotely sensed spaceborne datasets coupled with modern modeling and computational capabilities provide the means to meaningfully deduce the different connections between the vastly different magnitudes, mechanisms, and effects of large-scale lacustrine changes. To this end, this brief introductory chapter describes the motivation behind the three substantive chapters of this document. This work entails the utilization of remote sensing datasets from spaceborne optical sensors and lidar altimeters, *in situ* water level measurements, and localized Earth models. These datasets and processing/modeling techniques help to provide a more complete picture of the diverse connections between the magnitudes, mechanisms, and effects of large-scale lacustrine changes.

River impoundments are notable examples of large lacustrine changes, and these hydrological engineering projects can have a multitude of different impacts on the hydrosphere and lithosphere. For one, seasonal discharge curves can be severely altered, and this can have dramatic impacts on downstream hydrological conditions and

human water use. Further, this can allow for better control of flood and drought events. These impoundments can also have a dramatic impact on downstream hydrologic engineering projects. For example, three projects downstream of the Grand Ethiopian Renaissance Dam (GERD) in Ethiopia (Rosaries, Sennar, and Aswan High) will need to adjust their release operations in order to maintain Sudanese agricultural water supplies [1]. Downstream hydrologic power generation could possibly be affected by the filling and operation of an impoundment, and the potential reduction in power generation is related to the filling and operational scenarios that the project's water managers decide upon [1-3].

Groundwater levels can also be impacted by large-scale impoundments and their subsequent reservoir operations. To this end, reservoirs can provide seepage into the subsurficial rock and connected aquifer systems. This diffusion of water into the underlying rock is capable of increasing pore pressure and reducing frictional stresses. Further, impoundment and operational strategies of large dams (e.g., Three Gorges) have been shown to directly alter groundwater levels for hydraulically connected aquifer systems [4, 5]. These connections are capable of decreasing slope stability and can trigger slope failure events as caused by the changes in hydrostatic pressure due to the varying levels in the groundwater and the hydraulically connected reservoir levels [6-9].

Additional impacts from these impoundments are associated with the large hydrologic loading forces applied on the reservoir-adjacent lithosphere. Extreme changes in surface loads caused by large hydro-engineering projects (e.g. the Aswan High Dam in Egypt and the Three Gorges Reservoir in China) can have far reaching implications for increased stress and strain on surrounding fault systems and

subsequent seismicity [10-15]. These marked changes in hydrologic loads impart large forces on the surface of the Earth and are capable of deforming the lithosphere [16]. For example, several studies have shown that remotely sensed and *in situ* products (e.g. InSAR, GNSS, GRACE, etc.) have the capability to quantify the flexural response from changes in hydrologic loads (drought, lakes, regional climatic changes, reservoirs, seasonal precipitation, snow, etc.) [17-24]. Large-scale impoundment projects allow for a marked influx of water into the upstream reservoir area during the initial impoundment stages as well as during normal seasonal hydro-operations. These hydrologic loads are highly dependent on the filling and operational strategies that are selected by the local/regional water managers. The amplitude and extent of the flexural response and subsurficial stresses are mostly dependent on the underlying rheology as well as the timing and amount of the hydrologic forcing. Both the early filling stages and the subsequent operational scenarios play important roles in the application of hydrologic load induced lithospheric deformation and stress for large impoundments.

Drastic influxes of water into a reservoir can apply large stresses on the region as well as significantly increase the pore pressure in the surrounding areas [25]. Dozens of cases of post-impounding seismicity have been researched over the last several decades, and these topics are a concern for large-scale impoundments [26-38]. However, understanding these reservoir triggered seismic (RTS) events is not straightforward. For example, in some cases the increased RTS activity occurs during the filling stages, while other large reservoir projects have documented increases only after an impoundment is complete and several seasonal operational phase cycles have been completed [11, 39]. There are two dominant mechanisms responsible for RTS: (1)

increased normal and shear stress from the elastic response to the hydrologic loading and/or unloading and (2) increased pore pressure from a reduction in effective normal stresses [11, 27, 34, 39-41]. However, the stress changes from the elastic response can also be a stabilizing factor for the underlying and reservoir-adjacent regions, but this is dependent on the overall geometry of the impoundment relative to nearby faults as well as the preexisting stressors in the study area [38, 42].

The first and second chapters seek to provide a first look at the modeled vertical (subsidence and uplift) and horizontal displacement as well as the Coulomb stress on optimal fault orientations brought on by the GERD impoundment and seasonal operation. This work was undertaken in order to glean a better understanding of the amplitude and spatiotemporal dynamics of the load-induced flexural response and subsurficial stresses at and around the GERD study site. I utilize digital surface models (DSMs) and hydrologic inputs from several filling and operational scenarios along with a localized Earth model to compute the elastic displacements as well as to calculate the Coulomb stresses on optimal planes in a 3D elastic half-space in order to satisfy those goals.

A more thorough understanding of the spatiotemporal differences in the magnitude of lacustrine changes provides the foundation needed to appropriately assess the varying mechanisms behind, and the effects of these changes. In the third chapter, the mechanisms behind these changes are related to both direct and indirect anthropogenic impacts and are quite diverse across the landscape. To this end, monitoring changes in lake and reservoir water levels are of a benefit to both local and regional water managers so that they may make more informed decisions about water

management policies. This is especially true at the continental scale where the spatiotemporal changes in water levels are notably diverse across the landscape [43, 44]. That said, continental scale monitoring of lake and reservoir water level changes is particularly difficult to accomplish solely by the utilization of *in situ* water level gages. This statement holds true for countries that have a meaningful *in situ* gaging and monitoring system in place. The United States and the United States Geological Survey's (USGS) National Water Information System (NWIS) is a notable example. There is a stark need to utilize other methodologies and datasets for monitoring water level changes in the contiguous United States (CONUS).

Remote sensing techniques have been used for many years to augment the use of *in situ* surface water level and storage measurements [45, 46]. For example, [47] used early spaceborne radar altimetry data from the United States Navy's Geosat platform to monitor temporal changes in water levels within large lakes and inland seas. Further, more recent work utilizes a multi-platform approach for longer temporal scale lake level and storage changes [48-51] at notably larger spatial scales. However, most spaceborne altimeters are limited in their ability to meaningfully resolve water level changes for a large quantity of lakes. This is mostly due to spatial and temporal gaps in data coverage as well as the ground footprint size of the altimeter's energy source. The latter is especially true for radar altimeter platforms (e.g. Topex/Poseidon's ~1 km footprint). Spaceborne laser altimeters (like NASA's first ICESat mission) have notably smaller footprint diameters (~70 m) in comparison to their radar altimeter counterparts. The reduced footprint size of the altimeter allows for water level changes to be derived for waterbodies with smaller areal extents. This of course increases the number of lakes

and reservoirs where meaningful measurements can be acquired and allows for a more complete picture of surface water changes. Several researchers have successfully utilized highly accurate ICESat laser altimetry products to monitor water level and storage changes over the period of the sensor's lifetime [21, 52-54].

Recently, more water level and storage analyses have begun to utilize ICESat-2 (IS-2) ATLAS datasets into their studies. For example, [55, 56] employ IS-2 ATLAS products to accurately monitor water level and storage changes for ~3,700 global reservoirs and for several lakes on the Tibetan Plateau (TP), respectively. [56] note that utilizing IS-2 data increases the quantity of measurable lakes on the TP by a factor of two as compared to ICESat datasets. An accuracy comparison of *in situ* water level gage readings with levels derived from IS-2 and a modern spaceborne altimeter (Satellite with ARgos and ALtika - SARAL) for around 30 reservoirs in China shows that the relative altimetric accuracy from IS-2 data is nearly two decimeters better than SARAL's [57]. These studies further highlight the quality of lake and reservoir monitoring products from IS-2 data as compared to current and previous spaceborne altimeters.

The third chapter seeks to provide a novel automated workflow that utilizes the latest spaceborne altimetric products in order to monitor lake and reservoir water level changes for all waterbodies > 1 km^2 in the CONUS. An added objective of this work is to provide accuracy assessments of these remotely sensed water level products as compared to thousands of temporally and spatially overlapping water level changes from USGS gage readings. I employ careful processing techniques and cluster computing workflows along with a validated waterbody extent product and all spatially overlapping ATL03 photons for lakes and reservoirs > 1 km^2 in the CONUS along with

Landsat Dynamic Surface Water Extent (DSWE) products in order to satisfy the two goals as laid out above.

References

1. Wheeler, K.G., et al., *Cooperative filling approaches for the grand ethiopian renaissance dam.* Water international, 2016. **41**(4): p. 611-634.
2. Sharaky, A.M., K.H. Hamed, and A.B. Mohamed, *Model-Based Optimization for Operating the Ethiopian Renaissance Dam on the Blue Nile River.* 2017.
3. Beyene, A., *Reflections on the Grand Ethiopian Renaissance Dam.* Horn of Africa News, 2013. **14**.
4. Zhang, L., et al., *Impact of impoundment on groundwater seepage in the Three Gorges Dam in China based on CFCs and stable isotopes.* Environmental earth sciences, 2014. **72**(11): p. 4491-4500.
5. Zhao, Y., et al., *Groundwater level prediction of landslide based on classification and regression tree.* Geodesy and Geodynamics, 2016. **7**(5): p. 348-355.
6. Paronuzzi, P., E. Rigo, and A. Bolla, *Influence of filling–drawdown cycles of the Vajont reservoir on Mt. Toc slope stability.* Geomorphology, 2013. **191**: p. 75-93.
7. Zhang, M., Y. Dong, and P. Sun, *Impact of reservoir impoundment-caused groundwater level changes on regional slope stability: a case study in the Loess Plateau of Western China.* Environmental earth sciences, 2012. **66**(6): p. 1715-1725.
8. Fredlund, D.G. and H. Rahardjo, *Soil mechanics for unsaturated soils*. 1993: John Wiley & Sons.
9. Xia, M., et al., *Relationship between landslide stability and reservoir water level variation.* Bulletin of Engineering Geology and the Environment, 2015. **74**(3): p. 909-917.

10. Allen, C.R., *Reservoir-induced earthquakes and engineering policy.* Revista Geofísica, 1980. **13**: p. 20-24.

11. Talwani, P., *On the nature of reservoir-induced seismicity*, in *Seismicity Associated with Mines, Reservoirs and Fluid Injections*. 1997, Springer. p. 473-492.

12. Kerr, R.A. and R. Stone, *A human trigger for the great quake of Sichuan?* Science, 2009. **323**(5912): p. 322-322.

13. Ge, S., et al., *Did the Zipingpu reservoir trigger the 2008 Wenchuan earthquake?* Geophysical Research Letters, 2009. **36**(20).

14. Gahalaut, K., et al., *Influence of Tehri Reservoir Impoundment on Local Seismicity of Northwest Himalaya.* Bulletin of the Seismological Society of America, 2018. **108**(5B): p. 3119-3125.

15. Chander, R. and K. Chander, *Probable influence of Tehri reservoir load on earthquakes of the Garhwal Himalaya.* Current science, 1996: p. 291-299.

16. Madson, A. and Y. Sheng, *Reservoir Induced Deformation Analysis for Several Filling and Operational Scenarios at the Grand Ethiopian Renaissance Dam Impoundment.* Remote Sensing, 2020. **12**(11): p. 1886.

17. Enzminger, T.L., E.E. Small, and A.A. Borsa, *Accuracy of snow water equivalent estimated from GPS vertical displacements: A synthetic loading case study for western US mountains.* Water Resources Research, 2018. **54**(1): p. 581-599.

18. Tregoning, P., et al., *Detecting hydrologic deformation using GRACE and GPS.* Geophysical Research Letters, 2009. **36**(15).

19. Dumka, R., et al., *GPS Measurements of Deformation Caused by Seasonal Filling and Emptying Cycles of Four Hydroelectric Reservoirs in India.* Bulletin of the Seismological Society of America, 2018. **108**(5B): p. 2955-2966.

20. Neelmeijer, J., et al., *Ground Deformations around the Toktogul Reservoir, Kyrgyzstan, from Envisat ASAR and Sentinel-1 Data—A Case Study about the Impact of Atmospheric Corrections on InSAR Time Series.* Remote Sensing, 2018. **10**(3): p. 462.

21. Madson, A., Y. Sheng, and C. Song, *ICESat-derived lithospheric flexure as caused by an endorheic lake's expansion on the Tibetan Plateau and the comparison to modeled flexural responses.* Journal of Asian Earth Sciences, 2017. **148**: p. 142-152.

22. Gahalaut, V., et al., *InSAR and GPS measurements of crustal deformation due to seasonal loading of Tehri reservoir in Garhwal Himalaya, India.* Geophysical Journal International, 2017. **209**(1): p. 425-433.

23. Borsa, A.A., D.C. Agnew, and D.R. Cayan, *Ongoing drought-induced uplift in the western United States.* Science, 2014. **345**(6204): p. 1587-1590.

24. Kraner, M.L., W.E. Holt, and A.A. Borsa, *Seasonal nontectonic loading inferred from cGPS as a potential trigger for the M6. 0 South Napa earthquake.* Journal of Geophysical Research: Solid Earth, 2018. **123**(6): p. 5300-5322.

25. Simpson, D.W., *Seismicity changes associated with reservoir loading.* Engineering Geology, 1976. **10**(2-4): p. 123-150.

26. Baisch, S., et al., *Induced seismicity during the stimulation of a geothermal HFR reservoir in the Cooper Basin, Australia.* Bulletin of the Seismological Society of America, 2006. **96**(6): p. 2242-2256.

27. Bell, M.L. and A. Nur, *Strength changes due to reservoir‐induced pore pressure and stresses and application to Lake Oroville.* Journal of Geophysical Research: Solid Earth, 1978. **83**(B9): p. 4469-4483.

28. Chen, L. and P. Talwani, *Reservoir-induced seismicity in China*, in *Seismicity Caused by Mines, Fluid Injections, Reservoirs, and Oil Extraction*. 1998, Springer. p. 133-149.

29. Gahalaut, K., V. Gahalaut, and M. Pandey, *A new case of reservoir triggered seismicity: Govind Ballav Pant reservoir (Rihand dam), central India.* Tectonophysics, 2007. **439**(1-4): p. 171-178.

30. Ghaboussi, J. and E. Wilson, *Seismic analysis of earth dam-reservoir systems.* Journal of Soil Mechanics & Foundations Div, 1973. **99**(Proc Paper 10053).

31. Gupta, H., et al., *Pore pressure studies initiated in area of reservoir‐induced earthquakes in India.* Eos, Transactions American Geophysical Union, 2000. **81**(14): p. 145-151.

32. Gupta, H.K., *A review of recent studies of triggered earthquakes by artificial water reservoirs with special emphasis on earthquakes in Koyna, India.* Earth-Science Reviews, 2002. **58**(3-4): p. 279-310.

33. Mekkawi, M., J.-R. Grasso, and P.-A. Schnegg, *A long-lasting relaxation of seismicity at Aswan reservoir, Egypt, 1982-2001.* Bulletin of the Seismological Society of America, 2004. **94**(2): p. 479-492.

34. Roeloffs, E.A., *Fault stability changes induced beneath a reservoir with cyclic variations in water level.* Journal of Geophysical Research: Solid Earth, 1988. **93**(B3): p. 2107-2124.

35. Simpson, D.W. and S.K. Negmatullaev, *Induced seismicity at Nurek reservoir, Tadjikistan, USSR.* Bulletin of the Seismological Society of America, 1981. **71**(5): p. 1561-1586.

36. Talwani, P. and S. Acree, *Pore pressure diffusion and the mechanism of reservoir-induced seismicity*, in *Earthquake Prediction*. 1985, Springer. p. 947-965.

37. Zoback, M.D. and S. Hickman, *In situ study of the physical mechanisms controlling induced seismicity at Monticello Reservoir, South Carolina.* Journal of Geophysical Research: Solid Earth, 1982. **87**(B8): p. 6959-6974.

38. Tao, W., et al., *Impoundment of the Zipingpu reservoir and triggering of the 2008 Mw 7.9 Wenchuan earthquake, China.* Journal of Geophysical Research: Solid Earth, 2015. **120**(10): p. 7033-7047.

39. Simpson, D., W. Leith, and C. Scholz, *Two types of reservoir-induced seismicity.* Bulletin of the Seismological Society of America, 1988. **78**(6): p. 2025-2040.

40. Simpson, D., *Triggered earthquakes.* Annual Review of Earth and Planetary Sciences, 1986. **14**(1): p. 21-42.

41. Snow, D. *Geodynamics of seismic reservoirs*. in *Proceedings of the symposium on percolation through fissured rocks*. 1972.

42. Rajendran, K. and P. Talwani, *The role of elastic, undrained, and drained responses in triggering earthquakes at Monticello Reservoir, South Carolina.* Bulletin of the Seismological Society of America, 1992. **82**(4): p. 1867-1888.

43. Song, C., B. Huang, and L. Ke, *Modeling and analysis of lake water storage changes on the Tibetan Plateau using multi-mission satellite data.* Remote Sensing of Environment, 2013. **135**: p. 25-35.

44. Sheng, Y., et al., *Representative lake water extent mapping at continental scales using multi-temporal Landsat-8 imagery.* Remote Sensing of Environment, 2016. **185**: p. 129-141.

45. Birkett, C., *Radar altimetry: a new concept in monitoring lake level changes.* Eos, Transactions American Geophysical Union, 1994. **75**(24): p. 273-275.

46. Birkett, C.M. and I.M. Mason, *A new global lakes database for a remote sensing program studying climatically sensitive large lakes.* Journal of Great Lakes Research, 1995. **21**(3): p. 307-318.

47. Morris, C.S. and S.K. Gill, *Variation of Great Lakes water levels derived from Geosat altimetry.* Water Resources Research, 1994. **30**(4): p. 1009-1017.

48. Birkett, C., et al., *From research to operations: The USDA global reservoir and lake monitor*, in *Coastal altimetry*. 2011, Springer. p. 19-50.

49. Crétaux, J.-F., et al., *Lake volume monitoring from space.* Surveys in Geophysics, 2016. **37**(2): p. 269-305.

50. Crétaux, J.-F., et al., *SOLS: A lake database to monitor in the Near Real Time water level and storage variations from remote sensing data.* Advances in space research, 2011. **47**(9): p. 1497-1507.

51. Duan, Z. and W. Bastiaanssen, *Estimating water volume variations in lakes and reservoirs from four operational satellite altimetry databases and satellite imagery data.* Remote Sensing of Environment, 2013. **134**: p. 403-416.

52. Song, C., et al., *Heterogeneous glacial lake changes and links of lake expansions to the rapid thinning of adjacent glacier termini in the Himalayas.* Geomorphology, 2017. **280**: p. 30-38.

53. Yuan, T., et al., *Mapping forested floodplain topography using InSAR and radar altimetry.* IEEE Journal of Selected Topics in Applied Earth Observations and Remote Sensing, 2019. **12**(12): p. 5189-5198.

54. Zhang, G., et al., *Monitoring lake level changes on the Tibetan Plateau using ICESat altimetry data (2003–2009).* Remote Sensing of Environment, 2011. **115**(7): p. 1733-1742.

55. Ryan, J.C., et al., *Global Characterization of Inland Water Reservoirs Using ICESat‐2 Altimetry and Climate Reanalysis.* Geophysical Research Letters, 2020. **47**(17): p. e2020GL088543.

56. Zhang, G., W. Chen, and H. Xie, *Tibetan Plateau's lake level and volume changes from NASA's ICESat/ICESat‐2 and Landsat Missions.* Geophysical Research Letters, 2019. **46**(22): p. 13107-13118.

57. Yuan, C., P. Gong, and Y. Bai, *Performance Assessment of ICESat-2 Laser Altimeter Data for Water-Level Measurement over Lakes and Reservoirs in China.* Remote Sensing, 2020. **12**(5): p. 770.

Chapter 1: Reservoir Induced Deformation Analysis for Several Filling and Operational Scenarios at the Grand Ethiopian Renaissance Dam Impoundment

Abstract

Addressing seasonal water uncertainties and increased power generation demand has sparked a global rise in large-scale hydropower projects. To this end, the Blue Nile impoundment behind the Grand Ethiopian Renaissance Dam (GERD) will encompass an areal extent of ~1763.3 km^2 and hold ~67.37 Gt (km^3) of water with maximum seasonal load changes of ~27.93 (41% of total)—~36.46 Gt (54% of total) during projected operational scenarios. Five different digital surface models (DSMs) are compared to spatially overlapping spaceborne altimeter products and hydrologic loads for the GERD are derived from the DSM with the least absolute elevation difference. The elastic responses to several filling and operational strategies for the GERD are modeled using a spherically symmetric, non-rotating, elastic, and isotropic (SNREI) Earth model. The maximum vertical and horizontal flexural responses from the full GERD impoundment are estimated to be 11.99 and 1.99 cm, regardless of the full impoundment period length. The vertical and horizontal displacements from the highest amplitude seasonal reservoir operational scenarios are 38–55% and 34–48% of the full deformation, respectively. The timing and rate of reservoir inflow and outflow affects the hydrologic load density on the Earth's surface, and, as such, affects not only the total elastic response but also the distance that the deformation extends from the reservoir's body. The magnitudes of the hydrologic-induced deformation are directly related to the

size and timing of reservoir fluxes, and an increased knowledge of the extent and magnitude of this deformation provides meaningful information to stakeholders to better understand the effects from many different impoundment and operational strategies.

1. Introduction

The Grand Ethiopian Renaissance Dam (GERD) on the Blue Nile is located in Ethiopia about 15 km upstream (east) of the Sudanese border and is set to be complete in the next several years [1, 2]. The initial GERD site itself was one of four identified during a survey in the 1960s by the United States Bureau of Reclamation [3]. The dam is located around 11.215° N, 35.092° E (Figure 1) and sits in the Upper Blue Nile Basin, a large watershed with an areal extent of ~175,000 km^2. The notable Ethiopian Highlands drain through the basin and into the Blue Nile, and subsequently to the GERD impoundment. Construction on the dam began in the spring of 2011, and when completed, it will be the largest dam in Africa. The main roller compacted concrete gravity dam is 150 m tall and 1800 m long and will work in unison with an adjacent rock-filled saddle dam that is ~50 m tall and 5 km long in order to increase the water level of the impoundment to approximately 640 m above mean sea level [4-6]. The entire Blue Nile River Basin contributes around 58–62% of the total water supply to downstream Nile River flows [7]. Blue Nile flow data at the Sudanese/Ethiopian border from the National Meteorological Agency of Ethiopia have a historical (1967–1972; 1999–2003) annual mean of around 50 Gt, where the vast majority (~80%) of this flow occurs in the months of July through October [2, 8, 9].

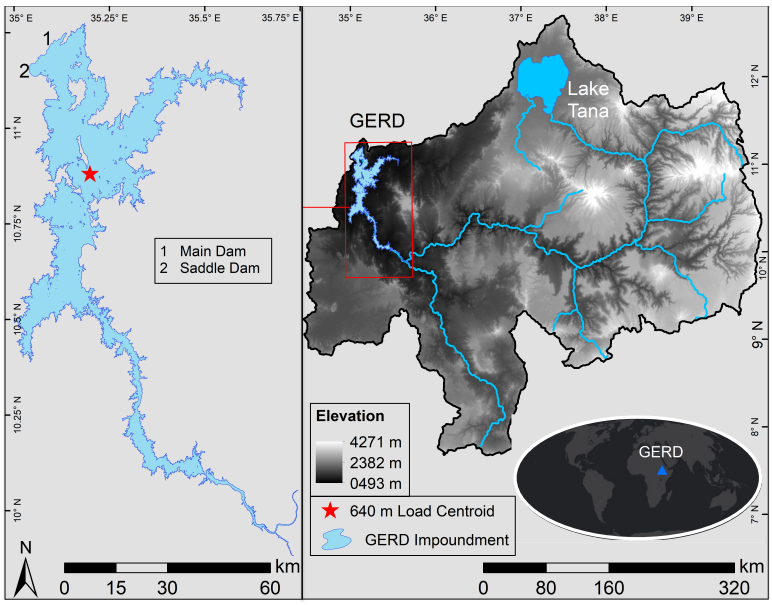

Figure 1. Overview figure of the Grand Ethiopian Renaissance Dam (GERD) study area. The elevation of the GERD impoundment's watershed is plotted on the right along with the global overview of the general location of the study area. The areal extent of the full GERD impoundment (640 m reservoir level) is plotted on the left along with the weighted hydrologic load centroid for the full water volume of the reservoir. The locations of the main dam and the saddle dam are also noted.

The impoundment of the Blue Nile at the GERD site will have a multitude of different impacts. The annual discharge curve will be severely altered due to the GERD construction and the subsequent large volume of the impoundment. The large capacity of the GERD impoundment allows for a near-equal discharge for each month of the year, allowing for a reduction in both high and low Blue Nile flow events [7]. To this end, there will likely be fewer flood and drought events and the region's hydrologic uncertainty will be reduced. The GERD is not the first dam on the Blue Nile or the Nile. However, the upstream location coupled with the size of the reservoir will affect the

already completed downstream hydrologic engineering projects. For example, three downstream dams (Rosaries, Sennar, and Aswan High) will need to adjust their release operations in order to maintain Sudanese agricultural water supplies [10]. Downstream hydrologic power generation could possibly be affected by the filling and operation of the GERD impoundment. The potential reduction in power generation will be related to the filling and operation scenarios that the GERD water managers decide upon [6, 10, 11].

Groundwater levels are also likely to be impacted by the GERD impoundment and subsequent reservoir operations. To this end, reservoirs can provide seepage into the subsurficial rock and connected aquifer systems. This diffusion of water into the underlying rock is capable of increasing pore pressure and reducing frictional stresses. Further, impoundment and operational strategies of large dams (e.g., Three Gorges) have been shown to directly alter groundwater levels for hydraulically connected aquifer systems [12, 13]. These connections are capable of decreasing slope stability and can trigger slope failure events as caused by the changes in hydrostatic pressure due to the varying levels in the groundwater and the hydraulically connected reservoir levels [14-17].

Other impacts from the GERD impoundment are related to the large hydrologic loading forces applied to the reservoir-adjacent lithosphere. Drastic changes in surface loads brought on by large hydro-engineering projects can have far reaching implications for increased stress and strain on surrounding fault systems and subsequent seismicity [18-23]. The initial GERD impoundment and subsequent reservoir creation along with seasonal fluxes in water levels due to operational phases cause large changes in both

the areal extent and volumetric content of the reservoir. These marked variations in hydrologic loads can impart large forces on the surface of the Earth and are capable of deforming the lithosphere. For example, numerous studies have shown that in situ and remotely sensed products (e.g., GNSS, InSAR, GRACE, etc.) are capable of quantifying the flexural response from changes in hydrologic loads (snow, reservoirs, seasonal precipitation, drought, regional climatic changes, lakes, etc.) [24-31]. The size of the GERD project allows for a large influx of water into the upstream reservoir area during the filling stages as well as during normal seasonal operation. These loads are highly dependent on the chosen filling and operational strategies. The amplitude and extent of the flexural response is mostly dependent on the underlying rheology as well as the timing and amount of the hydrologic forcing. Both the early filling stages and the subsequent operational scenarios play important roles in the application of hydrologic load induced lithospheric deformation for an impoundment of this size.

This study seeks to provide a first look at the modeled vertical (subsidence and uplift) and horizontal displacement brought on by the initial GERD impoundment along with reservoir operations from several predicted seasonal release plans. This work was undertaken in order to glean a better understanding of the amplitude and spatiotemporal dynamics of the load-induced flexural response at and around the GERD study site. In order to accomplish this task, we seek to answer the following questions: (1) What are the areal extents, reservoir volumes, and hydrologic loads from potential scenarios of long-term reservoir operation and multi-year reservoir filling schedules? (2) What are the modeled elastic flexural responses as caused by hydrologic loading variations from long-term reservoir operations and multi-year reservoir filling schedules at the GERD?

We utilize digital surface models (DSMs) and hydrologic inputs from several filling and operational scenarios to answer (1), and we use those results along with a localized Earth model to compute the elastic displacements for each of the scenarios in order to answer (2).

2. Data and Methods

2.1. Reservoir Extents, Volumes, and Loads

Traditional remote sensing techniques to delineate water/reservoir extents (e.g., multispectral and/or radar satellite platforms) cannot be employed in this situation as the final GERD impoundment process has not yet begun. Instead, this study utilizes a DSM-based technique to determine areal extents and loads for varying reservoir levels behind the GERD. Several remotely sensed DSMs were examined in order to more precisely derive the areal extent, reservoir volume, and hydrologic load for every 1 m increment of the GERD impoundment. We inspected five different well-known DSMs that encompass the entirety of our study area, and selected the most accurate surface model based on a comparison of overlapping data from the Geoscience Laser Altimeter System (GLAS) instrument onboard the Ice, Cloud, and land Elevation satellite (ICESat) platform. More specifically, we tested three DSMs generated from Shuttle Radar Topography Mission (SRTM) data (one arcsecond void filled, three arcsecond void filled, three arcsecond not void filled), one derived from Advanced Land Observing Satellite (ALOS) data, and another from Advanced Spaceborne Thermal Emission and Reflection Radiometer (ASTER) data [32-34]. All five surface models were mosaicked to encompass the entirety of the study area (all DSM grids encompassing the minimum

bounding box) around the extent of the full GERD impoundment and were then projected to UTM Zone 36N (EPSG:32636) using the WGS84 ellipsoid.

We acquired all GLAH14 (Land Elevation; Version 34) GLAS tracks from the National Snow and Ice Data Center (NSIDC) that overlap the five different mosaicked DSMs mentioned above [35]. GLAH14 elevation products are provided in ellipsoidal heights referenced to the Topex/Poseidon (TP) ellipsoid. As such, the GLAH14 data were converted to orthometric height above the WGS84 reference ellipsoid by subtracting the corresponding EGM96 geoid from the TP ellipsoidal heights and then subtracting 0.7 m. The WGS84 coordinates were projected to UTM Zone 36N (EPSG:32636) in order to be directly comparable to the five DSMs investigated in this study. Lastly, the elevation values were filtered using the "sat_corr_flg" (saturation correction) and "FRir_qa_flg" (cloud presence) flags to only keep unsaturated elevation GLAS points and to further filter the GLAS data to only include cloud-free pulses, respectively. We compared overlapping GLAS pulses to the nearest DSM cell value for each of the five elevation models mentioned above in order to determine the appropriate DSM used to derive the most reliable hydrologic load inputs for our deformation models (as discussed in Section 2.2). We calculated the mean absolute difference and standard deviation for all quality GLAS pulses from the nearest cell for each of the five DSMs at five different slope bins of less than or equal to 1°, 3°, 5°, 10°, and 90° (i.e., all data). Mean absolute differences were derived for several slope bins in order to better determine the most accurate DSM to select for further processing. Areas with larger slopes can cause increased ground elevation values within the ~70 m GLAS footprint. These increased elevation ranges can decrease the accuracy of the returned

GLAS elevation value as the elevation variation affects the GLAS laser return time and power, and subsequently negatively affects the final ellipsoidal height given by the GLAH14 product. We utilize Table 1 to show the GLAS comparisons for each of the slope bins for the five DSMs investigated. We note that the AW3D30 DSM has a lower mean absolute difference for each of the five different slope bins as compared with every other DSM we investigated. Similarly, the standard deviations are almost always lower for the AW3D30 DSM as compared with the other four surface models. The overall lower mean absolute differences and associated standard deviations for the AW3D30 DSM are evident in this table and highlight why we have selected this surface model for our hydrologic calculations. For comparison, we display the meter-by-meter areal extent and volumetric water loads for each of the five DSMs mentioned above in Table S1. We note increases of ~7 and ~19% in areal extent and volumetric water load for the least accurate DSM investigated as compared to the results from the AW3D30 DSM that we have utilized for our final reservoir calculations. We describe the ALOS-based DSM in the following paragraph.

DSM	**All: Mean Difference (SD)**	**1°: Mean Difference (SD)**	**3°: Mean Difference (SD)**	**5°: Mean Difference (SD)**	**10°: Mean Difference (SD)**
ALOS	4.61 m (26.73 m)	3.85 m (1.69 m)	3.74 m (4.15 m)	3.82 m (20.93 m)	3.77 m (20.18 m)
ASTER	8.16 m (27.20 m)	6.32 m (4.29 m)	6.04 m (5.73 m)	6.42 m (21.28 m)	6.88 m (20.65 m)
SRTM_1arc	5.47 m	4.56 m	4.74 m	4.84 m	4.75 m

	(26.71 m)	(2.09 m)	(4.28 m)	(20.87 m)	(20.13 m)
SRTM_3arc_nonVoid	7.22 m (27.17 m)	4.60 m (2.23 m)	4.86 m (4.46 m)	5.07 m (20.92 m)	5.34 m (20.24 m)
SRTM_3arc_yesVoid	7.22 m (27.17 m)	4.60 m (2.23 m)	4.86 m (4.46 m)	5.07 m (20.92 m)	5.34 m (20.24 m)

Table 1. Mean absolute differences in elevation between the investigated digital surface models (DSMs) and spatially overlapping Ice, Cloud, and land Elevation satellite (ICESat) Geoscience Laser Altimeter System (GLAS) pulses for all data, slopes ≤1°, ≤ 3°, ≤5°, and ≤10° along with their standard deviations.

The ALOS DSM was acquired from the Japan Aerospace Exploration Agency (JAXA) and is part of the ALOS World 3D-30m (AW3D30) project. The surface model has a cell spacing of 1 arcsecond (~30 m) and a vertical height accuracy of 4.4 m (RMSE). The AW3D30 product was up-sampled from the AW3D version (~5 m cell size) using a simple average of the 49 (7 × 7) underlying AW3D cells, and consists of 16-bit signed integer values [36]. We mosaicked three AW3D30 grids (N009E035, N010E035, N011E035) over the study region and manually adjusted the cells where the GERD infrastructure (main dam and saddle dam) is located to the appropriate infrastructural elevation values. We utilized this DSM to derive the areal extent, reservoir volume, and subsequently, the GERD impoundment load grids used in the flexural model described in Section 2.2.

We derived the areal extents, volumes, and water level changes for each 1 m increment from the pre-impoundment level of 500 m to the reservoir's maximum

capacity at 640 m. The AW3D30 DSM was contoured for each of the associated water level increments upstream of the GERD pour point, and the incremental areal extents were then derived for each reservoir extent boundary. Similarly, for each water level increment, we calculated the volume for each cell in the grid by deriving the water depth change from the initial DSM elevation value and multiplied by the appropriate cell dimensions of the mosaicked AW3D30 surface model (i.e., ~30 × ~30 m). We then summed these cell-by-cell volumes to derive the total volumetric content for the incremental water level. These meter-by-meter areal extent and volumetric water load values are further used to plot hypsometric curves for water level versus areal extent and water load along with areal extent versus water load. Cubic and quadratic fits of these curves were calculated and the coefficients from the water level versus water load and the areal extent versus water level equations were applied in order to create daily and mean monthly water level, areal extent, and volumetric content changes from inflow and outflow calculations for each of the different impoundment and operational scenarios that are discussed in the following paragraph.

A filling plan has not been finalized for the GERD, and, as such, we focused our input water load derivations and subsequent initial impoundment deformation modeling on representative filling scenarios as laid out in [5]. [5] utilized an 80-month filling strategy based on natural inflow rates from 1973–1978. Here, the mean annual inflow of this impoundment strategy is only ~0.5% greater than the 41-year mean annual inflow of ~50 Gt (1961–2002), and the annual outflow during this initial impoundment stage does not fall below 28.9 Gt. Monthly water level values were acquired from the above-cited paper, and daily loads were created in conjunction with the coefficients from the cubic

fits mentioned in the previous paragraph. We call this daily filling scenario *M1*. [7] derived precipitation, seepage, actual evapotranspiration (ET), inflow, and outflow (in m^3s^{-1}) at the GERD impoundment for 39 years (January 1961 to the end of December 1999). These 468 monthly hydrologic observations were utilized to determine average monthly inflow datasets based on three types of water years (Average: 1961–1999, Average Wet: 1961–1981, and Average Dry: 1981–1999), where we took the mean of the water inflow from the hydrologic variables within their respective year ranges. The monthly GERD outflow rates from these three sets of inflow observations were derived as a percentage of the total inflow from 5 to 90% at 5% intervals. Here, an outflow percentage value of 5 indicates that only 5% of the daily GERD inflow is allowed to flow through the dam outlets as outflow (i.e., 95% storage). We note that precipitation inputs were included in the inflow calculation and the seepage and actual ET were removed from the reservoir volume and the subsequent water level calculation (not the outflow). That is, there may be a negative water storage rate in months where the summation of the seepage and ET rates is greater than the difference between the inflow and outflow rates. Finally, the monthly reservoir storage was determined for each of the three types of water years and their 18 different percentages of inflow rates from 5 to 90%. These monthly hydrologic observations were utilized in conjunction with the coefficients from the cubic fits described in the previous paragraph to determine daily water levels for each scenario. We call these filling scenarios A5–A90 (Average), AW5–AW90 (Average Wet), and AD5–AD90 (Average Dry), respectively. These cell-by-cell water levels for each of the 55 different impoundment scenarios (one scenario derived from [5] and 54

derived from [7]) were used to create the initial impoundment load grids that are utilized as inputs into the elastic deformation model that is discussed in Section 2.2.

Similarly, a seasonal operation plan has not been finalized for the GERD, and, as such, we focused our annual flexural modeling on the five operational strategies as laid out in [7]. They described these five operational scenarios as (1) "hpp_1500MW_a": Operation is geared towards a hydroelectric power production (hpp) of 1500 MW regardless of the season, unless the reservoir is at full capacity (hpp increase) or the total volume is low (hpp decrease), (2) "hpp_1500MW_b": Operation is geared towards an hpp of 1500 MW if the active storage is less than 50%, unless the total volume is low (hpp decrease) or the active storage of the reservoir is above 50% (hpp increase), (3) "hpp_1700MW": Operation is geared towards an hpp of 1700 MW regardless of the season, unless the reservoir is at full capacity (hpp increase) or the total volume is low (hpp decrease), (4) "hpp_1800MW": Operation is geared towards an hpp of 1800 MW regardless of the season or overall reservoir volume, unless the reservoir is at full capacity (hpp increase), and (5) "eco_mgt": Operation best represents the natural flow regime with peak flows during the flood season and reduced flows during the dry season. We call these five operational scenarios (L1–L5). Similar to the abovementioned filling scenarios from [7], these operational strategies consist of monthly precipitation, seepage, actual ET, inflow, and outflow (in m^3s^{-1}) at the GERD impoundment from January 1961 to the end of December 1999. The 468 different monthly hydrologic values described in the previous paragraph were used in order to derive two temporally different sets of overall inflow, outflow, and storage values for each of the five scenarios. Again, we note that precipitation inputs were included in the

inflow calculation and the seepage and actual ET were removed from the reservoir volume and the subsequent water level calculation (not the outflow). The first of the two monthly datasets consists of a single-year's inflow, outflow, and water storage as calculated from the respective months' mean from the entire 39-year dataset, and the second consists of the full 39-year hydrologic monthly dataset. The monthly hydrologic values from both of the temporally different sets of strategies were utilized in conjunction with the coefficients from the appropriate cubic fits in order to determine daily water levels. These cell-by-cell water levels for each of the five different reservoir operation phases were used to create the operational load grids that are utilized as inputs into the elastic deformation model that is discussed in Section 2.2.

2.2. SNREI Deformation

We created a spherically symmetric, non-rotating, elastic, and isotropic (SNREI) Earth model based on the local rheology around the study region in order to calculate the most accurate vertical and horizontal displacements imposed by the loading of the GERD impoundment scenarios as well as the loading and unloading from the seasonal reservoir operations. To this end, we utilized the rheologic parameters in the Crust 1.0 model [37] for the cell that encompasses the majority of the GERD impoundment (centered at 10.5° N, 35.5° E) to appropriately amend the STW105 reference Earth model [38] in order to derive more meaningful load Love numbers (LLNs) for the study region. More specifically, we used the density, compressional (V_p) and shear wave (V_s) velocities, and depths for the crustal values in the abovementioned Crust 1.0 cell and appropriately replaced the rheologic values in the STW105 Earth model while keeping

the original mantle properties intact. We also replaced the oceanic water layer in the upper 3 km of the STW105 model with appropriate density, V_p, and V_s values for the upper crust. From this altered, GERD-centric STW105 model (CRUSTY_GERD_STW105), we calculated the two Lamé parameters (λ and μ) for the Earth radii increments needed to appropriately derive the LLNs. We utilized the CRUSTY_GERD_STW105 Earth model and set the mantle to be both isotropic and compressible and the core to be layered and compressible in the calculation of the LLNs. Elastic LLNs were derived to a harmonic degree of 32768 (at 1 degree increments) using the method and scripts outlined in [39, 40]. These LLNs represent dimensionless parameters that explain Earth's elastic response to different loads and stresses [41, 42].

We calculated the elastic response, or Green's functions (GFs), to a set disc loading scenario using the flexural theory from [43] based on the CRUSTY_GERD_STW105 Earth model-derived LLNs using the Regional ElAstic Rebound calculator (REAR) from [44]. REAR is optimized for the calculation of displacements from very high harmonic degrees, which is important for the analysis of geodetic observables in study areas which are subjected to smaller-scale surface mass variations (like hydrologic loading at the reservoir scale) [45]. This is important as the increased number of spherical harmonic degrees allows for a higher resolution model domain (e.g., finely layered mantle and crustal layers) as well as for a more detailed (finer spatial resolution) output displacement product. REAR computes the elastic flexural response of SNREI Earth models to loading and unloading scenarios. In this case, the loading and unloading scenarios are the filling of the GERD impoundment

along with the seasonal operations. The computed GFs are the surface rates of displacement associated with a unit rate of mass variation from a finite-sized disc load, where the diameter of the disc corresponds to the cell resolution of the input DSM (AW3D30) utilized to derive the load files. These GFs were utilized in conjunction with the hydrologic load files calculated for each 1 m water level increment (500 to 640 m) to derive the elastic deformation caused by the hydrologic load from the entire GERD impoundment. We also derived the flexural response for each areal extent where the corresponding water level utilized in the input load file is the water level at which the areal extent was derived plus 1 m (501 to 641 m). This was done to create a displacement factor to utilize in the linear interpolation of the flexural response from sub-meter water level changes. For example, we derived the vertical and horizontal displacements utilizing each cell from the 600 m water level areal extent along with the deformation from the same cells plus 1 m of water level (i.e., 601 m). We employed the flexural responses from these +1 m data runs to derive a displacement factor to apply to daily floating point values of water level changes that are present in our load inputs from the different filling and operational scenarios. For example, this displacement factor is calculated from the quotient of the displacement from the 600 m areal extent load with a water level of 600 + 1 m and the displacement from the 600 m areal extent load with a water level of 600 m, divided by 1000. This allows us to calculate the daily flexural responses from sub-meter water level changes (e.g., at 0.001 m intervals between water levels of 600 and 601 m) without having to run the flexural model through many tens of thousands of iterations.

We utilized the daily reservoir load files as described in Section 2.1 to derive the modeled flexural response using the SNREI model discussed in the preceding paragraph. We calculated the deformation from the daily load changes for each of the 55 different impoundment scenarios as well as from both temporal sets of the 5 different operational scenarios. We then determined the daily accumulated maximum vertical and horizontal displacements from those daily load changes for each of the 55 different impoundment scenarios. We note that we stopped each filling scenario as soon as the reservoir reached its full supply level of 640 m. We also calculated the time to full supply level along with the accumulated annual inflow, outflow, and storage for each of these 55 filling scenarios. We note that each of these data runs began on January 1. We utilized the daily vertical and horizontal displacements in response to the daily load changes (Section 2.1) to derive the maximum seasonal accumulated flexural responses for both the full 39-year dataset and the average annual scenarios (as discussed in Section 2.1). Here, the maximum accumulated responses are defined as the displacement from the load change at the beginning of the year to the peak load for the highest annual amplitude water load change for each of the scenarios. We note that we started the average annual operational scenarios on the first day of the first month in which there is a positive storage rate (i.e., L1–L3, L5: July 1, and L4: June 1), and we started the annual cycles within the 39-year seasonal operational dataset on the first day in which there was a positive water storage.

3. Results

3.1. Initial Impoundment

The overall areal extent and volumetric water load for the full impoundment of the GERD (500 to 640 m) using the AW3D30 surface model and the methods outlined in Section 2.1 are ~1763.30 km^2 and 67.37 Gt, respectively. We derived the monthly inflow, outflow, and water storage values for each of the 54 impoundment scenarios derived from [7], and plot them in Figures S1, S2, and S3. We utilized these annual curves to derive daily reservoir inflow and outflow, and subsequently the accumulated water levels and volumes for each of the impoundment strategies. We focus our discussion on the 22 filling scenarios M1, A45-A75, AW45–AW75, and AD45–AD75 due to the markedly low levels of accumulated annual outflow and long impoundment periods at the lower and upper end of the percentage scenarios, respectively. We note that the full impoundment periods and the accumulated annual outflow rates for the A80-A90, AW80–AW90, and AD80–AD90 and the A5-A40, AW5-AW40, and AD5-AD40 scenarios range from 9.7 (AW80) to 76.7 years (AD90) and 2.4 (AD5) to 22.0 Gt/year (AW40), respectively. The total accumulated annual inflow for each of the average, average-wet, average-dry, and M1 impoundment scenarios are 51.25, 55.11, 48.32, and 50.00 Gt, respectively. For reference, we plot the daily reservoir inflows and outflows along with the accumulated water levels and volumes for each of the 54 impoundment strategies derived from [7] in Supplementary materials Figures S4, S5, and S6. We also plot the accumulated daily GERD storage and water levels for the M1 scenario derived from [5] in Figure S7. Along with these plots, we show the time-to-full, the accumulated annual inflows, outflows, and storage values for each of the 54 filling scenarios derived from [7] (A5–A90, AW5–AW90, and AD5–AD90) in Table S2. We note that we do not have the inflow and outflow rates for scenario M1 as the data

acquired from [5] do not consist of the full hydrologic values that we have acquired from the study by [7]. However, we require only water levels in order to appropriately derive the load inputs for the elastic flexural model.

The maximum accumulated vertical and horizontal displacements from the SNREI model for the complete GERD impoundment utilizing the methods and datasets described in Sections 2.1 and 2.2 are 11.99 and 1.99 cm, respectively. Figure 2 plots the total vertical and horizontal response from the entire hydrologic load from the full 140 m GERD impoundment. Vertical and horizontal displacements from the complete impoundment in excess of 1 cm extend out to ~99 and ~49 km from the 640 m weighted hydrologic load centroid, respectively. We point the reader to Video S1 for an animation showing the modeled flexural response along with its associated areal extent and water volume for each meter of water level rise from 500 to 640 m.

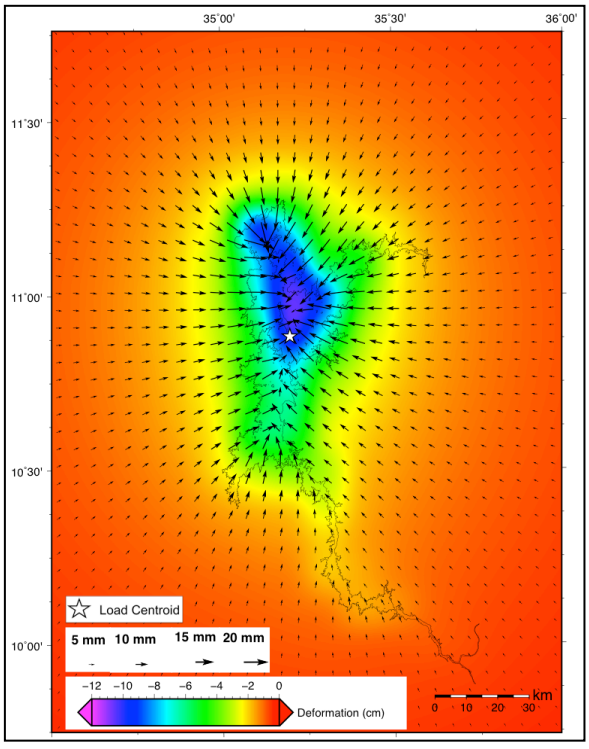

Figure 2. Vertical and horizontal displacements from the full GERD impoundment. The modeled vertical displacement is plotted on the colored grid while the horizontal displacement motion vectors are plotted on top. The weighted hydrologic load centroid from the full reservoir volume is plotted as a star. The total areal extent of the full impoundment (640 m reservoir level) is drawn as a black polygon. These are the modeled elastic displacements from the full hydrologic loading for the entire GERD impoundment.

Figure 3 plots the daily accumulated horizontal and vertical displacements for each of the 22 different filling scenarios. We note that the vertical displacement for each of the filling scenarios maxes out at the same response due to the fact that we plot the accumulated displacement for the entire filling, and that according to [43], the elastic flexural response to any given load is both constant and instantaneous. That is to say, these maximum displacement values are the same for the vertical and horizontal displacements plotted in Figure 2.

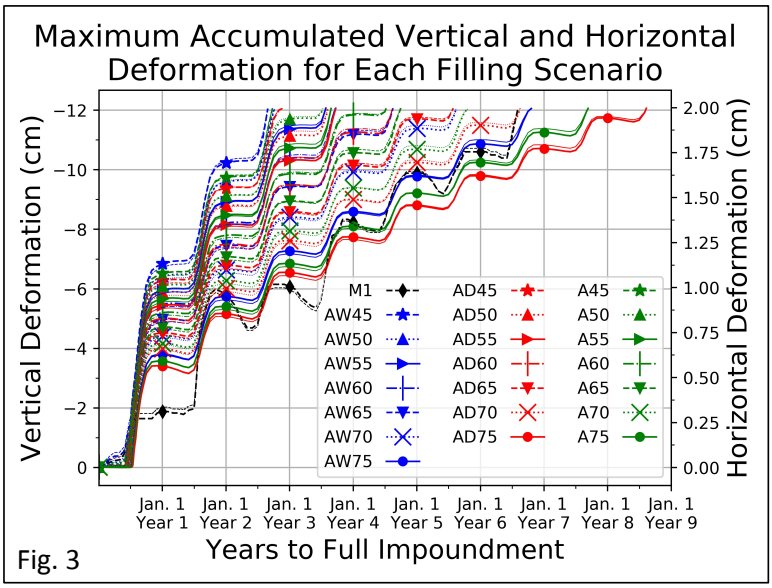

Fig. 3

Figure 3. Accumulated daily vertical and horizontal displacements from 22 different filling scenarios. The horizontal displacement on the second y-axis is marginally offset from the vertical displacement on the first y-axis and is plotted as the slightly minor lines of the same symbology for each of the filling scenarios.

3.2. Seasonal Operations

We derived the average monthly inflow, outflow, and water storage values for each of the five operational cycles, and plot them in s8. We utilized these monthly hydrologic variables to derive an average annual regime of daily reservoir inflow and outflow rates, and subsequently the accumulated water levels and volumes for each of the five seasonal strategies (*L1–L5*). These are plotted in Figure S9. This figure shows that the maximum annual seasonal amplitudes of change for the areal extent, water level, and reservoir volume for each of the five average annual operational scenarios (L1–L5) are 491.12, 492.28, 484.33, 420.06, and 360.40 km^2, 16.22, 16.25, 16.01, 14.13, and 12.22 m, and 23.09, 23.16, 22.76, 19.59, and 16.74 km^3, respectively. We note that the percentage of the total accumulated water volume from the full impoundment for each average annual seasonal scenario is 25 (L1), 34 (L2), 34 (L3), 34 (L4), and 29% (L5). Similarly, we plot the daily water levels, water storage, and inflow and outflow rates for the five operational scenarios over their entire 39-year cycle in Figure S10. This figure shows that the maximum annual seasonal amplitudes of change for the areal extent, water level, and reservoir volume for each of the 39-year operational scenarios (L1–L5) are 902.02, 868.00, 821.83, 903.36, and 644.81 km^2, 41.22, 36.99, 33.28, 46.53, and 26.88 m, and 36.46, 36.30, 35.22, 34.35, and 27.93

km^3, respectively. We note that the percentages of the total accumulated water volume from the full impoundment for each of these maximum seasonal amplitudes from the full 39-year daily seasonal scenarios are 54 (L1), 54 (L2), 52 (L3), 51 (L4), and 41% (L5). This shows how large an effect dam operations can have on the amplitudes of seasonal hydrologic load fluctuations. In turn, these markedly different fluxes will determine the amplitude of flexural responses to the corresponding annual load changes in any given operational year, as discussed below.

The maximum accumulated vertical (and horizontal) displacement from the SNREI model for each of the five average annual operational scenarios (L1–L5) is 3.27 (4.89), 3.29 (4.94), 3.24 (4.84), 2.76 (4.14), and 2.40 cm (3.59 mm), respectively. We plot the total vertical and horizontal response for these annual average operational scenarios (L1–L5) in Figure 4a–e. Vertical and horizontal displacements from the maximum seasonal amplitudes in excess of 1 cm and 3 mm for these five scenarios extend out to ~92 and ~51 km (L1–L3), ~77 and ~44 km (L4), and lastly ~49 and ~40 km (L5) from their respective maximum water level weighted hydrologic load centroids.

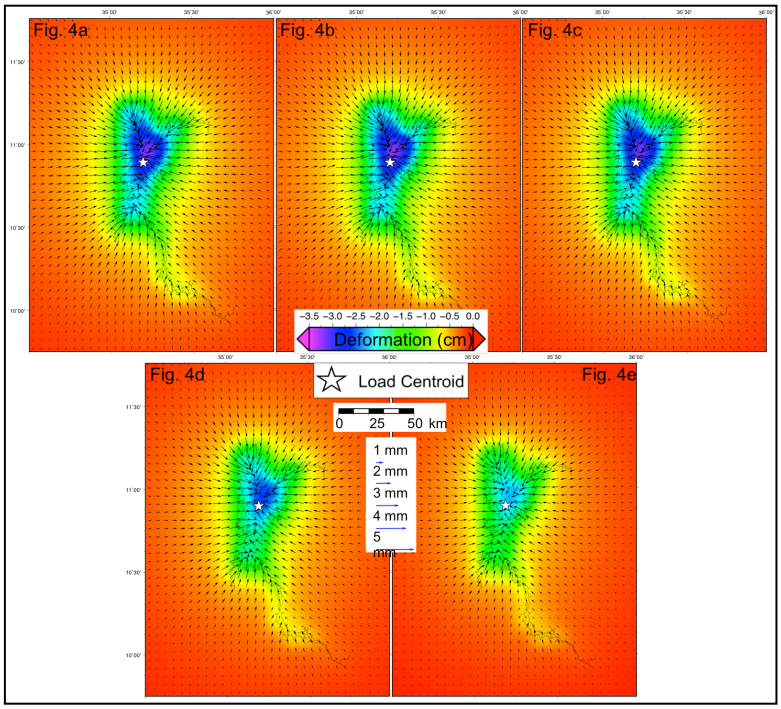

Figure 4. Vertical and horizontal displacements from each of the five average annual operational scenarios. The modeled vertical displacement is plotted on the colored grid while the horizontal displacement motion vectors are plotted on top. The maximum water level weighted hydrologic load centroids are plotted as stars. The maximum areal extent of the reservoir for each of these scenarios is drawn as a black polygon. (**a**)–(**e**) correspond to the average annual seasonal scenarios L1–L5, respectively. These are the maximum accumulated displacements for each of the five average annual operational scenarios.

We plot the daily accumulated maximum horizontal and vertical displacements for each of the five seasonal operational scenarios in Figure 5. We note that the maximum accumulated displacements are the same as the responses plotted in Figure 4a–e. We also note that the maximum displacement for operational scenario *L4* occurs

one month prior to the other four scenarios. This is due to the operational start date of June 1 for the *L4* scenario versus July 1 for the remaining four scenarios. Here, July 1 and June 1 are the first days in each scenario in which there is net positive reservoir storage.

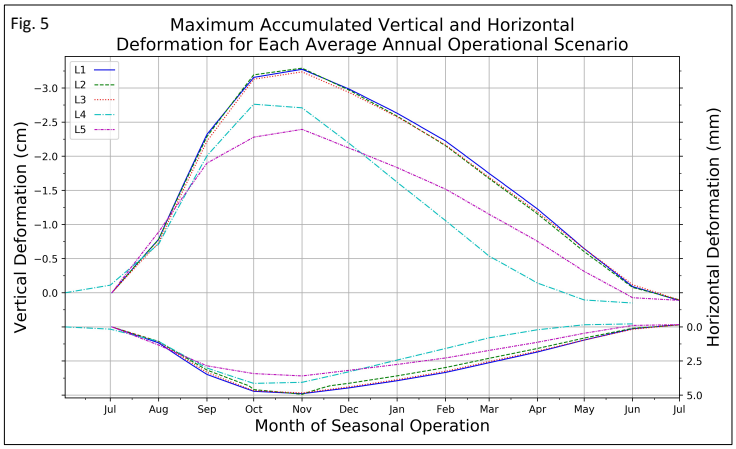

Figure 5. Maximum accumulated daily vertical and horizontal displacements from the five different average annual operational scenarios. Seasonal operations are started July 1 for scenarios L1–L3 and L5 and on June 1 for scenario L4. These are the first days in each scenario in which there is net positive reservoir storage. These plots track the daily displacement at the location of the overall maximum accumulated vertical and horizontal displacement for each average annual scenario. Note that the top and bottom portions of the plot correspond to vertical and horizontal displacement in cm and mm, respectively. We also note that the y-axis scale for the horizontal displacement is half that of the vertical displacement.

We note that the maximum accumulated vertical (and horizontal) displacement for each of the largest seasonal amplitudes of hydrologic change from the full 39-year dataset for the five operational scenarios (*L1–L5*) is 6.58 (9.39), 6.29 (8.94), 5.91 (8.45),

6.56 (9.58), and 4.61 cm (6.69 mm), respectively. We plot the total vertical and horizontal response for these maximum annual operational scenarios (*L1–L5*) in Figure 6a–e, respectively. Vertical and horizontal displacements from the maximum seasonal amplitudes in excess of 1 cm and 5 mm for these scenarios extend to ~78 and ~50 km (L1), ~93 and ~50 km (L2), ~93 and ~48 km (L3), ~78 and ~46 km (L4), and lastly ~78 and ~44 km (L5) from their respective maximum water level weighted hydrologic load centroids.

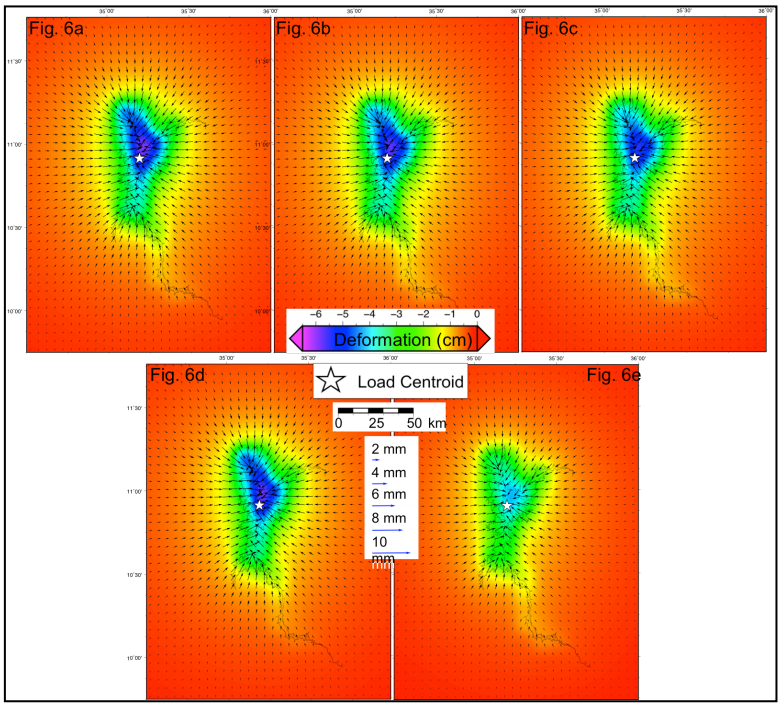

Figure 6. Total vertical and horizontal displacements from the maximum annual amplitude for each of the five 39-year operational scenarios. The modeled vertical displacement is plotted on the colored grid while the horizontal displacement motion vectors are plotted on top. The maximum water level weighted hydrologic load centroids are plotted as stars, and the maximum areal extent of the reservoir for each of these scenarios is drawn as a black polygon. (**a**)–(**e**) correspond to the maximum

displacement out of the full 39-year dataset for each of the five different seasonal operational scenarios (L1–L5).

We plot the daily maximum vertical and horizontal accumulated flexural responses from the full 39-year dataset for each of the five scenarios in Figure 7. We start the water level for each of these runs such that the maximum water level over the full 39-year dataset is never greater than the maximum GERD water level of 640 m. We note that the seasonal maximum and minimum vertical and horizontal displacements for all five scenarios over all 39 years of hydrologic data are 6.58 and 1.32 cm (vertical) and 9.58 and 1.91 mm (horizontal), respectively. This further highlights the stark differences in the annual stresses applied on the crust from the varying hydrologic loading and unloading operational scenarios of the reservoir.

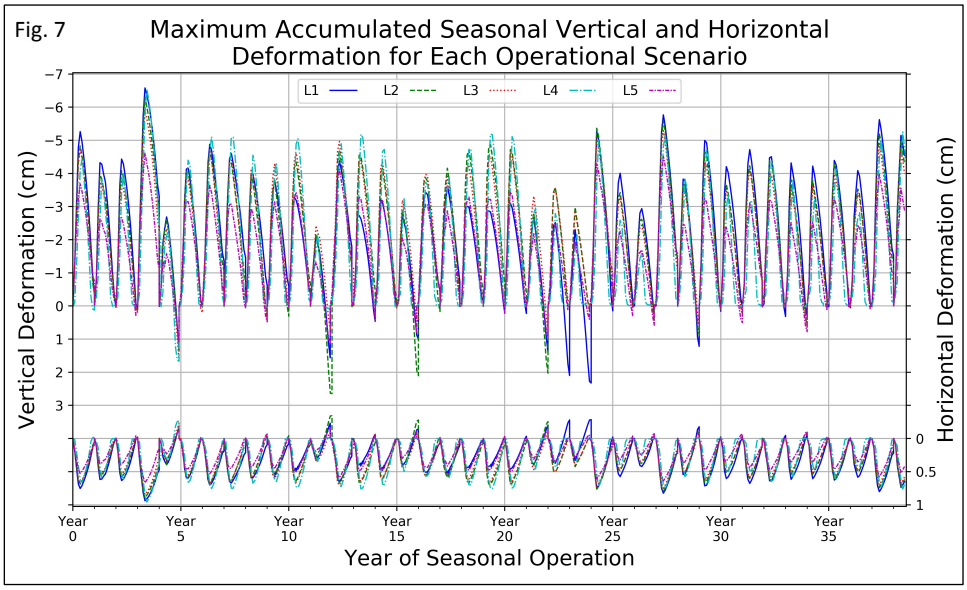

Figure 7. Maximum seasonal accumulated daily vertical and horizontal displacements for all five operational scenarios from the full 39-year datasets. These plots track the

daily displacement at the location of the annual season's overall maximum accumulated vertical and horizontal displacement for each scenario. The plotted data are the accumulated vertical and horizontal displacements for each seasonal cycle in the full 39-year dataset. Note that the displacement at the beginning of each season reverts back to zero, and the subsequent seasonal displacements are accumulated from that start point until the end of the season. The top and bottom portions of the plot correspond to vertical and horizontal displacement, respectively. We also note that the y-axis scale for the horizontal displacement is half that of the vertical displacement.

4. Discussion

4.1. Initial Impoundment

At present, our DSM-derived results cannot be validated to in situ or other remote sensing-based areal extent and volumetric water load curves of the GERD as the final impoundment process has not yet begun. However, our very high R-squared values of 0.99 are indicative of the quality of the relationships between water level, areal extent, and volumetric content (Figure S11a–c). These relationships can be employed by water managers and researchers to derive more meaningful operational rule curves and to better understand the hydrologic fluctuations as they relate to future GERD studies (e.g., remotely sensed volumetric calculations from ICESat-2, GRACE-FO, and SWOT). We note our method relies heavily on the DSM employed by our processing methodology, and that we have utilized the most accurate surface model (as compared to spatially overlapping ICESat GLAS pulses) at our disposal (Section 2.1).

For comparison to the modeled vertical displacements from the full impoundment at the GERD (Figure 2), we note that vertical displacements from the full impoundment for two other large hydro-engineering projects (Lake Mead in the United States and the Three Gorges Reservoir in China) are ~12 cm and ~3.8 cm, respectively [46, 47]. The locational difference in the maximum vertical displacement and the weighted hydrologic load centroid in Figure 2 is very likely caused by the upstream reaches of the GERD reservoir at this water level "pulling" the centroid toward the south-southeast away from the deformation center. Further, Video S1 shows the south-southeastward migration of the weighted hydrologic load centroid as the reservoir levels rise and the upstream reaches "pull" the centroids in that direction. We note that utilizing a different DSM than the one selected for this analysis would affect the displacements calculated from our flexural modeling methodology. The displacements from a given load are directly related to the input water levels at each cell in the DSM grid. As such, the overall difference in the modeled displacements from different DSMs would be dependent on the cell-by-cell differences in their water levels. We note that the results in Figure 2 and Video S1 are the total accumulated elastic flexural response from the GERD impoundment in its entirety. Further, we note that filling scenarios for reservoirs of this size are typically drawn out over several years/wet-dry seasons due to the size of the reservoir itself, downstream water users, and the seasonality of the inflows at the impoundment.

A filling plan has not been finalized for the GERD, and, as such, we focus our discussion on 22 (M1, A45–75, AW45–75, and AD45–75) of the 55 different scenarios as laid out in the end of Section 2.1. These particular filling scenarios were deemed the most realistic after comparing their outflow rates to the mean outflow at the

impoundment site as well as their respective filling times. The former is important to negate downstream user impacts and the latter is important for the operation and timing of the reservoir operations. The filling time is also an important parameter where faster impoundments may increase the drained response that is responsible for the increase in diffusive pore pressure through the underlying rock. The filling scenarios had a start date of January 1, and for the most part, the first five months of each filling scenario shows little to no impoundment. We note that 14 of the 22 filling scenarios examined were complete before the fifth year, and that the shortest filling scenario (AW45) and the longest filling scenario (AD75) took ~2.65 and ~8.6 years, respectively.

Although the total magnitude of the vertical and horizontal displacements are the same for each filling scenario plotted in Figure 3, it is the timing of the hydrologic variables that play a role in the temporal dynamics of the load-induced flexural response. This is especially true for a marked seasonal hydrologic regime defined by a peak discharge lasting a few months followed by a low-flow period that we see at the GERD impoundment. This is evidenced in Figure 3 by the fact that 8 of the 22 filling scenarios (A45–55, AW45–55, and AD45–50) have nearly 50% (~6 and ~1 cm) of their total accumulated (~12 and ~2 cm) vertical and horizontal displacement (respectively) within the last half of the first year of the filling scenario. We point the reader to Dataset S1 for the complete displacement arrays for each of the 22 filling scenarios. We also note that all but one of the filling scenarios (M1) have more than 25% of their total deformation in the same six-month time span. However, if we think in terms of displacement per unit time and we take the quotient of the total accumulated vertical displacement and the filling time for each scenario plotted in Figure 3, we find that the

top-five scenarios in terms of the lowest total daily displacement rate are AD75 (~0.04), A75 (~0.04), AW75 (~0.05), AD70 (~0.05), and M1 (~0.05 mm/day). In contrast, the bottom-five scenarios in terms of the highest total daily displacement rate are AW45 (~0.12), A45 (~0.12), AW50 (~0.12), AD45 (~0.11), and A50 (~0.09 mm/day). We note that because the total displacement is the same for each of the filling scenarios (500 to 640 m), these displacement rates are for the five longest and five shortest filling scenarios, respectively. We reiterate that the overall flexural response (Figure 2) from the full impoundment applied on the surrounding lithosphere will not occur within one season, but will be spread out over the filling scenario decided upon by the water managers. As such, we have shown (Figure 3) 22 different potential filling scenarios at the GERD, and how their associated flexural responses accumulate over their respective impoundment periods.

4.2. Seasonal Operations

Overall, the differences in accumulated horizontal and vertical displacements between the five operational scenarios plotted in Figure 5 stem from the different monthly (and subsequently, the daily) reservoir outflow rates. These scenarios are discussed at the end of Section 2.1 and are plotted in Figures S8 and S9, respectively. The different outflow rates are responsible for variations in monthly (and subsequently, the daily) water storage, and, in turn, the different areal extents and total water levels for each of the five scenarios. We expect there to be differences in the accumulated displacement from the different operational scenarios as the inputs into the elastic deformation models are the hydrologic load grids derived from these areal extents and

water levels. The notable difference in both the timing and the quantity of reservoir outflow in scenarios *L4* and *L5* as compared with the outflow rates in scenarios L1–L3 causes the decreased accumulated displacement for scenarios L4 and L5 (See Figures S8 and S9).

We start the seasonal model runs at the first date in which there is positive reservoir storage (L1–L3, L5: July 1 and L4: June 1) and use a 622 m reservoir level as the initial model input. We selected the 622 m water level as [48] specified the minimum operating level of the GERD as such. However, other studies stated that the minimum operating level is at 590 m [49, 50]. We ran our models with both 622 and 590 m as the starting point, and we note that the total volumetric change is the same in both runs and that the amplitudes of the seasonal water level and areal extent changes are larger with the 590 m elevation starting point. Further, the maximum accumulated vertical and horizontal displacements are around 1 cm and 1 mm larger (respectively) in the 590 m data runs as compared with the flexural results from the 622 m starting point. This is due to the increased load per unit area for the 590 m data runs as the reservoir volumes for both starting points are the same, but the maximum areal extents for the 590 m runs are smaller than their 622 m counterparts, thereby increasing the hydrologic load per unit area. In turn, this larger, more condensed loading affects the distance that the deformation extends from the corresponding load centroid as compared with the 622 m data runs. Here, we note that the vertical and horizontal displacements from the maximum seasonal amplitudes in excess of 1 cm and 3 mm for the scenarios with a 590 m water level start extend out to ~59 and ~50 km (L1–L2), ~59 and ~48 km (L3), ~48 and ~46 km (L4), and lastly ~49 and ~42 km (L5) from their respective maximum water

level weighted hydrologic load centroids. This overall reduction in the spatial reach of the deformation as compared with the 622 m data runs is due to the abovementioned condensed hydrologic loading around the load centroid where the 590 m data runs do not have the increased displacement in the upstream (southerly) reaches of the reservoir.

The vertical and horizontal displacements plotted in Figure 7 are normalized to the first day of the seasonal cycle. Here, we define the beginning of an annual seasonal cycle as the first day in which there is positive water storage and the end to that cycle occurs when the water storage flips from negative to positive (i.e., a full seasonal inflow and outflow curve). The daily vertical displacement plotted in Figure 7 is the accumulated vertical response for that season at the location of maximum deformation for that annual cycle. Here, vertical displacement that is greater than zero indicates that the daily water level has dropped below the water level at the start of our defined seasonal cycle, and the accumulated displacement switches sign to a positive value due to the continued withdrawal of reservoir water (decreased water storage) and the subsequent upward flexural response (relaxation) of the crust. The decrease in water storage and subsequent crustal relaxation for each seasonal cycle begins after the maximum accumulated vertical displacement peak on the seasonal curves plotted in Figure 7 and ends when the reservoir storage changes from a positive to a negative value. The horizontal displacement is nearly always positive, and, similar to the plotted vertical displacement, it switches signs when the daily water level has dropped below the water level at the start of our defined seasonal cycle. The horizontal response curves in Figure 7 show that the non-vertical crustal motion changes direction from

towards the center of load mass during water storage and downward flexural response to away from the center of load mass during periods in the seasonal cycle that are dominated by a reduction in water storage and subsequent reservoir withdrawals. This occurs simultaneously with the decrease in water storage and subsequent crustal relaxation for each seasonal cycle and begins after the maximum accumulated vertical displacement peak on the seasonal curves.

We note that the full vertical and horizontal displacement for each of the five average annual operational strategies (L1–L5) is 27, 27, 27, 23, and 20% and 24, 25, 24, 21, and 18% of the total maximum accumulated vertical and horizontal displacement from the entire GERD impoundment, respectively. In context, the vertical and horizontal percent differences for the highest amplitude year of the 39-year data cycle are 55, 52, 49, 55, and 38% and 47, 45, 43, 48, and 34%, respectively. The overall magnitude of the vertical and horizontal displacements for the five operational scenarios are highly varied when looking at both the average scenarios and the full 39-year runs. The deformation is dependent on the annual load density and the input natural hydrologic variables (e.g., inflow, seepage, actual ET) for that particular water year as well as the operational variables (i.e., outflow/reservoir release as it is related to hydropower generation) that the water managers decide upon. Subsequently, these varied reservoir inflow and outflow rates and release timings can dramatically affect the maximum accumulated seasonal displacement as well as the distance with which the flexural response occurs away from the associated hydrologic load centroid.

5. Conclusion

This study has compared the accuracy of several widely used DSMs to spaceborne laser altimetric products from the ICESat GLAS sensor in order to determine the most appropriate product for reservoir extent and volumetric calculations at the GERD. We utilized the ALOS-derived AW3D30 surface model to determine that the overall extent and total hydrologic load of the full GERD impoundment, which are ~1763.30 km^2 and 67.37 km^3 (Gt), respectively. We determined the areal extent and volumetric content for the GERD impoundment at 1 m water level increments (from 500 to 640 m) and derived hypsometric curves for water level versus areal extent and water load along with areal extent versus water load. We determined the most appropriate cubic and quadratic fits of these curves and found very high R-squared values for each. We utilized the associated coefficients to derive areal extent and volumetric content at sub-meter water level changes (e.g., 0.001 m) for each day in our scenarios.

We created daily water level, areal extent, water storage, inflow, and outflow values for 55 different filling scenarios as well as for 5 different operational strategies at the GERD. The time to full impoundment varies by scenario, and ranges from 1.6 to 76.7 years. We determined that the accumulated annual storage for these scenarios ranges from 0.9 to 48.3 km^3 at the longer end of impoundment time to the shorter end, respectively. A more realistic scenario is, of course, somewhere in between these values. The accumulated annual reservoir storage during the initial impoundment directly affects the time it takes to fill the reservoir to its maximum water level of 640 m. We found that the maximum seasonal amplitude of reservoir load changes for each of the five operational strategies to consist of 54, 54, 52, 51, and 41% of the total accumulated water volume from the full impoundment. When compared with the

percentages from the average annual operational strategies of 25, 34, 34, 34, and 29%, it becomes quite evident that reservoir operations have a large effect on the amplitude of seasonal hydrologic load fluctuations.

We found the maximum accumulated vertical and horizontal displacements caused by the hydrologic load from the full GERD impoundment to be 11.99 and 1.99 cm, and that the vertical and horizontal displacements in excess of 1 cm extend out to ~99 and 49 km from the 640 m weighted hydrologic load centroid, respectively. We derived the daily accumulated vertical and horizontal displacements for 22 of the 55 filling scenarios. Although the total magnitude of the elastic vertical and horizontal displacements are the same for each of the filling scenarios, it is the timing of these forces that play a role in the temporal dynamics of the load-induced flexural response. We note that the marked seasonal hydrologic regime at the GERD impoundment plays a major role in the timing of the deformation, and this is evidenced by the fact that 8 of the 22 filling scenarios (*A45-55*, *AW45-55*, and *AD45-50*) have nearly 50% (~6 and ~1 cm) of their total accumulated (~12 and ~2 cm) vertical and horizontal displacements (respectively) within the last half of the first year of the filling scenario.

We found that the maximum accumulated vertical (and horizontal) displacement for each of the largest seasonal amplitudes of hydrologic change from the full 39-year dataset for the five operational scenarios (L1 – L5) is 6.58 (9.39), 6.29 (8.94), 5.91 (8.45), 6.56 (9.58), and 4.61 cm (6.69 mm), respectively. The vertical and horizontal displacements in excess of 1 cm and 5 mm from these maximum amplitudes extend to ~78 and ~50 km (L1), ~93 and ~50 km (L2), ~93 and ~48 km (L3), ~78 and ~46 km (L4), and lastly ~78 and ~44 km (L5) from their respective maximum water level

weighted hydrologic load centroids. We compared this maximum seasonal displacement to the displacements from the full impoundment and found that the vertical and horizontal percent differences for the highest amplitude year of the 39-year data cycle for the five operational scenarios are 55, 52, 49, 55, and 38% and 47, 45, 42, 48, and 34%, respectively. We determined that the seasonal maximum and minimum vertical and horizontal displacements for all five operational scenarios over all 39 years of hydrologic data are 6.58 and 1.32 cm (vertical) and 9.58 and 1.91 mm (horizontal), respectively. We have shown that the overall magnitude of the vertical and horizontal displacements for the five operational scenarios are highly varied, and that the deformation is dependent on the input natural hydrologic variables (e.g., inflow, seepage, actual ET) for that particular water year as well as the operational variables (i.e., outflow/reservoir releases as they are related to hydropower generation) that the water managers decide upon. Subsequently, we noted that the annual load density along with the varied reservoir inflow and outflow rates and release timings can dramatically affect the maximum accumulated seasonal displacement as well as the distance with which the flexural response occurs away from the associated hydrologic load centroid.

Acknowledgments

We thank Stefan Liersch for kindly supplying his monthly hydrologic data. Some figures in this paper were made with Generic Mapping Tools (GMT) software. This work used computational and storage services associated with the Hoffman2 Shared Cluster

provided by the UCLA Institute for Digital Research and Education's Research Technology Group. We thank Frank Madson for his help in figure creation.

Supplementary Material

Separate File

Table S1. Areal extent and volumetric water loads for every meter of water level from 500 m to 640 m calculated from each of the five DSMs.

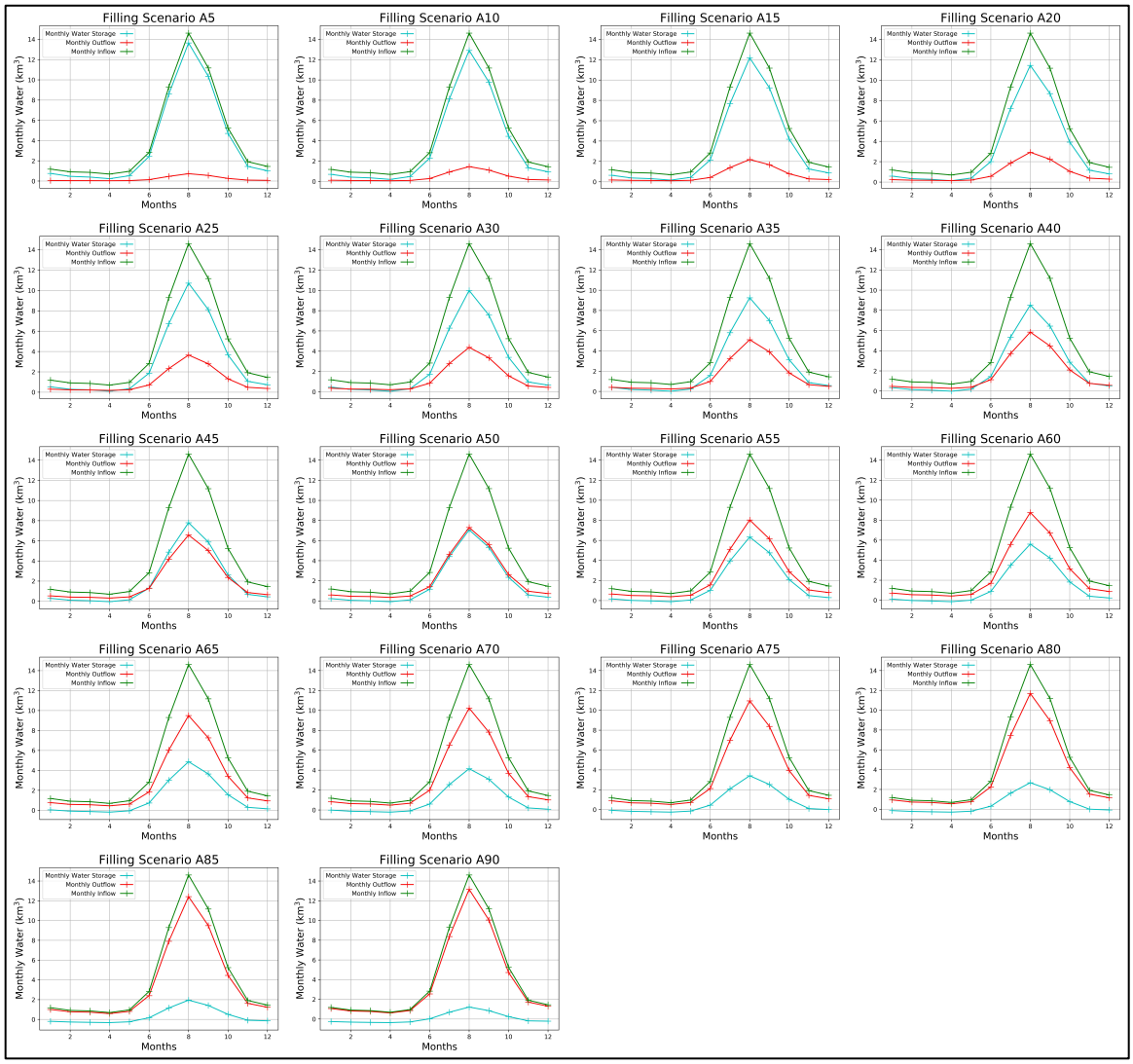

Figure S1. Monthly inflow, outflow, and water storage values for each of the average (A) water year impoundment scenarios. Note that integers after "A" in the sub-plot titles denote outflow rates as a percentage of the total inflow.

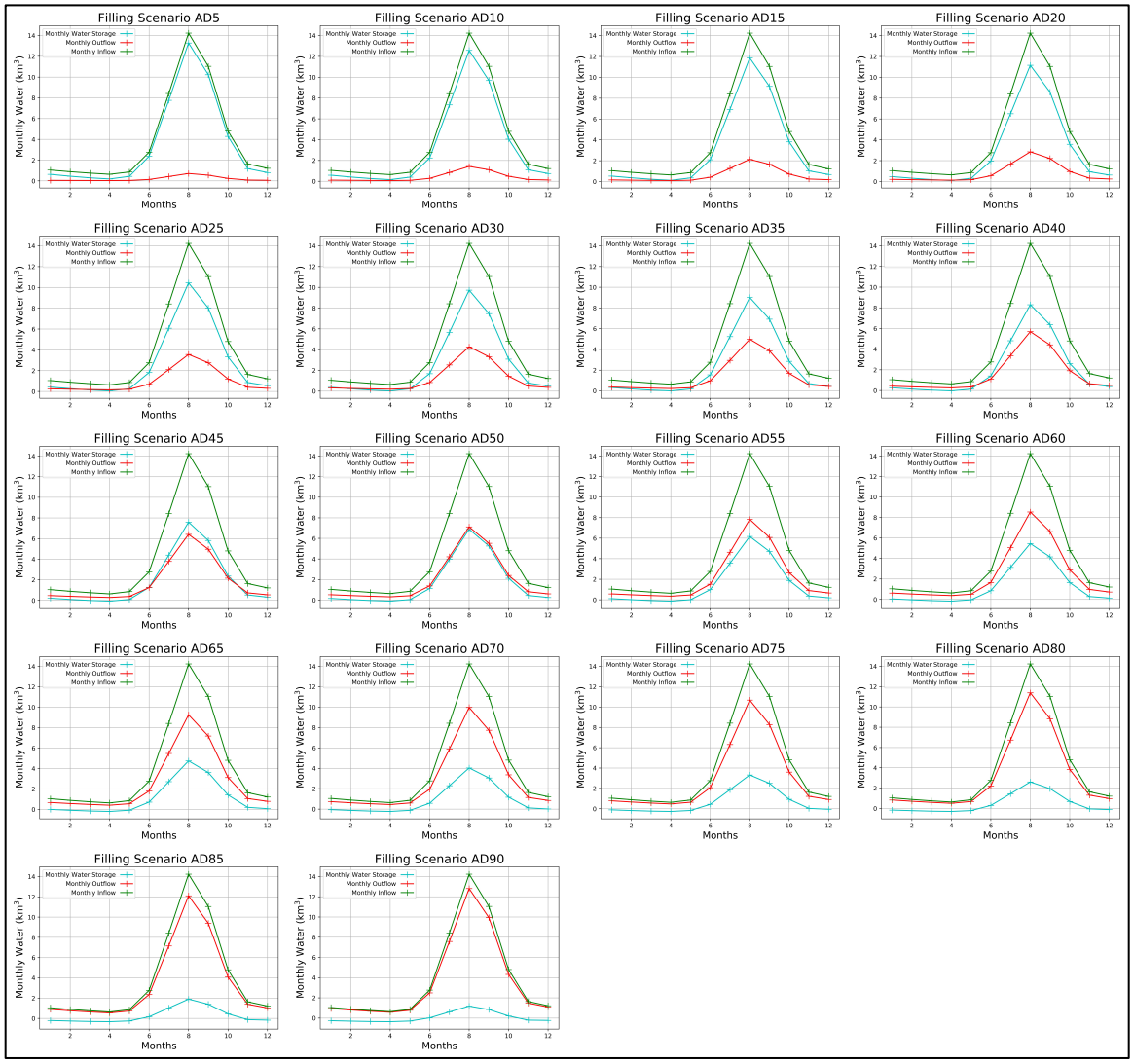

Figure S2. Monthly inflow, outflow, and water storage values for each of the average-dry (AD) water year impoundment scenarios. Note that integers after "AD" in the sub-plot titles denote outflow rates as a percentage of the total inflow.

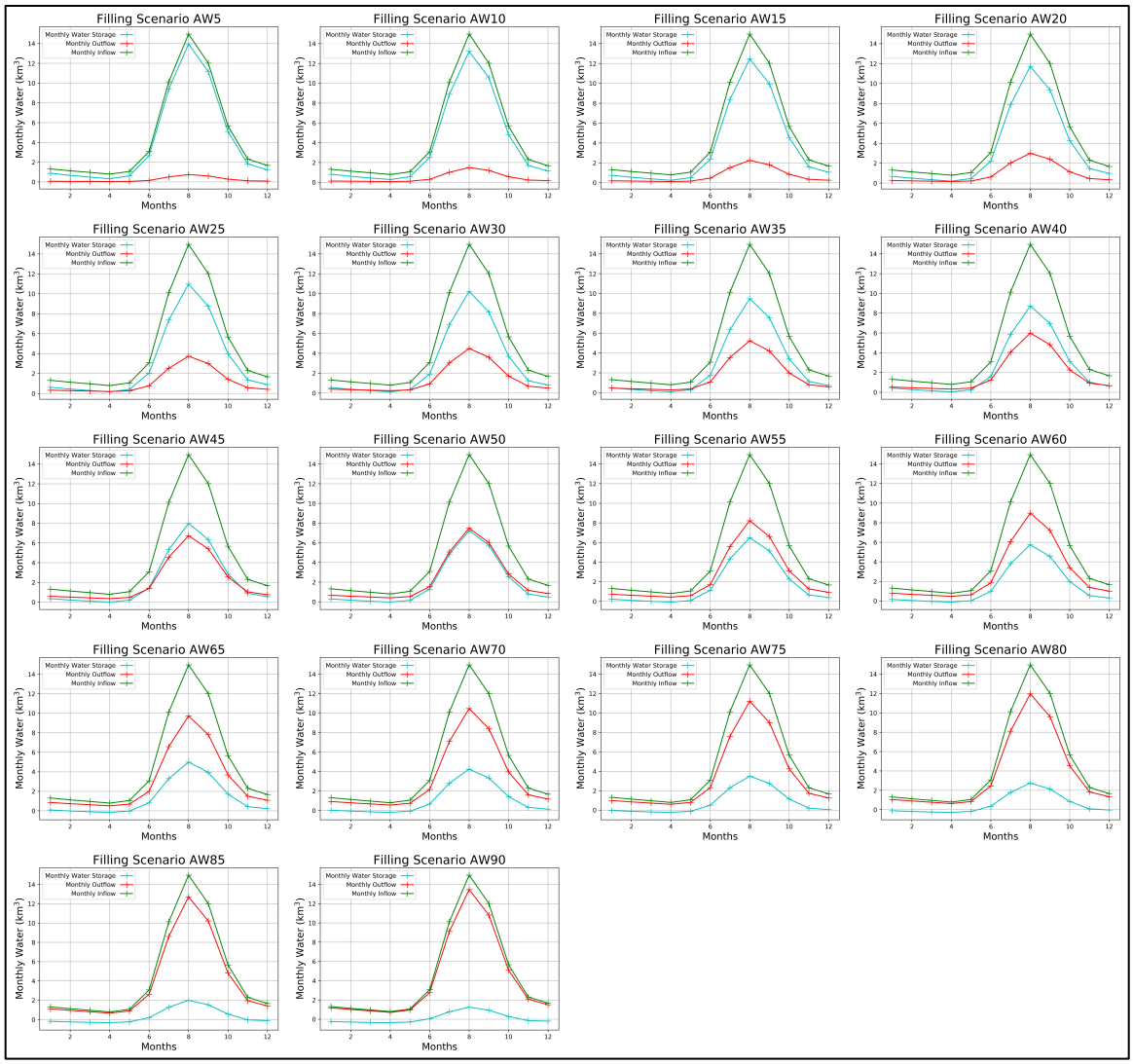

Figure S3. Monthly inflow, outflow, and water storage values for each of the average-wet (AW) water year impoundment scenarios. Note that integers after "AW" in the sub-plot titles denote outflow rates as a percentage of the total inflow.

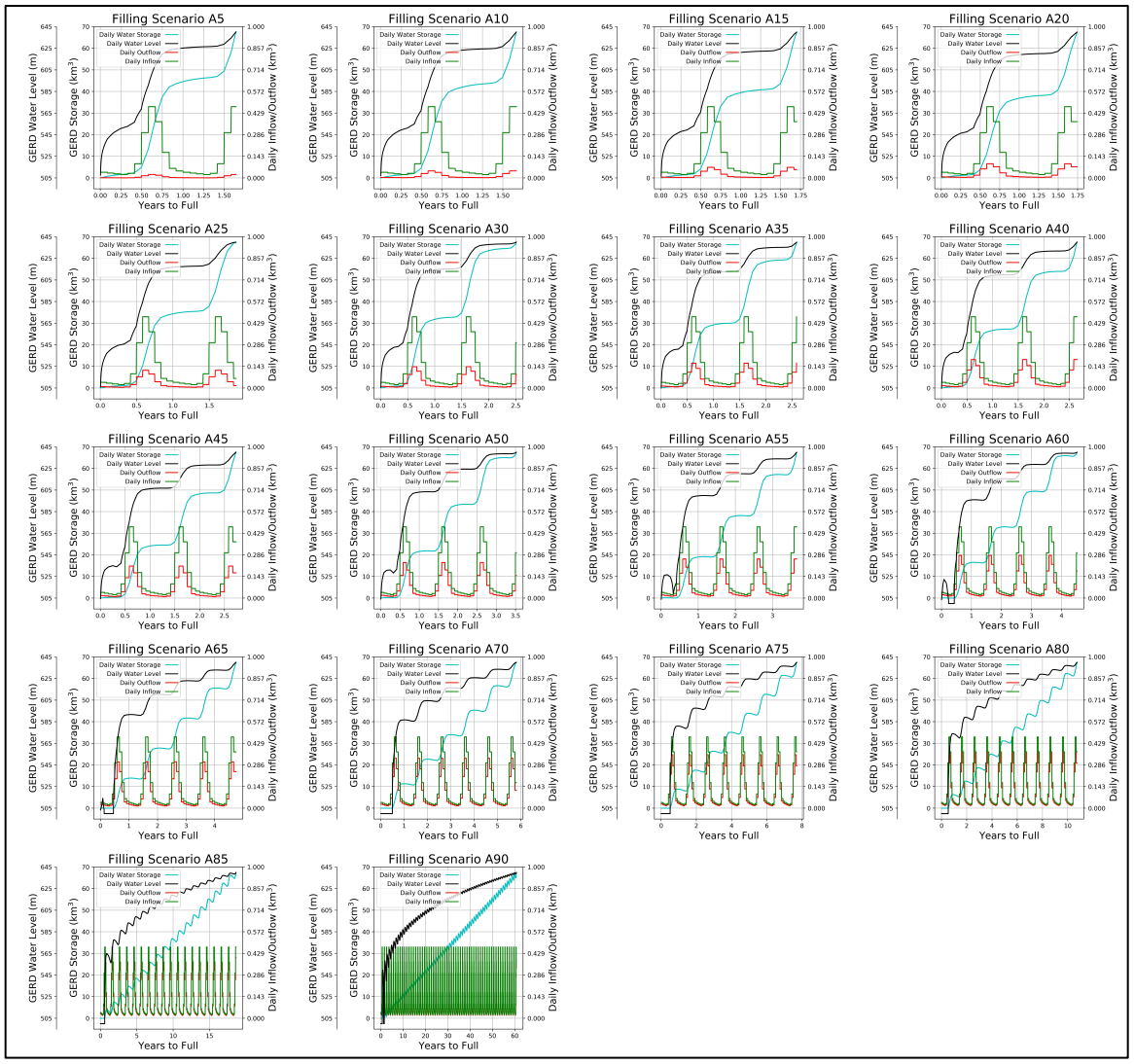

Figure S4. Daily reservoir inflows and outflows along with the accumulated water levels and hydrologic loads for each of the average (A) water year impoundment scenarios. Note that integers after "A" in the sub-plot titles denote outflow rates as a percentage of the total inflow. We set each accumulated water level that is less than the base reservoir elevation of 500 m to the actual base elevation of 500 m. The filling scenarios as plotted begin on the first of January, as we do not yet know when the actual filling will begin. If we started the scenarios on the first day of the year in which there is a positive

storage value then the years-to-full would simply be reduced by that day-number of the year.

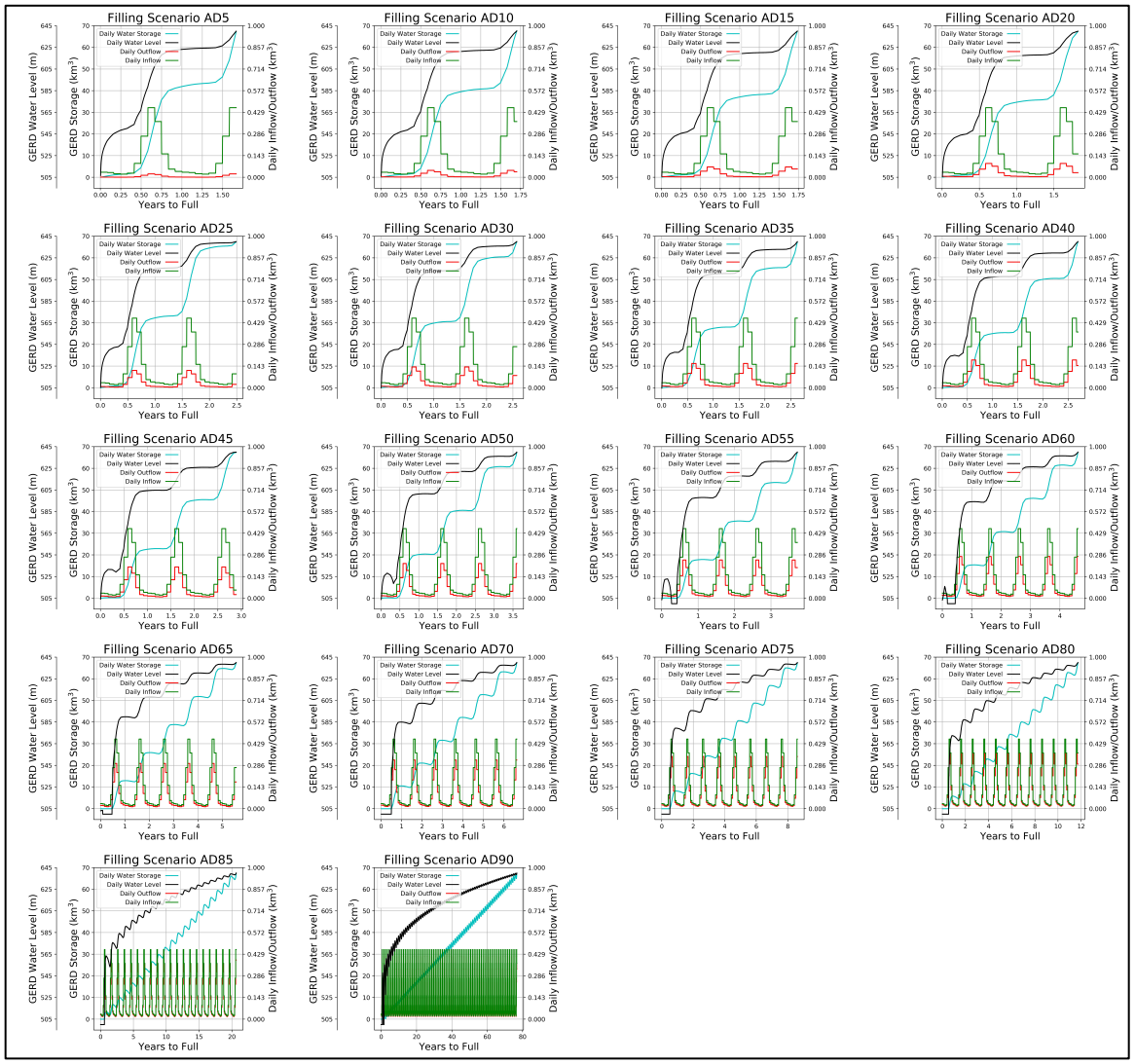

Figure S5. Daily reservoir inflows and outflows along with the accumulated water levels and hydrologic loads for each of the average-dry (AD) water year impoundment scenarios. Note that integers after "AD" in the sub-plot titles denote outflow rates as a percentage of the total inflow. We set each accumulated water level that is less than the base reservoir elevation of 500 m to the actual base elevation of 500 m. The filling

scenarios as plotted begin on the first of January, as we do not yet know when the actual filling will begin. If we started the scenarios on the first day of the year in which there is a positive storage value then the years-to-full would simply be reduced by that day-number of the year.

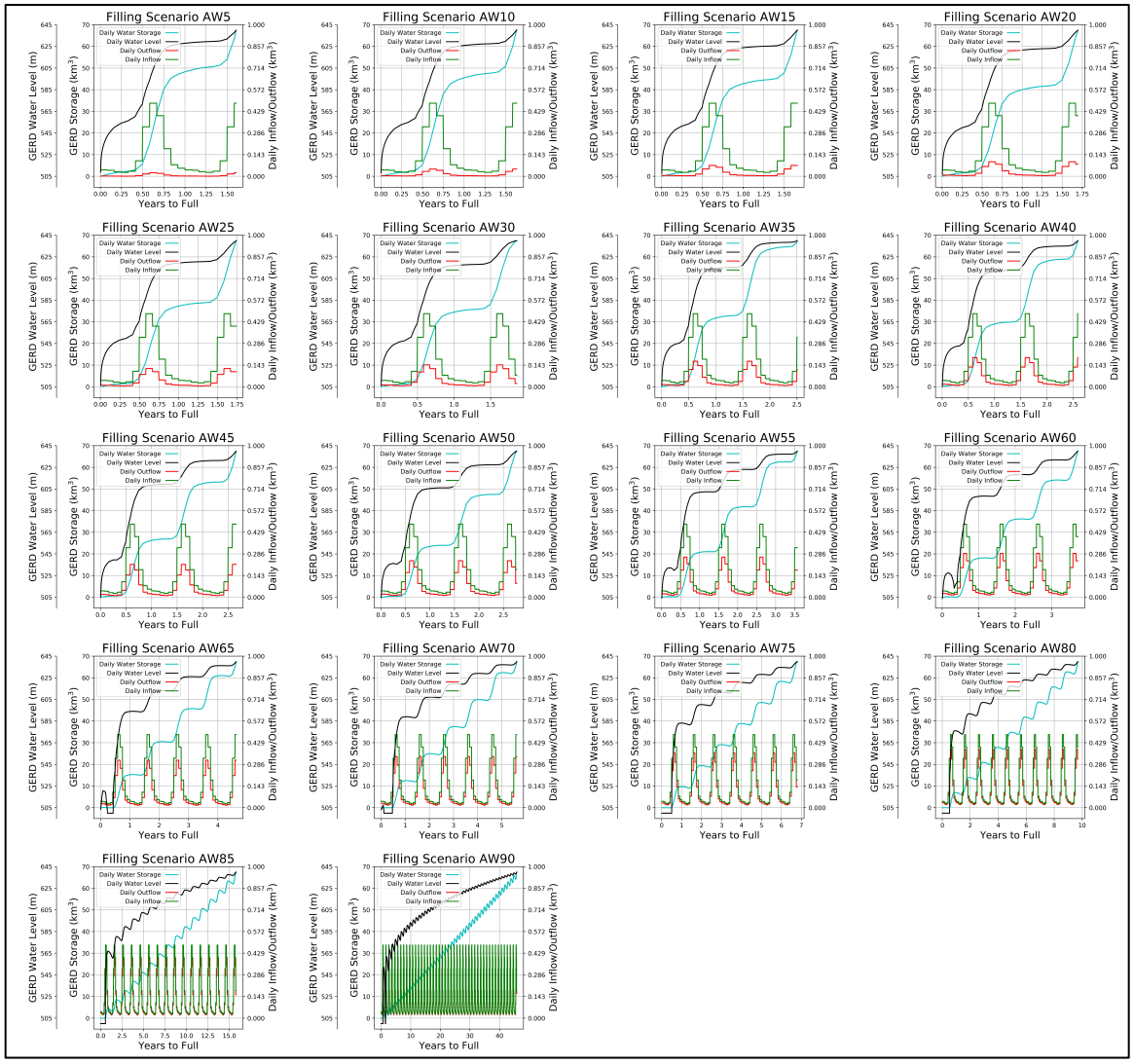

Figure S6. Daily reservoir inflows and outflows along with the accumulated water levels and hydrologic loads for each of the average-wet (AW) water year impoundment scenarios. Note that integers after "AW" in the sub-plot titles denote outflow rates as a

percentage of the total inflow. We set each accumulated water level that is less than the base reservoir elevation of 500 m to the actual base elevation of 500 m. The filling scenarios as plotted begin on the first of January, as we do not yet know when the actual filling will begin. If we started the scenarios on the first day of the year in which there is a positive storage value then the years-to-full would simply be reduced by that day-number of the year.

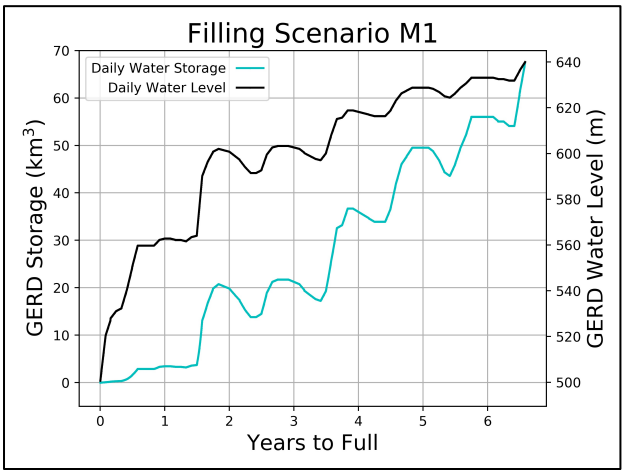

Figure S7. Daily accumulated water levels and hydrologic loads for the M1 impoundment scenario. We set each accumulated water level that is less than the base reservoir elevation of 500 m to the actual base elevation of 500 m. The filling scenario as plotted began on the first of January, as we do not yet know when the actual filling will begin. If we started the scenario on the first day of the year in which there is a positive storage value then the years-to-full would simply be reduced by that day-number of the year.

Separate File

Table S2. Annual outflow and inflow rates, accumulated reservoir storage, and the filling times for each impoundment scenario.

Separate File

Video S1. Animation displaying the flexural response along with the accumulated areal extent and hydrologic load for every meter of reservoir level rise from 500 m to the full impoundment of 640 m.

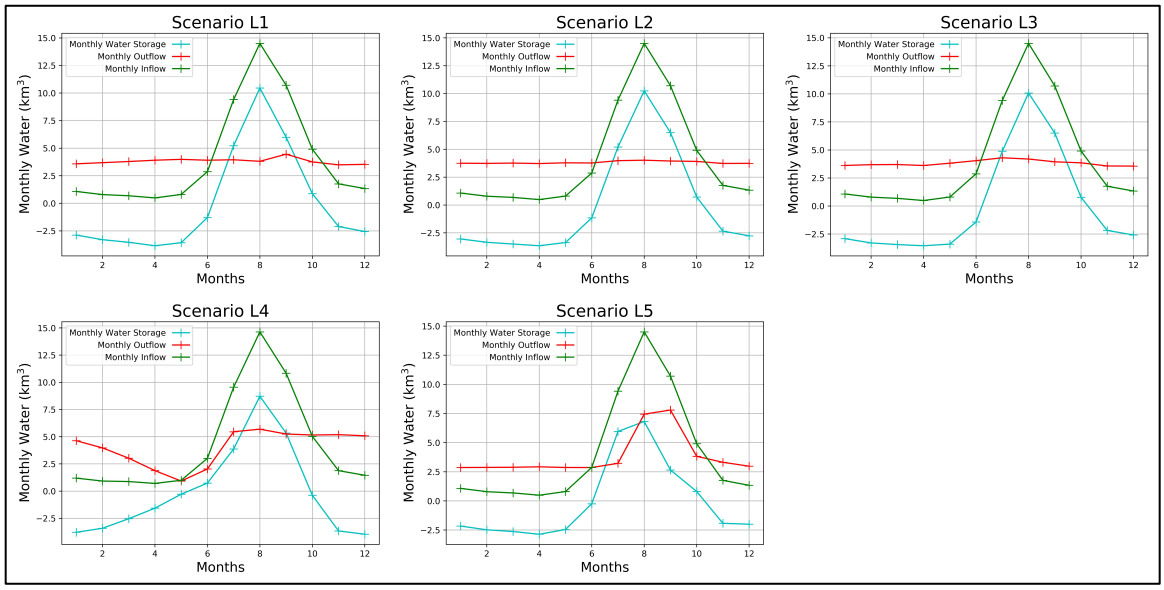

Figure S8. Average monthly inflow, outflow, and water storage values for each of the five seasonal reservoir operation strategies.

Separate File

Dataset S1. Zipped file containing vertical and horizontal displacement arrays for each of the 22 different filling scenarios. These are 1xNx3 arrays where N is the number of

days in the filling scenario and the three columns represent the day of the filling scenario, the vertical displacement (mm), and the horizontal displacement (mm).

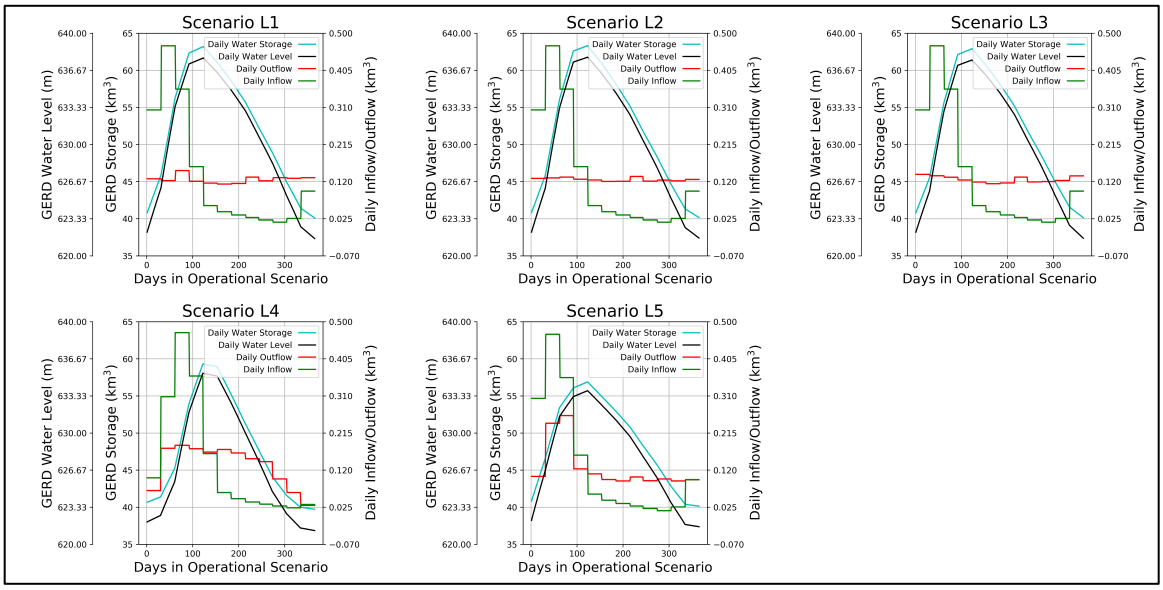

Figure S9. Average annual regime of daily reservoir inflow and outflow rates and the accumulated water levels and reservoir volumes for each of the five seasonal reservoir operation strategies**.**

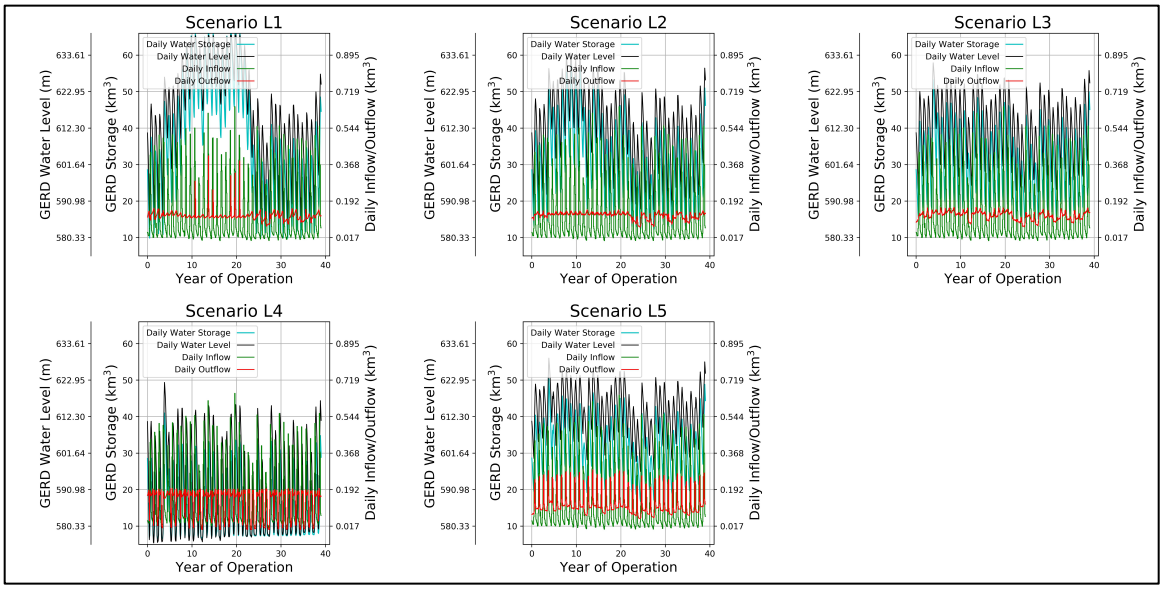

Figure S10. Daily water levels, water storage, and inflow and outflow rates for the five operational scenarios over their entire 39-year cycle.

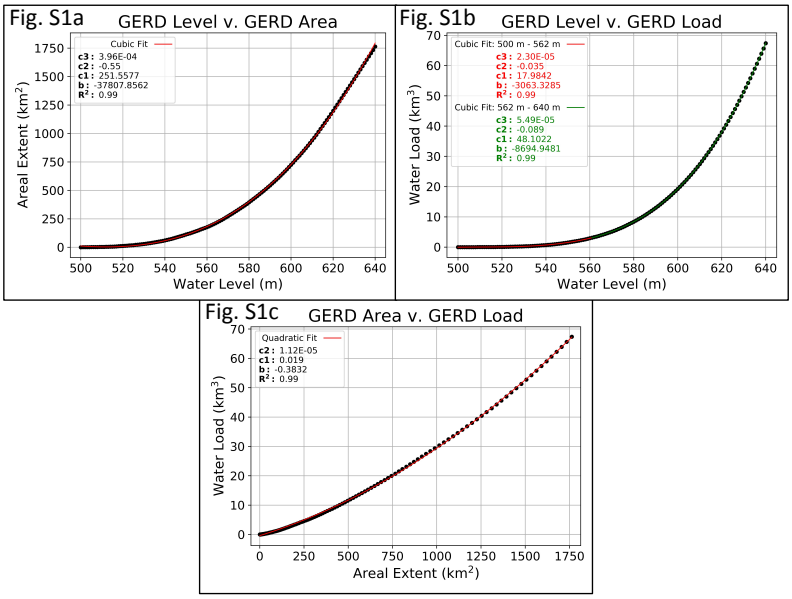

Figure S11. Hypsometric curves for water level versus areal extent and water load along with areal extent versus water load. Plotted here are the relationships between the GERD impoundment's water level versus the areal extent (a), the GERD impoundment's water level versus the hydrologic load (b), and the GERD impoundment's areal extent versus the hydrologic load (c). Also plotted are the cubic and quadratic fits alongside their associated coefficients and R-squared values. Note there are two fits in (b). This was undertaken to reduce the error when utilizing these relationships to derive reservoir volume during the early filling stages.

References

1. Zhang, Y., S.T. Erkyihum, and P. Block, *Filling the GERD: evaluating hydroclimatic variability and impoundment strategies for Blue Nile riparian countries.* Water international, 2016. **41**(4): p. 593-610.
2. Abtew, W. and S.B. Dessu, *The Grand Ethiopian Renaissance Dam on the Blue Nile*. 2018, Springer.
3. Reclamation, U.S.B.o., *Land and Water Resources of the Blue Nile Basin, Ethiopia*. 1964: The Bureau.
4. Ahmed, A.T. and M.H. Elsanabary, *ENVIRONMENTAL AND HYDROLOGICAL IMPACTS OF GRAND ETHIOPIAN RENAISSANCE DAM ON THE NILE RIVER.*
5. Mulat, A.G., S.A. Moges, and M.A. Moges, *Evaluation of multi-storage hydropower development in the upper Blue Nile River (Ethiopia): regional perspective.* Journal of Hydrology: Regional Studies, 2018. **16**: p. 1-14.
6. Sharaky, A.M., K.H. Hamed, and A.B. Mohamed, *Model-Based Optimization for Operating the Ethiopian Renaissance Dam on the Blue Nile River.* 2017.
7. Liersch, S., H. Koch, and F.F. Hattermann, *Management Scenarios of the Grand Ethiopian Renaissance Dam and Their Impacts under Recent and Future Climates.* Water, 2017. **9**(10): p. 728.
8. Melesse, A.M., W. Abtew, and S.G. Setegn, *Nile River basin: ecohydrological challenges, climate change and hydropolitics*. 2014: Springer Science & Business Media.
9. Abtew, W., A.M. Melesse, and T. Dessalegne, *Spatial, inter and intra‐annual variability of the Upper Blue Nile Basin rainfall.* Hydrological Processes: An International Journal, 2009. **23**(21): p. 3075-3082.

10. Wheeler, K.G., et al., *Cooperative filling approaches for the grand ethiopian renaissance dam.* Water international, 2016. **41**(4): p. 611-634.

11. Beyene, A., *Reflections on the Grand Ethiopian Renaissance Dam.* Horn of Africa News, 2013. **14**.

12. Zhang, L., et al., *Impact of impoundment on groundwater seepage in the Three Gorges Dam in China based on CFCs and stable isotopes.* Environmental earth sciences, 2014. **72**(11): p. 4491-4500.

13. Zhao, Y., et al., *Groundwater level prediction of landslide based on classification and regression tree.* Geodesy and Geodynamics, 2016. **7**(5): p. 348-355.

14. Paronuzzi, P., E. Rigo, and A. Bolla, *Influence of filling–drawdown cycles of the Vajont reservoir on Mt. Toc slope stability.* Geomorphology, 2013. **191**: p. 75-93.

15. Zhang, M., Y. Dong, and P. Sun, *Impact of reservoir impoundment-caused groundwater level changes on regional slope stability: a case study in the Loess Plateau of Western China.* Environmental earth sciences, 2012. **66**(6): p. 1715-1725.

16. Fredlund, D.G. and H. Rahardjo, *Soil mechanics for unsaturated soils*. 1993: John Wiley & Sons.

17. Xia, M., et al., *Relationship between landslide stability and reservoir water level variation.* Bulletin of Engineering Geology and the Environment, 2015. **74**(3): p. 909-917.

18. Allen, C.R., *Reservoir-induced earthquakes and engineering policy.* Revista Geofísica, 1980. **13**: p. 20-24.

19. Talwani, P., *On the nature of reservoir-induced seismicity*, in *Seismicity Associated with Mines, Reservoirs and Fluid Injections*. 1997, Springer. p. 473-492.

20. Kerr, R.A. and R. Stone, *A human trigger for the great quake of Sichuan?* Science, 2009. **323**(5912): p. 322-322.

21. Ge, S., et al., *Did the Zipingpu reservoir trigger the 2008 Wenchuan earthquake?* Geophysical Research Letters, 2009. **36**(20).

22. Gahalaut, K., et al., *Influence of Tehri Reservoir Impoundment on Local Seismicity of Northwest Himalaya.* Bulletin of the Seismological Society of America, 2018. **108**(5B): p. 3119-3125.

23. Chander, R. and K. Chander, *Probable influence of Tehri reservoir load on earthquakes of the Garhwal Himalaya.* Current science, 1996: p. 291-299.

24. Enzminger, T.L., E.E. Small, and A.A. Borsa, *Accuracy of snow water equivalent estimated from GPS vertical displacements: A synthetic loading case study for western US mountains.* Water Resources Research, 2018. **54**(1): p. 581-599.

25. Tregoning, P., et al., *Detecting hydrologic deformation using GRACE and GPS.* Geophysical Research Letters, 2009. **36**(15).

26. Dumka, R., et al., *GPS Measurements of Deformation Caused by Seasonal Filling and Emptying Cycles of Four Hydroelectric Reservoirs in India.* Bulletin of the Seismological Society of America, 2018. **108**(5B): p. 2955-2966.

27. Neelmeijer, J., et al., *Ground Deformations around the Toktogul Reservoir, Kyrgyzstan, from Envisat ASAR and Sentinel-1 Data—A Case Study about the Impact of Atmospheric Corrections on InSAR Time Series.* Remote Sensing, 2018. **10**(3): p. 462.

28. Madson, A., Y. Sheng, and C. Song, *ICESat-derived lithospheric flexure as caused by an endorheic lake's expansion on the Tibetan Plateau and the comparison to modeled flexural responses.* Journal of Asian Earth Sciences, 2017. **148**: p. 142-152.

29. Gahalaut, V., et al., *InSAR and GPS measurements of crustal deformation due to seasonal loading of Tehri reservoir in Garhwal Himalaya, India.* Geophysical Journal International, 2017. **209**(1): p. 425-433.

30. Borsa, A.A., D.C. Agnew, and D.R. Cayan, *Ongoing drought-induced uplift in the western United States.* Science, 2014. **345**(6204): p. 1587-1590.

31. Kraner, M.L., W.E. Holt, and A.A. Borsa, *Seasonal nontectonic loading inferred from cGPS as a potential trigger for the M6. 0 South Napa earthquake.* Journal of Geophysical Research: Solid Earth, 2018. **123**(6): p. 5300-5322.

32. Tadono, T., et al., *Precise global DEM generation by ALOS PRISM.* ISPRS Annals of the Photogrammetry, Remote Sensing and Spatial Information Sciences, 2014. **2**(4): p. 71.

33. NASA/METI/AIST/Japan Spacesystems, a.U.S.J.A.S.T., *ASTER Global Digital Elevation Model.* 2009, NASA EOSDIS Land Processes DAAC.

34. Farr, T.G., et al., *The shuttle radar topography mission.* Reviews of geophysics, 2007. **45**(2).

35. Zwally, et al., *GLAS/ICESat L2 Global Land Surface Altimetry Data.* Version, 2014. **34**.

36. Tadono, T., et al., *Generation of the 30 m-Mesh Global Digital Surface Model by ALOS PRISM* International Archives of the Photogrammetry, Remote Sensing & Spatial Information Sciences, 2016. **41**.

37. Laske, G., et al. *Update on CRUST1. 0—A 1-degree global model of Earth's crust*. in *Geophys. Res. Abstr*. 2013. EGU General Assembly Vienna, Austria.

38. Kustowski, B., G. Ekström, and A. Dziewoński, *Anisotropic shear‐wave velocity structure of the Earth's mantle: A global model.* Journal of Geophysical Research: Solid Earth, 2008. **113**(B6).

39. Chen, J., E. Pan, and M. Bevis, *Accurate computation of the elastic load Love numbers to high spectral degree for a finely layered, transversely isotropic and self-gravitating Earth.* Geophysical Journal International, 2017. **212**(2): p. 827-838.

40. Pan, E., et al., *An analytical solution for the elastic response to surface loads imposed on a layered, transversely isotropic and self-gravitating Earth.* Geophysical Supplements to the Monthly Notices of the Royal Astronomical Society, 2015. **203**(3): p. 2150-2181.

41. Love, A.E.H., *Some Problems of Geodynamics: Being an Essay to which the Adams Prize in the University of Cambridge was Adjudged in 1911*. 1911: CUP Archive.

42. Munk, W.H. and G.J. MacDonald, *The rotation of the earth: a geophysical discussion.* The rotation of the earth: a geophysical discussion., by Munk, WH; MacDonald, GJF. First published 1960. Cambridge (UK): Cambridge University Press, 19+ 323 p., 1975.

43. Farrell, W., *Deformation of the Earth by surface loads.* Reviews of Geophysics, 1972. **10**(3): p. 761-797.

44. Melini, D., et al., *a Regional ElAstic Rebound calculator.* 2015.

45. Melini, D., et al., *REAR—A Regional ElAstic Rebound calculator, User manual for version 1.0*. 2014.

46. Kaufmann, G. and F. Amelung, *Reservoir‐induced deformation and continental rheology in vicinity of Lake Mead, Nevada.* Journal of Geophysical Research: Solid Earth, 2000. **105**(B7): p. 16341-16358.

47. Wang, H., *Surface vertical displacements and level plane changes in the front reservoir area caused by filling the Three Gorges Reservoir.* Journal of Geophysical Research: Solid Earth, 2000. **105**(B6): p. 13211-13220.

48. Mulat, A.G. and S.A. Moges, *Assessment of the impact of the Grand Ethiopian Renaissance Dam on the performance of the High Aswan Dam.* Journal of Water Resource and Protection, 2014. **6**(06): p. 583.

49. IPoE *International Panel of Experts (IPoE). Grand Ethiopian Renaissance Dam Project, Final Report.* 2013.

50. Jameel, A.L., *The Grand Ethiopian Renaissance Dam: An Opportunity for Collaboration and Shared Benefits in the Eastern Nile Basin.* World Water and Food Security Lab, Amicus Brief, 2014: p. 1-17.

Chapter 2: Reservoir Induced Stress Analysis for Several Filling and Operational Scenarios at the Grand Ethiopian Renaissance Dam Impoundment

Abstract

Increased demand for power generation coupled with changing seasonal water uncertainty have caused a global rise in large-scale hydrologic engineering projects. To that end, the soon-to-be-completed Grand Ethiopian Renaissance Dam (GERD) will impound the Blue Nile in Ethiopia and its reservoir will have an areal extent of ~1763 km^2 and store ~67 Gt (km^3) of water. The impoundment will undergo maximum seasonal load changes of ~28 – ~36 Gt during projected seasonal hydroelectric operations. The GERD impoundment will cause significant subsurficial stresses, and could possibly trigger seismicity in the region. This study examines Coulomb stress and hydrologic load centroid movements for several GERD impoundment and operational scenarios. The maximum subsurficial Coulomb stress applied on optimally oriented fault planes from the full impoundment is ~186 kPa and over 30% of our model domain incurs Coulomb stresses ≥ 10 kPa, regardless of the impoundment period length. The main driver behind Coulomb stress and load centroid motion during impoundment is the annual, accumulated daily reservoir storage change. The maximum Coulomb stresses from the highest amplitude season of five long-term operational scenarios are around 36, 33, 29, 41, and 24% of the total maximum stresses from the entire GERD impoundment. Variations in annual Coulomb stresses during modeled GERD operations are attributed to the seasonal load per unit area, and partially to the initial seasonal

water level. The spatial patterns and amplitudes of these stress tensors are closely linked to both the size and timing of GERD inflow/outflow rates, and an improved understanding of the magnitude and extent of these stresses provides useful information to water managers in order to better understand potential reservoir triggered seismic events from several different operational and impoundment strategies.

1 Introduction

The Grand Ethiopian Renaissance Dam (GERD) is located on the Blue Nile in Ethiopia around 15 km east (upstream) of the Sudanese border and is slated for completion within the next few years [1, 2]. The GERD build site was one of four initially identified in the 1960's during a United States Bureau of Reclamation survey [3]. The main dam is located at 11.215° N, 35.092° E (Figure 1) and sits near the pour point of the Upper Blue Nile Basin, a large watershed with an areal extent of ~175,000 km^2. The Blue Nile originates at Lake Tana and drains the notable Ethiopian Highlands into the GERD impoundment and further towards the confluence with the White Nile. Work on the dam began in 2011and will be the largest dam in Africa upon its completion. The GERD project consists of a 150 m tall and 1800 m long roller compacted concrete gravity main dam along with an adjacent rock-filled saddle dam that is ~50 m tall and 5 km long. The saddle dam increases the water level of the impoundment to ~640 m above mean sea level [4-6]. The Blue Nile River Basin provides about 58 - 62% of the total water supply to downstream Nile River flows [7]. Flow data from the National Meteorological Agency of Ethiopia for the Blue Nile at the Sudanese/Ethiopian border

has a historical (1967–1972; 1999–2003) mean of ~50 Gt where ~80% of the flow occurs in the months of July through October [2, 8, 9].

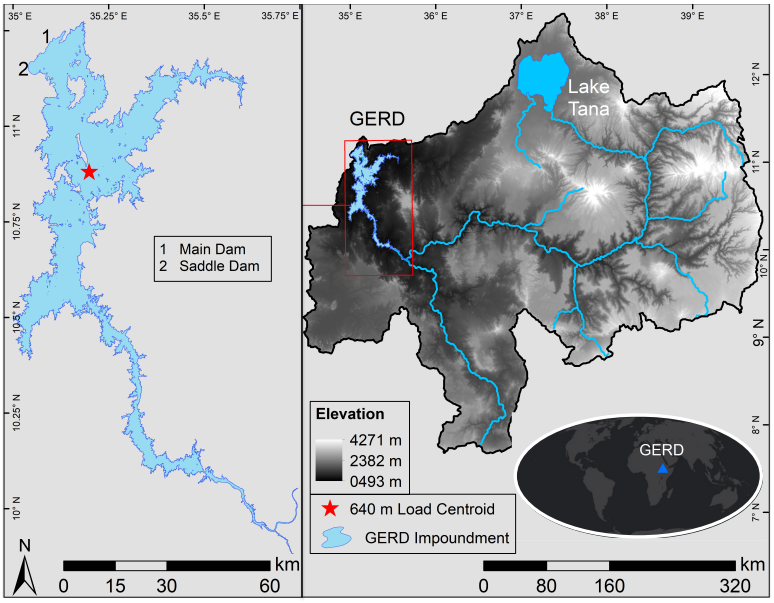

Figure 1. Overview of the GERD impoundment study area. The elevation of the Upper Blue Nile Basin is plotted on the right, as is the global overview of the general location of the GERD. The areal extent of the entire GERD impoundment (at the 640 m reservoir level) is plotted on the left, as is the weighted hydrologic load centroid for the entire water volume of the reservoir. The main dam and the saddle dam are also labeled. Reprinted from [10]

The large impoundment of the Blue Nile behind the GERD will have a multitude of different impacts. For example, the annual Blue Nile discharge curve will be severely affected from the GERD's construction and the subsequent large volume of impoundment water. The large capacity of the reservoir allows for a near-equal Blue Nile discharge rate for each month of the year. This will allow for the reduction of both high and low Blue Nile flow events [7]. There will likely be a decrease in the region's

hydrologic uncertainty owing to the reduction of drought and flood events. We note that the GERD is not the first major impoundment on the Blue Nile or the Nile itself. However, the GERD's upstream location combined with the large size of the reservoir will likely have an affect on downstream hydrologic engineering projects. As an example, three downstream dams (Rosaries, Sennar, and Aswan High) will likely need to modify their outflow release operations so that Sudanese agricultural water supplies will be maintained [11]. Further, the filling and operation of the GERD impoundment will likely affect downstream hydrologic power generation. This potential reduction of power generation will be directly related to the filling and operational scenarios that the GERD water managers decide upon [6, 11, 12].

It is also likely that groundwater levels will be impacted by the GERD impoundment and the ensuing reservoir operations. That said, reservoirs can cause seepage into the subsurficial rock as well as the connected aquifer systems. This diffusion of surface water into underlying rock is able to increase pore pressure and reduce frictional stresses. Further, impoundment and the subsequent operational strategies of large dams (e.g., Three Gorges) have been shown to directly alter groundwater levels for hydraulically connected aquifer systems [13, 14]. These connections have the capability to decrease slope stability, which can trigger slope failure events. This is caused by the changes in hydrostatic pressure from the varying groundwater levels and the hydraulically connected reservoir water levels [15-18].

Additional impacts from the GERD impoundment are associated with the large hydrologic loading forces applied on the reservoir-adjacent lithosphere. Extreme changes in surface loads caused by large hydro-engineering projects (e.g. the Aswan

High Dam and the Three Gorges Reservoir in China) can have far reaching implications for increased stress and strain on surrounding fault systems and subsequent seismicity [19-24]. The initial GERD impoundment and subsequent reservoir creation as well as seasonal fluctuations in water level due to hydro-operational phases will cause large fluctuations in both areal extent and volumetric content of the reservoir. These marked changes in hydrologic loads can impart large forces on the surface of the Earth and are capable of deforming the lithosphere [10]. For example, several studies have shown that remotely sensed and *in situ* products (e.g. InSAR, GNSS, GRACE, etc.) have the capability to quantify the flexural response from changes in hydrologic loads (drought, lakes, regional climatic changes, reservoirs, seasonal precipitation, snow, etc.) [25-32]. The vast size of the GERD project allows for a marked influx of water into the upstream reservoir area during the initial impoundment stages as well as during normal seasonal hydro-operations. These loads are highly dependent on the filling and operational strategies that are selected by the local/regional water managers. Both the initial impoundment stages and the subsequent operational scenarios play important roles in the application of hydrologic load induced lithospheric stress for an impoundment of such a large size.

A drastic influx of water into a reservoir can apply large stresses on the region as well as significantly increase the pore pressure in the surrounding areas [33]. Dozens of cases of post-impounding seismicity have been researched over the last several decades, and these topics are of great concern for a large reservoir like the GERD impoundment. [34-46]. However, understanding these reservoir triggered seismic (RTS) events is not straightforward. For example, in some cases the increased RTS activity

occurs during the filling stages, while other large reservoir projects have documented increases only after an impoundment is complete and several seasonal operational phase cycles have been completed [20, 47]. There are two dominant mechanisms responsible for RTS: (1) increased normal and shear stress from the elastic response to the hydrologic loading and/or unloading and (2) increased pore pressure from a reduction in effective normal stresses [20, 35, 42, 47-49]. However, the stress changes from the elastic response can also be a stabilizing factor for the underlying and reservoir-adjacent regions, but this is dependent on the overall geometry of the impoundment relative to nearby faults as well as the preexisting stressors in the study area [46, 50].

This study will focus on changes in normal ($\sigma\beta$) and shear ($\tau\beta$) stresses brought on by different impoundment scenarios and seasonal operations at the GERD site. More specifically, this work examines changes in Coulomb stress from the GERD's hydrologic load on optimally oriented planes in an elastic half-space. Typically, fault plane failures occur when Coulomb stresses exceed a certain threshold [51-53]. That said, a robust analysis of spatiotemporal changes in Coulomb stress helps to provide a meaningful assessment on the potential of triggered seismic events from different reservoir impoundment and operational strategies. These changes in the Coulomb stress state are mostly dependent on the frequency and amplitude of the reservoir fluxes as they relate to the initial filling stages as well as the subsequent operation of the reservoir. This highlights the need for a better understanding of the predicted subsurficial stress fields at the GERD as it relates to the creation of a well thought out

and appropriately timed impoundment/filling strategy along with a reasonable operational reservoir cycle.

This study seeks to provide a first look at the Coulomb stress on optimal fault orientations brought on by the initial GERD impoundment along with reservoir operations from several predicted seasonal release plans. This work was undertaken in order to glean a better understanding of the amplitude and spatiotemporal dynamics of the load-induced stress at and around the GERD study site. In order to accomplish this task we seek to answer the following questions: (1) What are the Coulomb stresses at depth on optimally oriented fault planes as caused by hydrologic loading variations from long-term reservoir operations and multi-year reservoir filling schedules at the GERD? (2) What are the main hydrologic factors that affect these subsurficial stresses? We utilize daily hydrologic load arrays from several filling and operational scenarios to derive Coulomb stresses on optimal planes in a 3D elastic half-space to answer (1), and we investigate the relationships between both load area density and starting reservoir water levels with Coulomb stress results to answer (2).

2 Data and Methods

2.1 Impoundment plans, operational scenarios, and centroids

A filling plan has not yet been finalized for the GERD project. That said, we have focused our input water load calculations and subsequent initial impoundment stress modeling on representative filling scenarios as laid out in Mulat, Moges [5] and Liersch, Koch [7]. Mulat, Moges [5] utilized an 80-month impoundment strategy that is based on natural inflow rates from 1973 – 1978. The mean annual inflow of this impoundment is

only ~0.5% more than the 41-year mean annual inflow of ~50 Gt (1961 – 2002), and the annual outflow during this initial impoundment does not fall below 28.9 Gt. We utilized the monthly water level values from the above-cited paper to derive filling scenario *M1*. We point the reader to [10] for an in-depth look at how we derived the *M1* filling scenario. Liersch, Koch [7] derived monthly actual evapotranspiration (ET), inflow, outflow, precipitation, and seepage (in m^3s^{-1}) at the GERD impoundment for 39 years (January 1961 to the end of December 1999). We utilized these 468 monthly hydrologic observations to determine mean monthly inflow datasets based on three types of water years (Average: 1961-1999, Average Wet: 1961-1981, and Average Dry: 1981-1999). The monthly GERD outflow rates from these three sets of inflow values were then derived as a percentage of the total inflow from 5% to 90% at 5% intervals. We note that an outflow percentage value of 5 means that only 5% of the daily inflow at the GERD is allowed to flow through the dam outlets as outflow (i.e. 95% storage). The monthly reservoir storage was determined for each of the three types of water years and their 18 different percentages of inflow rates from 5% to 90%. These monthly hydrologic observations were utilized to determine daily water levels for each scenario. From here on we call these filling scenarios *A5 – A90* (Average), *AW5 – AW90* (Average Wet), and *AD5 – AD90* (Average Dry), respectively. Again, we point the reader to [10] for an in-depth look at how we derived the *A5 – A90*, *AW5 – AW90*, and *AD5 – AD90* filling scenarios. These cell-by-cell water level arrays for each of the 55 different impoundment scenarios (54 derived from Liersch, Koch [7] and one scenario derived from Mulat, Moges [5]) were utilized to derive the initial impoundment load grids that are used as inputs into our stress model that is discussed in the following section.

Similarly, seasonal operation plans have not yet been finalized for the GERD. That said, we have focused our annual stress modeling on the five operational strategies as discussed in Liersch, Koch [7]. From here on we call these five operational scenarios *L1 – L5* and point the reader to [10] for a detailed definition of these five scenarios. These five operational strategies consist of monthly actual ET, inflow, outflow, precipitation, and seepage (in m^3s^{-1}) at the GERD impoundment from January 1961 to the end of December 1999 (39 years). From these monthly datasets we derived two temporally different sets of overall inflow, outflow, and storage values for each of the five scenarios. The first of these two temporally different datasets is comprised of a single-year's inflow, outflow, and water storage as calculated from the respective months' mean from the entire 39-year dataset, and the second consists of the entire 39-year hydrologic monthly dataset. These two temporally different datasets were used to create the operational load grids that are utilized as inputs into the stress model that is discussed in the following section. We point the reader to [10] for more information on these scenarios and how they were derived.

Marked changes in hydrologic loads during impoundment and seasonal operations cause notable variations in the location of the weighted load centroids. These centroids mark the location of the maximum load for any given water level and are an important variable with respect to spatiotemporal changes in the stresses applied on the underlying rocks. The motion of the load centroid can be thought of as a proxy for the changes in the location of where the maximum stresses are applied on the Earth's crust. The load grids for each water level of the impoundment (500 m to 640 m) from [10] were used to calculate the individual load centroids using a weighted mean

center algorithm where the weight of the cell is assigned the water level at that location. The daily water levels for each of the 55 different impoundment scenarios from the same study were employed to calculate the accumulated annual load centroid motion for each filling scenario. The weighted load centroid location for each daily reservoir level in the filling scenario was linearly interpolated by using the two surrounding water levels' weighted load center and the fractional part of the daily water level value. The distances between these daily load centroid locations were then accumulated for each 365-day period for all of the 55 different impoundment scenarios. The total accumulated weighted load centroid motion for each impoundment scenario was also derived. Similarly, the daily-accumulated annual weighted load centroid motion was calculated for both of the two temporally different monthly datasets (the single year and the entire 39-year) for the five separate operational strategies discussed in the previous paragraph.

2.2 Coulomb Stress

The previously described hydrologic load arrays from [10] were used to calculate the Coulomb stress on an optimal plane for each full-resolution cell (~30 m x ~30 m) in the array at 1 km depth increments from the surface (0 km) down to 25 km. See Appendix I. We followed the method outlined in [54] to derive the stress fields as caused by the hydrologic loads from the GERD impoundment and operational scenarios. All calculations were undertaken in an elastic half-space with a model domain of 300 km x 300 km x 25 km and at the full cell resolution. The horizontal dimensions of the model domain were selected such that regions with marked Coulomb stresses from the full

impoundment would fall within the domain. For the subsequent calculations, both the first and second Lame's parameters were set to 1, which assumes a Poisson ratio of 0.25. The final six stress tensor fields from the hydrologic loads were derived from their vertical (Boussinesq [55]) and horizontal (Cerruti [56]) stress components, per [54]. To this end, altered scripts from [57] were utilized to calculate both of the horizontal and vertical components. The vertical stress component was derived by convolving the Boussinesq solutions as Green's functions with the full hydrologic load array [54]. We utilized a water density of 1000 kg/m^3 and a gravitational constant of 9.81 m/s^2 and took advantage of the superposition theorem to do the convolutions in the Fourier domain in order to speed up the calculations. The horizontal component consists of the two sets of stress fields from both the *x* and *y* horizontal surface tractions brought on by the vertical point load arrays on the half-space surface as calculated above. The two horizontal stress components were calculated by convolving the Cerruti solutions as Green's functions with their respective *x* or *y* loading function as derived from the appropriate surface traction for the full hydrologic load array [54]. Similar to the above vertical component, we utilized a water density of 1000 kg/m^3 and a gravitational force of 9.81 m/s^2 and took advantage of the superposition theorem to do the *x* and *y* horizontal convolutions in the Fourier domain. Lastly, the stress fields from the vertical loading component and the two *x* and *y* horizontal components were summed in order to derive the final stress tensor field for each water level in the GERD impoundment and operational scenarios.

Next, the angle of an optimally oriented fault plane was calculated for each cell in the grid by following [58] while utilizing a friction coefficient of 0.6. This is the angle at

which fault activation requires the lowest ratio of principal stress [59]. The stress tensor arrays as calculated above were then utilized to determine the strike and dip angles of the optimally oriented fault plane for each cell in the grid. Next, the stress tensor arrays and the strike and dip angles for the optimally oriented planes were utilized in order to derive the shear stress by taking the maximum value between the along-strike and down-dip shear stresses. The normal stress on the optimal plane was then determined with the same stress tensor along with the plane's orientation (strike and dip angles). Lastly, the abovementioned shear and normal stresses were used to calculate the effective Coulomb stress changes following the equations in [52]. A friction coefficient of 0.6 was used throughout and pore pressure was ignored (set to zero) in the calculations. Pore pressure was neglected in order to solely focus on the static stress effects from the changing hydrologic load, and not the reduction in the optimal fault planes' stability from the increased pore pressure and the subsequent reduction in frictional stresses caused by the diffusion of water into the underlying rock. We note that the friction coefficient utilized within our calculations (0.6) is somewhat conservative and allows for increased estimates of stability, and that a reduction in this parameter would have a destabilizing effect on our calculations of Coulomb stress. Further, the absence of the pore pressure parameter underestimates the results from our final Coulomb stress computations and that its inclusion into the calculation would further increase the overall instability (increased Coulomb stress values) of the optimal planes.

The workflow described in the preceding paragraph was followed in order to derive the effective Coulomb stress for each water level of the full impoundment (500 m to 640 m) in one meter increments. The Coulomb stress for each load array was also

calculated where the corresponding water level utilized in the input load file is the water level at which the areal extent was derived plus 1 m (501 m to 641 m). This was done so that the Coulomb stress for each daily reservoir level in the filling scenarios could be linearly interpolated by using the stress arrays of the two surrounding water levels and the fractional part of the daily water level value. For example, we derived the Coulomb stress arrays utilizing each cell from the 600 m water level areal extent along with the stress array from the same cells plus 1 m of water level (i.e. 601 m). This allowed us to calculate the daily Coulomb stress arrays from sub-meter water level changes (e.g. at 0.001 intervals between 600 m and 601 m) without having to run the computationally expensive stress calculations through many tens of thousands of iterations. The daily reservoir load files for each of the 55 different impoundment scenarios as described in Section 2.1 and the abovementioned stress arrays were utilized to derive the daily accumulated Coulomb stresses for each of the GERD filling scenarios. Lastly, the seasonal Coulomb stress arrays were derived for both the full 39-year dataset and the mean annual scenarios (as discussed in the previous section). We note that the mean annual operational scenarios were started on the first day of the first month in which there is a positive storage rate (i.e. *L1 - L3, L5*: July 1 and *L4*: June 1), and the annual cycles within the 39-year seasonal operational dataset were started on the first day in which there is a positive water storage. These seasonal stress arrays were derived using input load arrays calculated from the difference between the hydrologic loads at the beginning of the annual operational season and at the peak of the season.

3 Results and Discussion

3.1 Initial Impoundment

We focus our discussion on the 22 filling scenarios M1, A45-A75, AW45–AW75, and AD45–AD75 due to the increased filling times and the lower levels of accumulated annual outflow at the upper and lower end of the percentage scenarios, respectively (See [10]). The former is important for the operation and timing of the reservoir water management and the latter is important to negate downstream user impacts. The filling time is also an important parameter with respect to potential RTS where faster impoundments denote increased shear and normal stresses within a shorter time span while longer filling times may slow the drained response that is responsible for the increase of diffusive pore pressure through the underlying rock. We note that the filling scenarios each had a start date of January 1 and the first five months of each filling scenario shows little to no impoundment.

We were unable to locate regional seismogenic fault models in the area of the GERD impoundment due to a lack of available data, and, as such, were not able to derive Coulomb stress on known faults. Instead, we focused on the Coulomb stresses applied on optimally oriented faults within our study area. Further results and discussion on Coulomb stresses from the GERD impoundment and operational scenarios are based on the stress tensors as calculated on optimal faults within the region, and we point the reader to Section 2.2 for the overview of these calculations. That said, the stresses computed herein would likely be different if calculated on the actual seismogenic structures and would be dependent on their depth, location, and orientation with respect to the impoundment. Lastly, in the discussion that follows we are suggesting operational and filling strategies that are based on the results from these

optimally oriented planes, and that these suggestions are speculative in nature. Whether or not the hydrologic load from the GERD actually triggers local seismicity is dependent on if there are critically stressed faults already present within the study area, and that the changes in shear and normal stresses along with the potential subsurficial pore pressure increase is enough to decrease the stability of the seismogenic faults beyond their failure point.

The maximum subsurficial Coulomb stress derived on optimally oriented fault planes for the complete GERD impoundment as calculated from the methods and datasets described in Section 2.2 is ~186 kPa. We exclude the surficial Coulomb stresses to determine this maximum value and note that this maximum stress occurs at a depth of 1 km. The maximum Coulomb stress values range from ~1100 kPa at the surface of the model down to ~57 kPa at a depth of 25 km. In order to show the spatial extent of non-negligible stresses from the full impoundment we calculated the number of cells at each depth that have a Coulomb stress value ≥ 10 kPa. Coulomb stress increases in excess of 10 kPa are considered to be the threshold at which seismicity is affected [53, 60]. These depth-accumulated values are plotted in Figure 2a along with six example cross sections of the Coulomb stress fields (Figure 2b) for the full GERD impoundment (500 m to 640 m). We provide the Coulomb, normal, and shear stress arrays from the full GERD impoundment and for each depth (0 km to 25 m) in our model in Movie S1. The location of the maximum Coulomb stress for each depth is plotted in the animation as a white cross and the contour lines denote the location of the 10 kPa Coulomb stress regions. The darkest red regions in Figure 2a show that the area immediately adjacent to the main body of the full impoundment incurs Coulomb stresses

≥ 10 kPa at all depths in our model (0 km to 25 km), and a closer look at cross sections for A – 'A, B – 'B, C – 'C, and E – 'E in Figure 2b shows detailed views along the depth axis in which this is the case. We reiterate that these are Coulomb stress arrays on idealized fault planes within our model regime.

In order to appropriately investigate and compare the timing of the stress state changes for the 22 filling scenarios we derived the daily depth-accumulated percentage of cells that have a Coulomb stress ≥ 10 kPa. These percentages include the Coulomb stresses at the surface of the model (0 km) and we note that the temporal pattern for the individual filling scenarios would be the same as if they were derived from all depths sans the surface (albeit with slightly lower percentages as caused by the removal of the surficial stress cells). The daily depth-accumulated percentage of cells that have a Coulomb stress ≥ 10 kPa for each of the 22 filling scenarios is plotted in Figure 2c. The percentage of cells for each of the filling scenario maxes out at the same value (~30%) due to the fact that the maximum Coulomb stress at the end of the line plots is from the full impoundment (500 m to 640 m) regardless of the filling strategy. This implies that the depth-accumulated plot in Figure 2a would be the same for each of these 22 different filling scenarios.

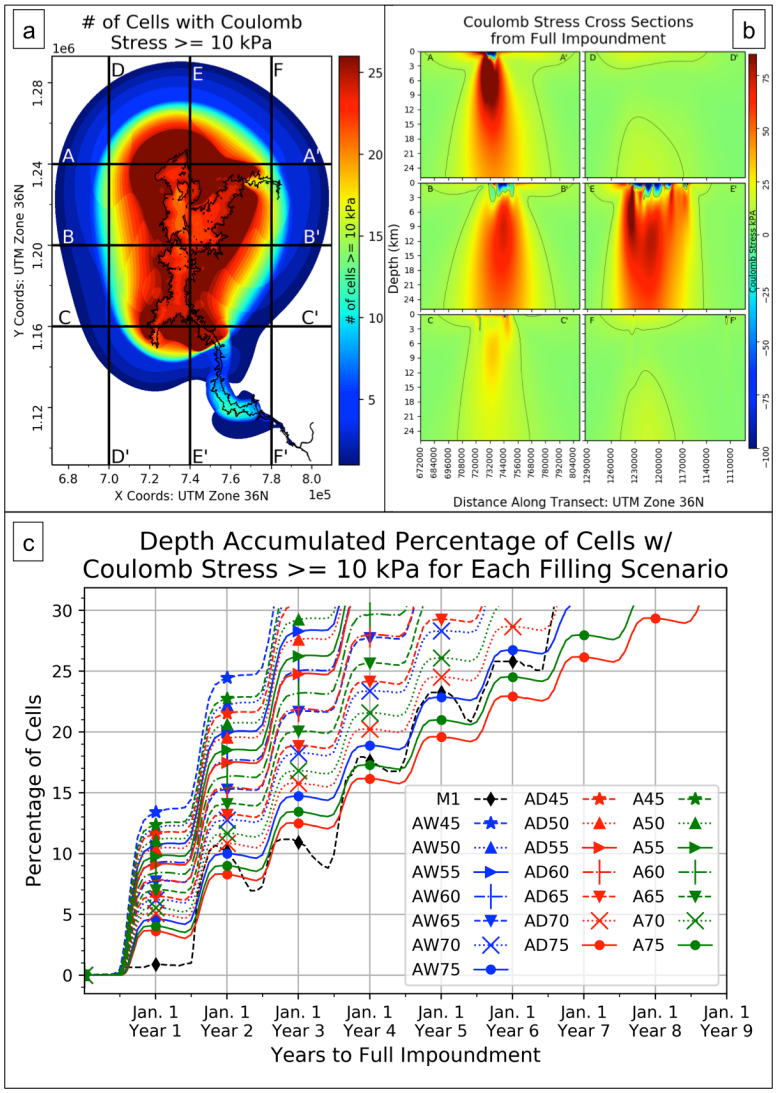

Figure 2. Depth-accumulated count of grid cells with Coulomb stresses ≥ 10 kPa (a), six example Coulomb stress cross sections (b), and daily depth-accumulated percentage of cells with a Coulomb stress ≥ 10 kPa for 22 different filling scenarios (c). Vertical and horizontal lines in (a) denote cross section locations in (b). Contour lines in (b) denote the location of the 10 kPa Coulomb stress regions. Cross sections are from west to east (e.g. A – A') and north to south (e.g. D – D'). The model depth is from the surface (0 km) down to 25 km. The areal extent of the reservoir for the full impoundment (500 m to 640 m) is plotted as the black polygon. Cell values at each depth in the model

with Coulomb stresses ≥ 10 kPa are summed and then divided by the total number of grid cells (c). This is done for each day in the filling strategy. Temporal variations in accumulated Coulomb stress as caused by the different impoundment scenarios are apparent

Lower percentages denote periods in the impoundment strategies where there is a reduced amount of modeled cells that are exposed to Coulomb stresses greater than the 10 kPa threshold. Although the magnitude of the overall depth-accumulated percentage of cells with a Coulomb stress ≥ 10 kPa is the same for each filling scenario (~30%), it is the timing of these accumulations that is markedly different. Here, we note that 13 of the 22 filling scenarios (*A45-60*, *AW45-65*, *AD45-60*) have nearly 50% of their total depth-accumulated cells ≥ 10 kPa within the first two years of the filling scenario. However, if the depth-accumulated percentage of cells is divided by the filling time for each scenario plotted in Figure 2c, we find that the five scenarios with the lowest count of daily cells that meet the 10 kPa stress threshold are *AD75* (0.0096), *A75* (0.0107), *AW75* (0.0121), *AD70* (0.0124), and *M1* (0.0125 %/day). Each of these five scenarios has a depth-accumulated cell-per-day total equating to an areal extent of 65.06, 72.79, 82.36, 84.54, and 85.06 km^2/day, respectively. In comparison, the bottom-five scenarios (*AW45*, *A45*, *AW50*, *AD45*, and *A50)* each have a depth-accumulated cell-per-day total equating to an areal extent of 210.73, 205.02, 201.98, 193.75, and 159.07 km^2/day, respectively. That said, these results show the five filling scenarios selected in order to reduce the daily depth-accumulated areal extent exposed to Coulomb stresses ≥ 10 kPa (based on optimally oriented faults) out of the 22 impoundment strategies

investigated. It is important to note that the highest and lowest rates are for the five longest and shortest filling scenarios as the total accumulated percentage of cells is the same for each of the filling scenarios. We reiterate that the overall Coulomb stress from the full impoundment applied on the surrounding lithosphere will not occur within one season, but will be spread out over the filling scenario decided upon by the water managers. That said, we have shown (in Figure 2c) 22 different potential filling scenarios at the GERD, and how their associated Coulomb stresses ≥ 10 kPa accumulate over their respective impoundment periods.

To further investigate the differences between the 22 different filling scenarios we derived the annual depth-accumulated distance change in the location of the maximum daily Coulomb stress. Simply put, the location of the maximum Coulomb stress for each of the 26 depths in our model was determined for each day of the 22 different impoundment strategies. The day-to-day change in the location of these max stresses was then determined at all depths. Lastly, the motion at each depth for each day was accumulated and these distances for every individual year in the filling scenario were summed. These depth-accumulated daily maximum Coulomb stress distances are plotted in Online Resource 1. These plots provide meaningful information as to the timing and motion changes of large Coulomb stresses brought on by the individual impoundment scenarios. They can act as a proxy for the comparison of the spatiotemporally varying stress changes imposed on the surrounding lithosphere from the individual filling scenarios. It is evident that the bulk of the maximum Coulomb stress motion occurs during the second-half of each year in the impoundment, and we attribute this to the marked seasonal hydrologic regime at the GERD site. We note that the filling

scenarios plotted in Online Resource 1 with lower end-of-the-year values denote impoundment strategies with a reduced amount of modeled area exposed to the maximum Coulomb stresses. In a sense, these lower accumulated distances can decrease the areal range where notable stresses are applied on potential seismogenic faults, and, in turn can also decrease the likelihood for these load-induced stresses to increase fault instability. The more these maximum Coulomb stresses migrate during the impoundment, the more areal extent is covered by these marked stress states and the more likely they are to interact with and push the optimally oriented faults to failure.

To better explore the differences between the 22 different impoundment strategies we sum the yearly distances for each filling scenario and plot the accumulation of these annual max Coulomb stress motions in Figure 3a. It is evident that the shorter impoundment scenarios (*A45*, *AD45*, and *AW45*) have the lowest accumulated max Coulomb stress motion. Again, if the max Coulomb stress motion is divided by the filling time for each scenario plotted in Figure 3a, we find that the five scenarios with the lowest daily motion of max Coulomb stress cells are *AD75* (0.14), *A75* (0.15), *AW75* (0.16), *AD70* (0.16), and *A70* (0.19 km/day). In contrast, the five scenarios with the highest daily motion of max Coulomb stress cells are *AD55* (0.42), *AW45* (0.39), *A55* (0.38), *A45* (0.38), and *AW50* (0.37 km/day). That said, these results show the five filling scenarios selected in order to reduce the depth-accumulated areal extent exposed to the maximum Coulomb stress (based on optimally oriented faults) out of the 22 impoundment strategies we investigated.

In a similar comparison, we derived the motion of the weighted hydrologic load centroid following the methodology outlined at the end of Section 2.1. The total

accumulated weighted load centroid motion for each impoundment scenario is plotted in Figure 3b. The total centroid motion was divided by the filling time for each scenario, and, similar to the results in the preceding paragraph, we find that the five scenarios with the lowest daily centroid motion are *AD75* (14), *A75* (15), *AW75* (17), *AD70* (17), and *A70* (19 m/day). In comparison, the five scenarios with the highest daily centroid motion are *AW45* (39), *A45* (39), *AW50* (38), *AD45* (37), and *AD55* (36 m/day). We note that the scenarios with the lowest hydrologic load centroid rates are similar to their max Coulomb stress motion rate counterparts as mentioned in the previous paragraph. Further, the examination of Figure 3 highlights the similar pattern between the motion rates of the load centroids and max Coulomb stresses. As such, it would appear that weighted hydrologic load centroid motion is a good proxy for maximum Coulomb stress cell motion on optimally oriented fault planes, and vice versa.

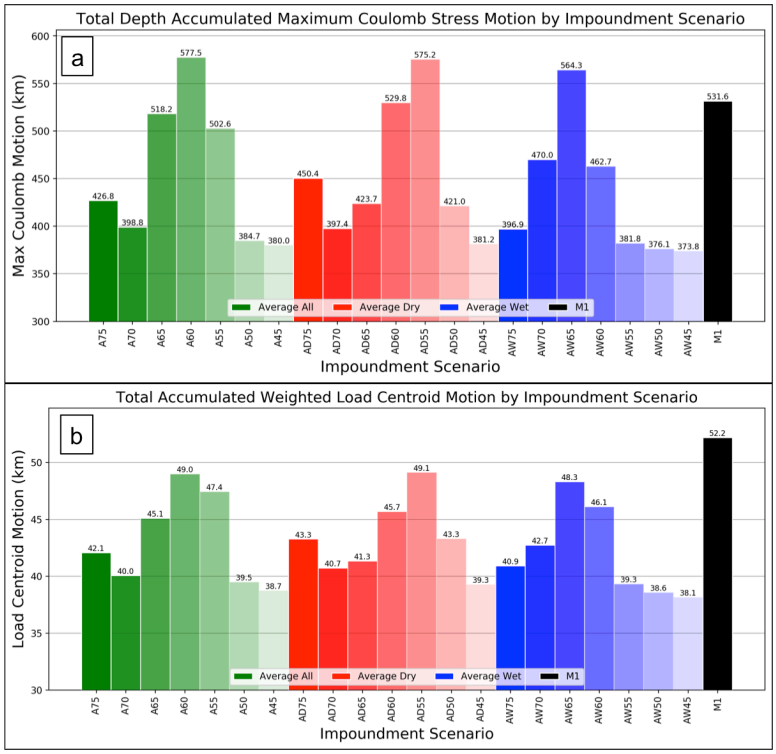

Figure 3. Total depth-accumulated movement of the maximum Coulomb stress cell (a) and total accumulated motion of the weighted hydrologic load centroid (b) for 22 different filling scenarios. (a) is the summation of the depth-accumulated motion of the maximum Coulomb stress as calculated on an array of optimally oriented faults and (b) is the accumulated motion of the weighted load centroid. Here, lower numbers denote filling scenarios where there is a reduced amount of sub-surface area exposed to the maximum Coulomb stresses (a) and where there is a reduced motion in the location of the weighted load centroid (b)

Upon comparison of the above stress vector and hydrologic load centroids for each of the 22 different impoundment scenarios we note that the more meaningful results are with the depth-accumulated maximum Coulomb motion and the load centroid movements. This is because the results from the percent Coulomb stress analysis have a constant value with which to derive their rates (i.e. The rate calculations are based on the same value due to the fact that the total percentage of Coulomb stress cells ≥ 10 kPa is the same for each impoundment scenario). That said, the five filling strategies that provide for the lowest maximum Coulomb stress motion and the lowest weighted hydrologic load centroid motion per impoundment are *AD75*, *A75*, *AW75*, *AD70*, and *A70*. We note that these five impoundment strategies are the longest-running, non-*M1* strategies of the 22 investigated. Impoundment scenario *M1* is not included (even though its filling time is longer than *A70*'s) as its accumulated maximum Coulomb stress and load centroid distance per unit time is notably higher than the abovementioned scenarios (as evidenced in Figure 3a and 3b). This stems from the different input

hydrologic variables utilized to derive the load input arrays (daily water level, volume, and areal extent changes). Upon inspection of Figure S7 from [10] it becomes evident that during the *M1* filling scenario there exists a seasonal period of non-negligible negative storage in all but the first year of the impoundment scenario. In some cases this seasonal negative storage value equates to ~5 Gt (i.e. during year 2 – 3 of the *M1* scenario). This is in direct comparison to all of the other impoundment scenarios (Figures S3 – S6 from [10]) where there are notably fewer seasons in the filling scenarios where negative water storage occurs. Further, when negative storage values do happen, they are far lower than the values that occur in the *M1* filling scenario. This is the reason that we see larger values in the motion of the depth-accumulated maximum Coulomb stress location as well as the weighted hydrologic load centroid per unit time for the *M1* scenario as compared to the *AD75*, *A75*, *AW75*, *AD70*, and *A70* impoundment scenarios. This implies that an increase in total accumulated daily reservoir storage change (both positive and negative) will cause an increase in the motion of both the depth-accumulated maximum Coulomb stress location as well as the weighted hydrologic load centroid. This makes intuitive sense seeing as how the increased change in the reservoir's hydrologic load will alter the location of the load's centroid as well as the maximum Coulomb stress.

3.2 Seasonal Operations

The notable differences between the operational scenarios investigated show how large the effect dam operations can have on the amplitudes of seasonal hydrologic load fluctuations [10]. In turn, these markedly different fluxes will determine the

magnitude and spatiotemporal changes of the load-induced Coulomb stresses in the region during any given operational year. The seasonal stress model runs were started on the first date in which there is positive reservoir storage (*L1 – L3, L5*: July 1 and *L4*: June 1) and use a 622 m reservoir level as the initial model input. The 622 m water level was selected as Mulat and Moges [61] specify the minimum operating level of the GERD as such. However, other studies state the minimum operating level is at 590 m [62, 63]. That said, our stress models were run with both 622 and 590 m as the starting point. We note that the total volumetric change is the same in both runs and that the amplitudes of the seasonal water level and areal extent changes are larger with the 590 m elevation starting point. The maximum subsurficial Coulomb stresses derived on optimally oriented fault planes for both the 590 and 622 m mean annual operational scenarios (*L1 – L5*) as calculated from the methods and datasets described in Section 2.2 are 44.7, 44.9, 44.3, 39.1, 34.7 kPa and 26.0, 26.2, 25.8, 22.2, 19.4 kPa, respectively. The surficial Coulomb stresses were excluded to determine this maximum value and this maximum stress occurs at a depth of 1 km for each scenario. The maximum Coulomb stresses for operational scenarios *L1 – L5* with a 590 m starting water level range from 87 to 20 kPa (*L1 – L3*), 78 to 17 kPa (*L4*), and 69 to 15 kPa (*L5*) from the surface (0 km) down to the base of the model (25 km), respectively. In contrast, the maximum Coulomb stresses for operational scenarios *L1 – L5* with a 622 m starting water level range from 53 to 16 kPa (*L1 – L3*), 45 to 14 kPa (*L4*), and 41 to 12 kPa (*L5*) from the surface (0 km) down to the base of the model (25 km), respectively. The maximum Coulomb stresses for each of the five mean annual scenarios are around 18.7 (*L1* & *L2*), 18.5 (*L3*), 16.9 (*L4*), and 15.3 kPa (*L5*) larger in

the 590 m data runs as compared to the maximum stresses derived from the 622 m starting point. We attribute this difference to the increased load per unit area for the 590 m data runs. The reservoir volumes for both starting points are the same, but the maximum areal extents for the 590 m runs are smaller than their 622 m counterparts, thereby increasing the hydrologic load per unit area.

In order to show the spatial extent of non-negligible stresses from each operational scenario (and both starting water levels) we calculated the number of cells at each depth that have a Coulomb stress value ≥ 10 kPa. These depth-accumulated values are plotted in Figure 4a along with an example cross section of the Coulomb stress fields (Figure 4b) for operational scenarios *L1 – L5*. The Coulomb, normal, and shear stress arrays from each of these operating strategies at the 590 m and 622 m starting water levels for each depth (0 km to 25 m) in our model are provided in Movie S2 – S11. Again, we note that Coulomb stress increases in excess of 10 kPa are considered to be the threshold at which seismicity is affected [53, 60]. The darkest red regions in Figure 4a show the areas immediately adjacent to the main body of the average seasonal impoundment that incurs Coulomb stresses ≥ 10 kPa at all depths in our model (0 km to 25 km). Example cross sections (A – A') through the heart of the reservoir for each of the mean annual operational scenarios and water level starts are provided in Figure 4b. These provide detailed views along the depth axis which allows for a comparison of subsurficial Coulomb stresses for each of the ten different mean annual operations. It is evident from the range of maximum Coulomb stresses per depth (see previous paragraph), the number of cells with Coulomb stresses ≥ 10 kPa (Figure 4a), and the Coulomb cross sections (Figure 4b) that the scenarios with a 590 m water

level start have larger subsurfical stress regimes as compared to their 622 m water level start counterparts. Again, we reiterate that these are Coulomb stress arrays on idealized fault planes within our model regime.

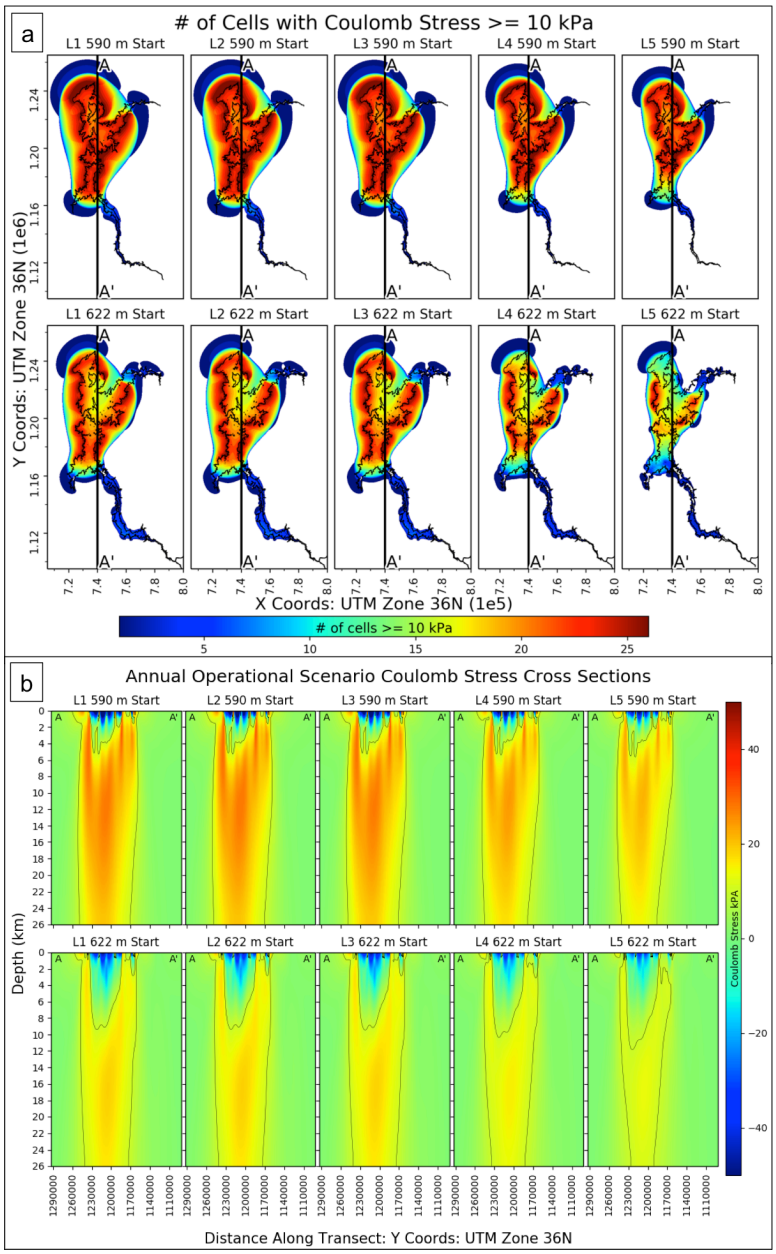

Figure 4. Depth-accumulated count of grid cells with Coulomb stresses ≥ 10 kPa (a) and Coulomb stress cross sections through the heart of the impoundment (b) for both

starting water levels (590 m: top & 622 m: bottom) and each mean annual operational scenario (*L1 – L5*). The vertical lines in (a) denote the cross section locations for the plots in (b). The areal extent of the reservoir for the individual mean annual scenarios' maximum water level is plotted as the black polygon in each subplot within (a). Contour lines in (b) denote the location of the 10 kPa Coulomb stress regions. Cross sections are from the north to south (e.g. A – A') and their locations are plotted in (a). The model depth is from the surface (0 km) down to 25 km

The depth-accumulated percentage of cells that have a Coulomb stress ≥ 10 kPa was determined in order to appropriately investigate and compare the stress state changes for the two different mean annual operational scenarios (590 & 622 m start). These percentages include the Coulomb stresses at the surface of the model (0 km) and we note that the stress arrays are calculated from hydrologic loads based on the starting water level and the seasonal peak water level for each of the ten individual mean annual operational strategies. The total depth-accumulated percentage of cells that have a Coulomb stress ≥ 10 kPa for the 590 m and the 622 m starting water levels for each operational scenario are 10.8, 10.9, 10.6, 8.8, 7.2% and 9.1, 9.2, 9.0, 6.6, 4.5%, respectively. Lower percentages denote strategies where there is a reduced amount of area exposed to Coulomb stresses greater than the 10 kPa threshold. The scenarios for the 590 m starting water level have around 1.6 – 2.7% more depth-accumulated cells than their 622 m starting water level counterparts. This implies that all five mean annual operational scenarios (*L1 – L5*) with a 590 m starting water level have an increased amount of optimally oriented fault cells with a Coulomb stress of at least

10 kPa as compared to the 622 m starting water level. We note that the total hydrologic load applied for each corresponding scenario at both water level start dates is the same, but the areal extent at the peak load between the two starting elevations is notably different. The difference in the overall areal extent at which the load is distributed is mostly dependent on the starting water level of the scenario. We recall from the end of the second paragraph in this section that there is an increased load per unit area for the 590 m data runs as the maximum areal extents for the 590 m starts are smaller than their 622 m counterparts, thereby increasing the hydrologic load per unit area. The load per unit areal coverage for each of the five operational strategies for the 590 m starting water level is 20.55, 20.57, 20.38 18.97, and 17.17 ton/m^2 as compared to 13.43 13.46, 13.29, 11.95, and 10.54 ton/m^2 for the 622 m starting water level. We attribute this as the cause for the increased amount of Coulomb stress for the scenarios with a 590 m starting water level.

The weighted hydrologic load motion was calculated following the methodology outlined at the end of Section 2.1, and the annual accumulated weighted load centroid motion for the 590 and the 622 m starting water levels for each operational scenario are 14.96, 14.99, 14.81, 13.32, 11.72 km and 8.03, 8.05, 7.94, 6.98, 6.09 km, respectively. The motion of the hydrologic load centroids for each scenario is similar to their depth-accumulated Coulomb stress percentage counterparts listed in the previous paragraph. We attribute the larger load centroid motion of the 590 m data runs to the increased range of annual water level and areal extent changes as compared to the 622 m water level start. The seasonal amplitudes of water level and areal extent change for both the 590 and 622 m starting water levels for the five mean annual operational scenarios (*L1*

– *L5*) are 27.3 (570.6), 27.4 (573.4), 27.1 (564.1), 23.9 (484.3), 21.2 m (421.4 km^2) and 15.6 (475.3), 15.7 (477.8), 15.5 (469.5), 13.4 (399.0), 11.7 m (344.9 km^2), respectively. These differences allow for the increased load centroid motion for the 590 m water level start scenarios.

The results from the previous few paragraphs highlight the importance of the initial and peak water levels for the mean annual operational scenarios. The Coulomb stresses from a more condensed seasonal reservoir load will be larger than the Coulomb stress as calculated from the same hydrologic load with less load per unit area. In contrast, for a given seasonal hydrologic load, a decrease in the load per unit area would reduce the overall Coulomb stresses on the optimal fault planes. We note that these are comparisons between five different mean annual scenarios, and we focus on the full 39-year operational dataset in subsequent paragraphs. These long-term scenarios are investigated in order to better understand the dissimilarities in Coulomb stress between differing seasonal amplitudes of load changes and initial water levels.

The maximum (and minimum) subsurficial Coulomb stresses for each of the largest seasonal amplitudes of hydrologic change from the full 39-year dataset for the five operational scenarios (*L1* – *L5*) are 67.51 (10.58), 60.76 (10.77), 54.80 (11.55), 75.91 (7.32), and 44.16 kPa (6.44 kPa), respectively. The seasonal maximum and minimum subsurficial Coulomb stress for all five scenarios over all 39 years of hydrologic data are 75.91 and 6.44 kPa, respectively. For context, the maximum subsurficial Coulomb stresses from the highest amplitude season in the full 39-year operational dataset for all five of the scenarios are 36.30, 32.67, 29.46, 40.81, and 23.74% of the total maximum subsurficial Coulomb stresses brought on by the entire

GERD impoundment. These notable ranges in Coulomb stresses further highlight the stark differences in the annual stresses applied on the lithosphere from the varying hydrologic loading and unloading operational scenarios of the reservoir. The starting water level for each of these full operational runs was set such that the maximum water level over the entire 39-year dataset never exceeded the maximum GERD water level of 640 m. Here, the beginning of an annual seasonal cycle is defined as the first day in which there is positive water storage and the end to that cycle occurs when the water storage flips from negative to positive (i.e. A full seasonal inflow and outflow curve). In some cases, this means that seasonal cycles are not exactly 365 days long.

The depth-accumulated percentage of cells that have a Coulomb stress ≥ 10 kPa was determined in order to appropriately investigate and compare the seasonal stress state changes for the full 39-year operational scenarios (*L1 – L5*). These percentages include the Coulomb stresses at the surface of the model (0 km) and the stress arrays are calculated from hydrologic loads based on the starting water level and the seasonal peak water level for each year in the full operational dataset. The season total depth-accumulated percentage of cells that have a Coulomb stress ≥ 10 kPa for each of the operational scenarios are plotted in Figure 5. Lower percentages denote strategies where there is a reduced amount of modeled area exposed to Coulomb stresses greater than the 10 kPa threshold for that particular season. There are marked differences in the percentages of Coulomb stress cells between the five different scenarios in any given season and between each individual annual operation within the full dataset. We attribute these variations to the hydrologic load per unit area of the seasonal reservoir loads for each of the annual operations. We point the reader to

Online Resource 2 that highlights the relationship between the seasonal load per unit area and the number of depth-accumulated Coulomb stress cells ≥ 10 kPa. This scatter plot shows that as the load per unit density increases so to does the amount of stress cells ≥ 10 kPa. This implies that a reduction in the seasonal hydrologic load per unit area will likely reduce the number of cells with notable Coulomb stresses. Further, due to the topography of the study area, we note that there is an overall decrease in the hydrologic load per unit area as the water level at the beginning of the operational season increases. This relationship is highlighted in Online Resource 3. It can be inferred that, typically, the higher the reservoir level is at the start of a given operational season the fewer cells will incur Coulomb stresses ≥ 10 kPa.

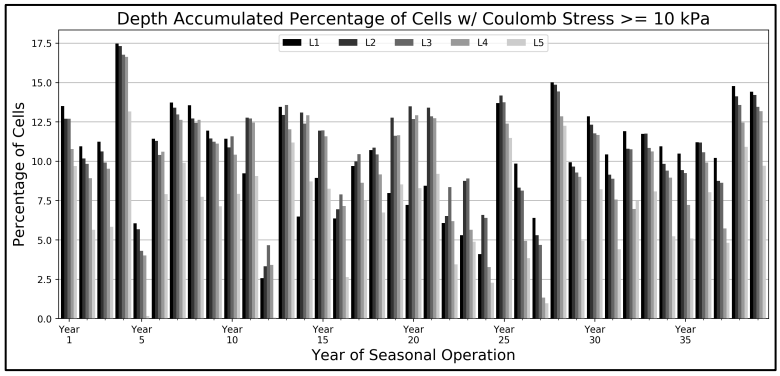

Figure 5. Depth-accumulated percentage of cells with a Coulomb stress ≥ 10 kPa for five different operational scenarios for the entire 39-year operational dataset. The Coulomb stress on optimally oriented fault planes was calculated from hydrologic loads based on the starting water level and the seasonal peak water level for each individual year

To better compare the differences between the five operational scenarios we determined the overall total percentage of Coulomb stress cells ≥ 10 kPa from the full

39-year dataset for the five operational scenarios. These percentages are plotted in Online Resource 4. Operational strategies *L1*, *L2*, and *L3* have the highest accumulated amount of cells followed by *L4* and then *L5*. These results follow a similar trend as previously discussed comparisons between strategies and are attributed to the overall differences in annual reservoir storage between the operational scenarios (Figure S8 from [10]).

The seasonal-accumulated daily weighted load centroid motion for the five operational scenarios for each of the 39 years in the GERD operational dataset is plotted in Online Resource 5. The motion of the load centroid can be thought of as a proxy for the changes in the location of where the maximum stresses are applied on the Earth's crust. Similar to the results in Figure 5, there are notable annual differences in the motion of the hydrologic load centroid for each scenario. Again, we attribute these marked variances to the different seasonal load per unit areas and the water levels at the start of each season. The relationship between the accumulated annual centroid motion and the reservoir water level at the beginning of the season is highlighted in Online Resource 6. It can be inferred that, typically, the higher the reservoir level is at the start of a given operational season, the less the weighted load centroid travels during that time period.

The comparisons of the stress vector and hydrologic load centroids for each annual operational scenario have shown that the water level at the beginning of the season as well as the seasonal reservoir load per unit area play a major role in the amount of stress applied on the surrounding lithosphere. We reiterate that the above discussion is based on the Coulomb stresses on optimally oriented fault planes and that

we were unable to locate regional seismogenic fault models in the area of the GERD impoundment. That said, this investigation has laid the groundwork for future studies to examine Coulomb stress on known seismogenic faults and to explore the stress vector responses on different impoundment and operational scenarios in order to reduce the likelihood of triggered seismic events during reservoir filling and operational scenarios.

4 Conclusion

The Coulomb stresses on optimal fault planes for the full GERD impoundment were calculated, and the maximum stresses ranged from ~1100 at the surface to ~57 kPa at a depth of 25 km. The maximum subsurficial Coulomb stress from the full load was found to be ~186 kPa. The daily (and total) depth-accumulated percentage of cells that have a Coulomb stress value ≥ 10 kPa for 22 impoundment strategies were determined and ~30% of the cells in our model had Coulomb stresses larger than this threshold. The depth-accumulated motion of the maximum Coulomb stress locations was calculated along with the motion of the weighted hydrologic load centroid for each impoundment scenario. The five filling scenarios selected in order to reduce the daily depth-accumulated extent exposed to Coulomb stresses ≥ 10 kPa (based on optimally oriented faults) out of the 22 impoundment strategies are *AD75*, *A75*, *AW75*, *AD70*, and *M1*. The five filling strategies that provide for the lowest maximum Coulomb stress motion and the lowest weighted hydrologic load centroid motion per day of impoundment are *AD75*, *A75*, *AW75*, *AD70*, and *A70*. The main driver behind the stress and load centroid motion is the annual, accumulated daily reservoir storage change (both positive and negative) where an increased volume change caused an increase in

the motion of both the depth-accumulated maximum Coulomb stress location as well as the weighted hydrologic load centroid.

Coulomb stresses for five mean annual operational cycles with two different starting water levels (590 and 622 m) were calculated and the maximum subsurficial Coulomb stresses for each 590 m water level start scenario were around 18.7 (*L1* & *L2*), 18.5 (*L3*), 16.9 (*L4*), and 15.3 kPa (*L5*) larger than their 622 m counterparts. The depth-accumulated percentage of cells that have a Coulomb stress value ≥ 10 kPa for these annual scenarios was determined and the 590 m water level start scenarios had larger stress regimes as compared to their 622 m water level start counterparts. These differences were attributed to the increased load per unit area for the 590 m data runs. The Coulomb stress from a more condensed seasonal reservoir load will be larger than the Coulomb stress as calculated from the same hydrologic load with less load per unit area. The motion of the weighted hydrologic load centroid for each operational scenario was calculated and an increased load centroid motion for the 590 m water level start scenarios was found. This was attributed to the increased range of annual water level and areal extent changes as compared to the 622 m water level starts.

Annual Coulomb stresses were calculated for five different operational scenarios each consisting of 39 different yearly operational seasons. The maximum Coulomb stresses from the highest amplitude season for each scenario consisted of 36.3, 32.7, 29.5, 40.8, and 23.7% of the total maximum Coulomb stresses brought on by the entire GERD impoundment. The depth-accumulated percentage of cells that have a Coulomb stress value ≥ 10 kPa and the motion of the weighted hydrologic load centroid for the 39-year operational scenarios were determined and marked differences between the

five different scenarios were found. These variations were attributed to the hydrologic load per unit area of the seasonal reservoir loads for each of the annual operations, and, in part to the initial seasonal water level. In other words, a reduction in the seasonal hydrologic load per unit area or an increased initial seasonal water level would likely reduce both the number of cells with notable Coulomb stresses and the accumulated annual centroid motion. Operational strategies *L1*, *L2*, and *L3* had the highest accumulated amount of notable Coulomb stress cells followed by *L4* and then *L5*. These differences were attributed to variations in overall annual reservoir storage between the actual operational scenarios.

Acknowledgments

We thank Stefan Liersch for kindly supplying his monthly hydrologic data. We thank Richard Styron for hosting his scripts on github. Part of this work was funded by NASA's Surface Water and Ocean Topography (SWOT) Program under Grant NNX16AH85G. This work used computational and storage services associated with the Hoffman2 Shared Cluster provided by UCLA Institute for Digital Research and Education's Research Technology Group. We thank Frank Madson for his help with figure creation.

Appendix I

Principles of Coulomb Stress Model

Coulomb stresses on optimal planes were calculated for each full-resolution cell (~30 m x ~30 m) in the array at 1 km depth increments from the surface (0 km) down to 25 km. We followed the method outlined in [54] to derive the stress fields as caused by the hydrologic loads from the GERD impoundment and operational scenarios. All calculations were undertaken in an elastic half-space with a model domain of 300 km x 300 km x 25 km and at the full cell resolution. For the subsequent calculations, both the first and second Lame's parameters were set to 1, which assumes a Poisson ratio of 0.25. The final six stress tensor fields from the hydrologic loads were derived from their vertical (Boussinesq [55]) and horizontal (Cerruti [56]) stress components, per [54]. The stress tensors $M(x,y,z)$ are derived by

$$M(x,y,z) = M^B(x,y,z) + M^C(x,y,x) \ ,$$

where $M^B(x, y, z)$ is the portion of the stress field as caused by the vertical loading of the hydrologic load and $M^C(x, y, z)$ is the portion of the stress field as caused by the horizontal forces of the vertical hydrologic loading. Here, $M^B(x, y, z)$ is derived by

$$M^B(x,y,z) = G^B(x,y,z) * F_v(x,y) \ ,$$

where $G^B(x, y, z)$ are the Boussinesq solutions for stresses as caused by the vertical hydrologic load on the model's surface and $F_v(x, y)$ is the vertical loading function for the six stress tensor components from the hydrologic loads. $M^C(x, y, z)$ is derived by

$$M^C(x, y, z) = G_x^C(x, y, z) * F_{h,x}(x, y) + G_y^C(x, y, z) * F_{h,y}(x, y) \ ,$$

where $G_i^C(x, y, z)$ are the Cerruti solutions for stresses as caused by the horizontal forces in the *i* direction from the vertical point source hydrologic load in the *i* direction on the model's surface. The loading Cerruti solutions are convolved by their respective *x* and *y* loading functions.

Altered scripts from [57] were utilized to calculate both of the horizontal and vertical components. The vertical stress component was derived by convolving the Boussinesq solutions as Green's functions with the full hydrologic load array [54]. We utilized a water density of 1000 kg/m^3 and a gravitational constant of 9.81 m/s^2 and took advantage of the superposition theorem to do the convolutions in the Fourier domain in order to speed up the calculations. The horizontal component consists of the two sets of stress fields from both the *x* and *y* horizontal surface tractions brought on by the vertical point load arrays on the half-space surface as calculated above. The two horizontal stress components were calculated by convolving the Cerruti solutions as Green's functions with their respective *x* or *y* loading function as derived from the appropriate surface traction for the full hydrologic load array [54]. Similar to the above vertical component, we utilized a water density of 1000 kg/m^3 and a gravitational force of 9.81 m/s^2 and took advantage of the superposition theorem to do the *x* and *y* horizontal

convolutions in the Fourier domain. Lastly, the stress fields from the vertical loading component and the two *x* and *y* horizontal components were summed in order to derive the final stress tensor field for each water level in the GERD impoundment and operational scenarios.

Those stress tensors were utilized to derive the shear and normal stresses on optimally oriented planes for each cell in the model. These shear and normal stresses were used to calculate the effective Coulomb stress changes following the equations in [52]. Failure occurs on these planes as soon as the Coulomb stress (σ_f) surpasses some value. Here, Coulomb stresses are derived by

$$\sigma_f = \tau_\beta - \mu(\sigma_\beta - p) \ ,$$

where τ_β is the shear stress, σ_β is the normal stress, p is the fluid pore pressure, and μ is the coefficient of friction. A friction coefficient of 0.6 was used throughout and pore pressure was ignored (set to zero) in the calculations. Pore pressure was neglected in order to solely focus on the static stress effects from the changing hydrologic load, and not the reduction in the optimal fault planes' stability from the increased pore pressure and the subsequent reduction in frictional stresses caused by the diffusion of water into the underlying rock. We note that the friction coefficient utilized within our calculations (0.6) is somewhat conservative and allows for increased estimates of stability, and that a reduction in this parameter would have a destabilizing effect on our calculations of Coulomb stress. Further, the absence of the pore pressure parameter underestimates the results from our final Coulomb stress computations and that its inclusion into the

calculation would further increase the overall instability (increased Coulomb stress values) of the optimal planes.

Supplementary Material

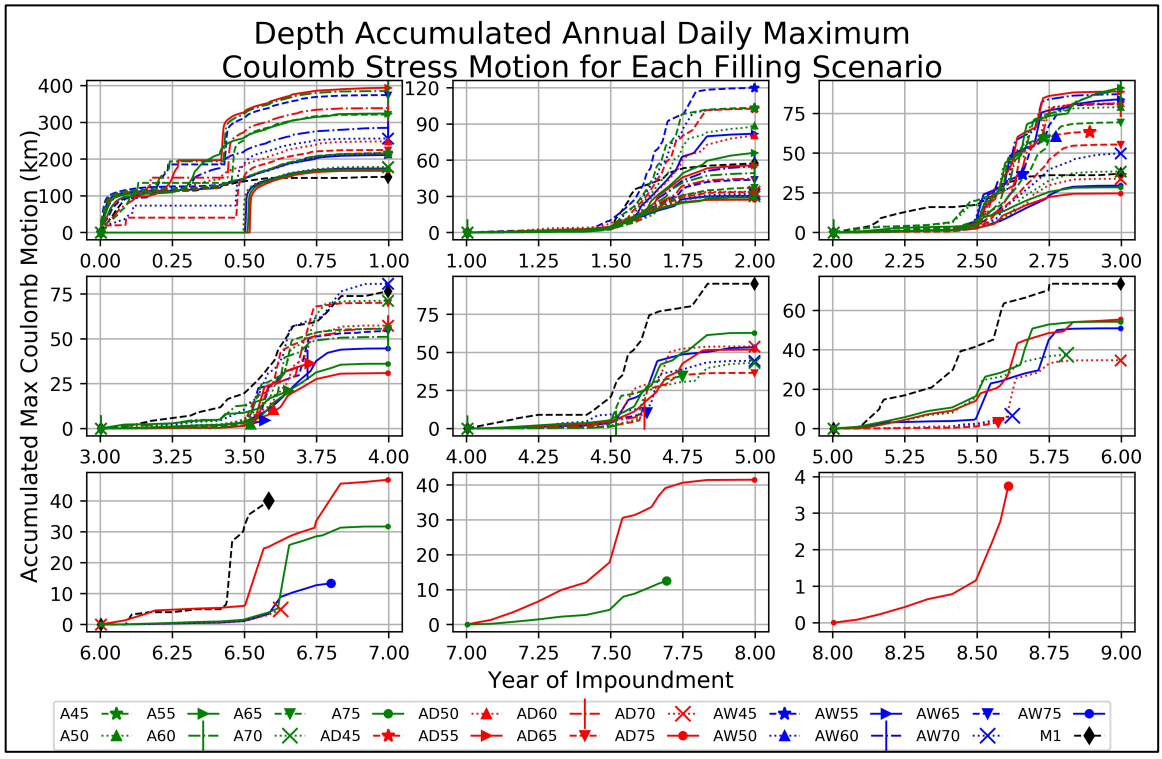

Figure S1. Daily depth-accumulated movement of the maximum Coulomb stress cell for 22 different filling scenarios. Markers on each of the impoundment scenarios denote the end of the annual period as well as the end of that particular filling scenario. We note that each subplot within the figure is a year's worth of accumulated maximum Coulomb stress distance changes and has its own y-axis limit/scale.

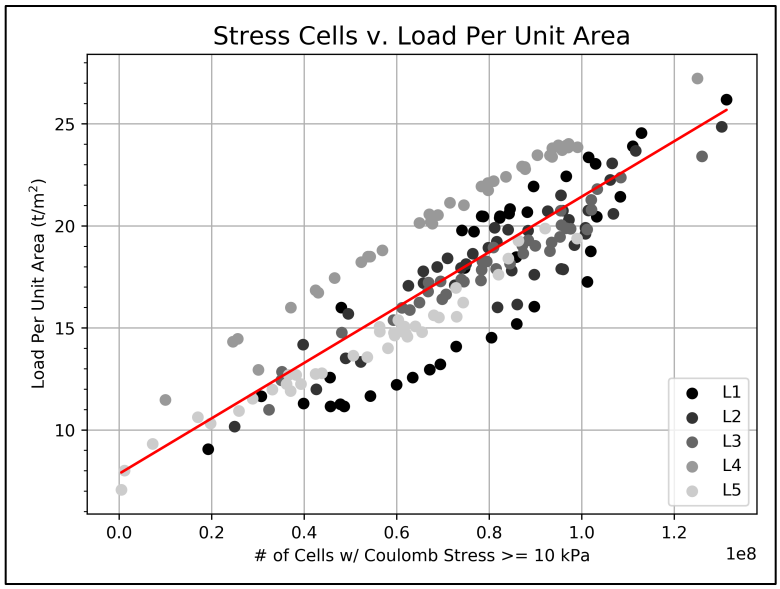

Figure S2. Depth-accumulated number of cells with a Coulomb stress ≥ 10 kPa against seasonal hydrologic load per unit area for all operational scenarios for each year in the full 39-year operational dataset.

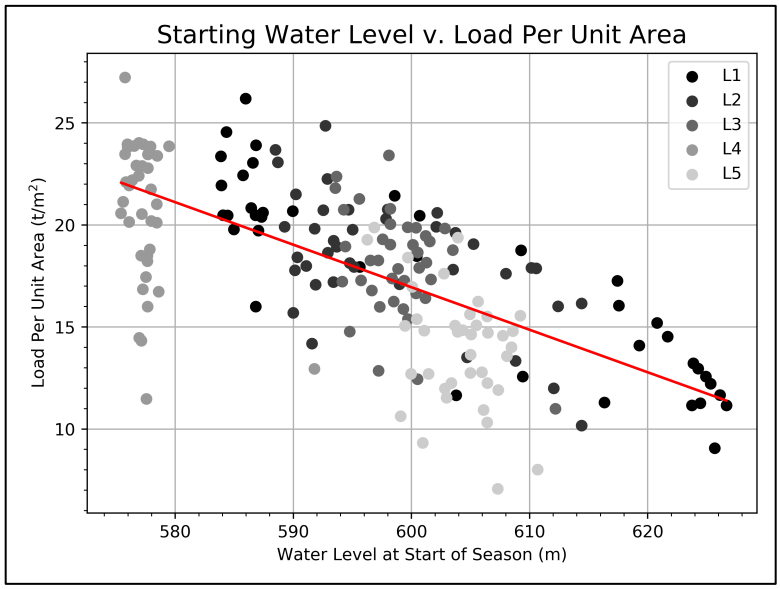

Figure S3. Water level at seasonal start against seasonal hydrologic load per unit area for all operational scenarios for each year in the full 39-year operational dataset.

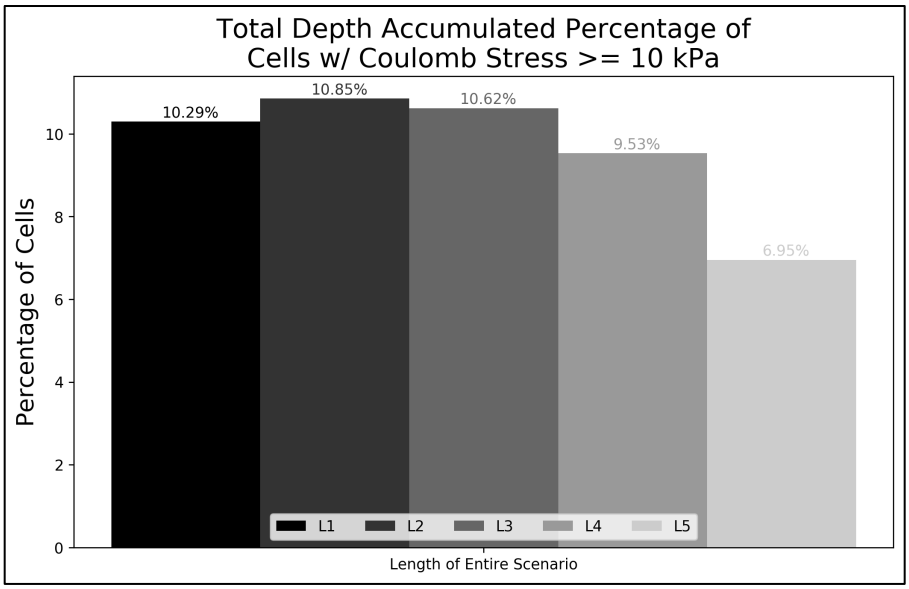

Figure S4. Total depth-accumulated percentage of cells with a Coulomb stress ≥ 10 kPa for five operational scenarios from the full 39-year operational dataset. The Coulomb stress on optimally oriented fault planes was calculated from hydrologic loads based on the starting water level and the seasonal peak water level for each of the 39 years.

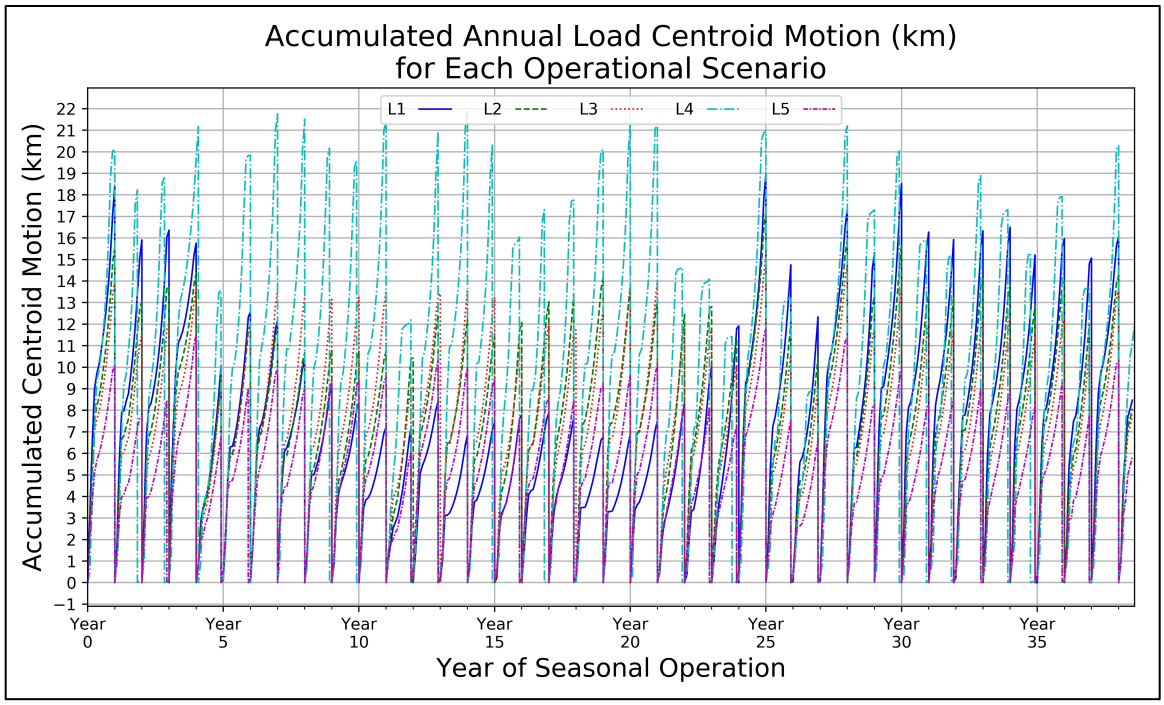

Figure S5. Seasonal accumulated daily motion of the weighted hydrologic load centroid for the five operational strategies for each year in the full 39-year datasets. These plots track the daily motion of the weighted load centroid for each scenario. The plotted data is the accumulated motion for each seasonal cycle in the full 39-year dataset. Note that the motion at the beginning of each season reverts back to zero, and the subsequent seasonal motion is accumulated from that starting point until the end of the season.

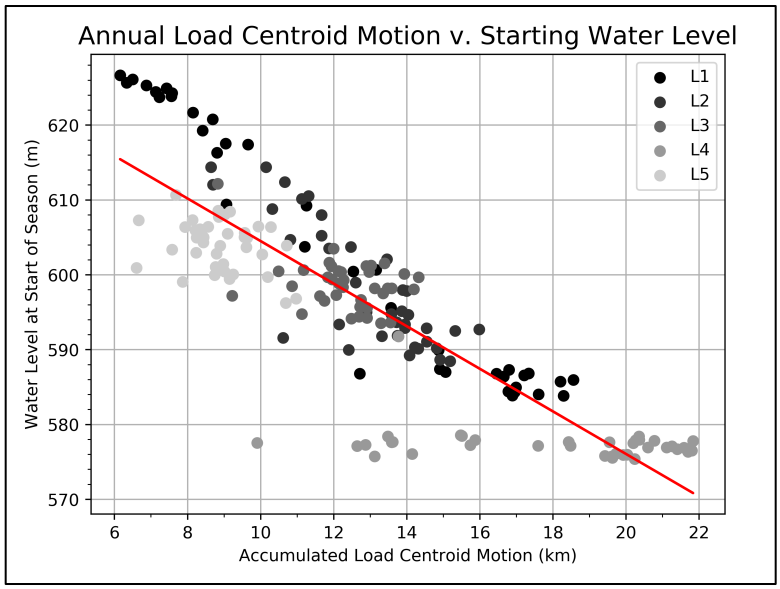

Figure S6. Accumulated annual load centroid motion against water level at seasonal start for all operational scenarios for each year in the full 39-year operational dataset.

Movie S1. Animation displaying the Coulomb, normal, and shear stress arrays from the full GERD impoundment for each depth (0 km to 25 m) in our model. The location of the maximum Coulomb stress for each depth is plotted as a white cross and the contour lines denote the location of the 10 kPa Coulomb stress regions.

Movie S2. Animation displaying the Coulomb, normal, and shear stress arrays from operational scenario *L1* for the 590 m starting water level at each depth (0 km to 25 m) in our model. The location of the maximum Coulomb stress for each depth is plotted as a white cross and the contour lines denote the location of the 10 kPa Coulomb stress regions.

Movie S3. Animation displaying the Coulomb, normal, and shear stress arrays from operational scenario *L2* for the 590 m starting water level at each depth (0 km to 25 m) in our model. The location of the maximum Coulomb stress for each depth is plotted as

a white cross and the contour lines denote the location of the 10 kPa Coulomb stress regions.

Movie S4. Animation displaying the Coulomb, normal, and shear stress arrays from operational scenario *L3* for the 590 m starting water level at each depth (0 km to 25 m) in our model. The location of the maximum Coulomb stress for each depth is plotted as a white cross and the contour lines denote the location of the 10 kPa Coulomb stress regions.

Movie S5. Animation displaying the Coulomb, normal, and shear stress arrays from operational scenario *L4* for the 590 m starting water level at each depth (0 km to 25 m) in our model. The location of the maximum Coulomb stress for each depth is plotted as a white cross and the contour lines denote the location of the 10 kPa Coulomb stress regions.

Movie S6. Animation displaying the Coulomb, normal, and shear stress arrays from operational scenario *L5* for the 590 m starting water level at each depth (0 km to 25 m) in our model. The location of the maximum Coulomb stress for each depth is plotted as a white cross and the contour lines denote the location of the 10 kPa Coulomb stress regions.

Movie S7. Animation displaying the Coulomb, normal, and shear stress arrays from operational scenario *L1* for the 622 m starting water level at each depth (0 km to 25 m) in our model. The location of the maximum Coulomb stress for each depth is plotted as a white cross and the contour lines denote the location of the 10 kPa Coulomb stress regions.

Movie S8. Animation displaying the Coulomb, normal, and shear stress arrays from operational scenario *L2* for the 622 m starting water level at each depth (0 km to 25 m) in our model. The location of the maximum Coulomb stress for each depth is plotted as a white cross and the contour lines denote the location of the 10 kPa Coulomb stress regions.

Movie S9. Animation displaying the Coulomb, normal, and shear stress arrays from operational scenario *L3* for the 622 m starting water level at each depth (0 km to 25 m) in our model. The location of the maximum Coulomb stress for each depth is plotted as a white cross and the contour lines denote the location of the 10 kPa Coulomb stress regions.

Movie S10. Animation displaying the Coulomb, normal, and shear stress arrays from operational scenario *L4* for the 622 m starting water level at each depth (0 km to 25 m) in our model. The location of the maximum Coulomb stress for each depth is plotted as a white cross and the contour lines denote the location of the 10 kPa Coulomb stress regions.

Movie S11. Animation displaying the Coulomb, normal, and shear stress arrays from operational scenario *L5* for the 622 m starting water level at each depth (0 km to 25 m) in our model. The location of the maximum Coulomb stress for each depth is plotted as a white cross and the contour lines denote the location of the 10 kPa Coulomb stress regions.

References

1. Zhang, Y., S.T. Erkyihum, and P. Block, *Filling the GERD: evaluating hydroclimatic variability and impoundment strategies for Blue Nile riparian countries.* Water international, 2016. **41**(4): p. 593-610.
2. Abtew, W. and S.B. Dessu, *The Grand Ethiopian Renaissance Dam on the Blue Nile*. 2018, Springer.
3. Reclamation, U.S.B.o., *Land and Water Resources of the Blue Nile Basin, Ethiopia*. 1964: The Bureau.
4. Ahmed, A.T. and M.H. Elsanabary, *ENVIRONMENTAL AND HYDROLOGICAL IMPACTS OF GRAND ETHIOPIAN RENAISSANCE DAM ON THE NILE RIVER.*
5. Mulat, A.G., S.A. Moges, and M.A. Moges, *Evaluation of multi-storage hydropower development in the upper Blue Nile River (Ethiopia): regional perspective.* Journal of Hydrology: Regional Studies, 2018. **16**: p. 1-14.
6. Sharaky, A.M., K.H. Hamed, and A.B. Mohamed, *Model-Based Optimization for Operating the Ethiopian Renaissance Dam on the Blue Nile River.* 2017.
7. Liersch, S., H. Koch, and F.F. Hattermann, *Management Scenarios of the Grand Ethiopian Renaissance Dam and Their Impacts under Recent and Future Climates.* Water, 2017. **9**(10): p. 728.
8. Melesse, A.M., W. Abtew, and S.G. Setegn, *Nile River basin: ecohydrological challenges, climate change and hydropolitics*. 2014: Springer Science & Business Media.
9. Abtew, W., A.M. Melesse, and T. Dessalegne, *Spatial, inter and intra‐annual variability of the Upper Blue Nile Basin rainfall.* Hydrological Processes: An International Journal, 2009. **23**(21): p. 3075-3082.

10. Madson, A. and Y. Sheng, *Reservoir Induced Deformation Analysis for Several Filling and Operational Scenarios at the Grand Ethiopian Renaissance Dam Impoundment.* Remote Sensing, 2020. **12**(11): p. 1886.

11. Wheeler, K.G., et al., *Cooperative filling approaches for the grand ethiopian renaissance dam.* Water international, 2016. **41**(4): p. 611-634.

12. Beyene, A., *Reflections on the Grand Ethiopian Renaissance Dam.* Horn of Africa News, 2013. **14**.

13. Zhang, L., et al., *Impact of impoundment on groundwater seepage in the Three Gorges Dam in China based on CFCs and stable isotopes.* Environmental earth sciences, 2014. **72**(11): p. 4491-4500.

14. Zhao, Y., et al., *Groundwater level prediction of landslide based on classification and regression tree.* Geodesy and Geodynamics, 2016. **7**(5): p. 348-355.

15. Paronuzzi, P., E. Rigo, and A. Bolla, *Influence of filling–drawdown cycles of the Vajont reservoir on Mt. Toc slope stability.* Geomorphology, 2013. **191**: p. 75-93.

16. Zhang, M., Y. Dong, and P. Sun, *Impact of reservoir impoundment-caused groundwater level changes on regional slope stability: a case study in the Loess Plateau of Western China.* Environmental earth sciences, 2012. **66**(6): p. 1715-1725.

17. Fredlund, D.G. and H. Rahardjo, *Soil mechanics for unsaturated soils*. 1993: John Wiley & Sons.

18. Xia, M., et al., *Relationship between landslide stability and reservoir water level variation.* Bulletin of Engineering Geology and the Environment, 2015. **74**(3): p. 909-917.

19. Allen, C.R., *Reservoir-induced earthquakes and engineering policy.* Revista Geofísica, 1980. **13**: p. 20-24.

20. Talwani, P., *On the nature of reservoir-induced seismicity*, in *Seismicity Associated with Mines, Reservoirs and Fluid Injections*. 1997, Springer. p. 473-492.

21. Kerr, R.A. and R. Stone, *A human trigger for the great quake of Sichuan?* Science, 2009. **323**(5912): p. 322-322.

22. Ge, S., et al., *Did the Zipingpu reservoir trigger the 2008 Wenchuan earthquake?* Geophysical Research Letters, 2009. **36**(20).

23. Gahalaut, K., et al., *Influence of Tehri Reservoir Impoundment on Local Seismicity of Northwest Himalaya.* Bulletin of the Seismological Society of America, 2018. **108**(5B): p. 3119-3125.

24. Chander, R. and K. Chander, *Probable influence of Tehri reservoir load on earthquakes of the Garhwal Himalaya.* Current science, 1996: p. 291-299.

25. Enzminger, T.L., E.E. Small, and A.A. Borsa, *Accuracy of snow water equivalent estimated from GPS vertical displacements: A synthetic loading case study for western US mountains.* Water Resources Research, 2018. **54**(1): p. 581-599.

26. Tregoning, P., et al., *Detecting hydrologic deformation using GRACE and GPS.* Geophysical Research Letters, 2009. **36**(15).

27. Dumka, R., et al., *GPS Measurements of Deformation Caused by Seasonal Filling and Emptying Cycles of Four Hydroelectric Reservoirs in India.* Bulletin of the Seismological Society of America, 2018. **108**(5B): p. 2955-2966.

28. Neelmeijer, J., et al., *Ground Deformations around the Toktogul Reservoir, Kyrgyzstan, from Envisat ASAR and Sentinel-1 Data—A Case Study about the Impact of Atmospheric Corrections on InSAR Time Series.* Remote Sensing, 2018. **10**(3): p. 462.

29. Madson, A., Y. Sheng, and C. Song, *ICESat-derived lithospheric flexure as caused by an endorheic lake's expansion on the Tibetan Plateau and the comparison to modeled flexural responses.* Journal of Asian Earth Sciences, 2017. **148**: p. 142-152.

30. Gahalaut, V., et al., *InSAR and GPS measurements of crustal deformation due to seasonal loading of Tehri reservoir in Garhwal Himalaya, India.* Geophysical Journal International, 2017. **209**(1): p. 425-433.

31. Borsa, A.A., D.C. Agnew, and D.R. Cayan, *Ongoing drought-induced uplift in the western United States.* Science, 2014. **345**(6204): p. 1587-1590.

32. Kraner, M.L., W.E. Holt, and A.A. Borsa, *Seasonal nontectonic loading inferred from cGPS as a potential trigger for the M6. 0 South Napa earthquake.* Journal of Geophysical Research: Solid Earth, 2018. **123**(6): p. 5300-5322.

33. Simpson, D.W., *Seismicity changes associated with reservoir loading.* Engineering Geology, 1976. **10**(2-4): p. 123-150.

34. Baisch, S., et al., *Induced seismicity during the stimulation of a geothermal HFR reservoir in the Cooper Basin, Australia.* Bulletin of the Seismological Society of America, 2006. **96**(6): p. 2242-2256.

35. Bell, M.L. and A. Nur, *Strength changes due to reservoir‐induced pore pressure and stresses and application to Lake Oroville.* Journal of Geophysical Research: Solid Earth, 1978. **83**(B9): p. 4469-4483.

36. Chen, L. and P. Talwani, *Reservoir-induced seismicity in China*, in *Seismicity Caused by Mines, Fluid Injections, Reservoirs, and Oil Extraction*. 1998, Springer. p. 133-149.

37. Gahalaut, K., V. Gahalaut, and M. Pandey, *A new case of reservoir triggered seismicity: Govind Ballav Pant reservoir (Rihand dam), central India.* Tectonophysics, 2007. **439**(1-4): p. 171-178.

38. Ghaboussi, J. and E. Wilson, *Seismic analysis of earth dam-reservoir systems.* Journal of Soil Mechanics & Foundations Div, 1973. **99**(Proc Paper 10053).

39. Gupta, H., et al., *Pore pressure studies initiated in area of reservoir‐induced earthquakes in India.* Eos, Transactions American Geophysical Union, 2000. **81**(14): p. 145-151.

40. Gupta, H.K., *A review of recent studies of triggered earthquakes by artificial water reservoirs with special emphasis on earthquakes in Koyna, India.* Earth-Science Reviews, 2002. **58**(3-4): p. 279-310.

41. Mekkawi, M., J.-R. Grasso, and P.-A. Schnegg, *A long-lasting relaxation of seismicity at Aswan reservoir, Egypt, 1982-2001.* Bulletin of the Seismological Society of America, 2004. **94**(2): p. 479-492.

42. Roeloffs, E.A., *Fault stability changes induced beneath a reservoir with cyclic variations in water level.* Journal of Geophysical Research: Solid Earth, 1988. **93**(B3): p. 2107-2124.

43. Simpson, D.W. and S.K. Negmatullaev, *Induced seismicity at Nurek reservoir, Tadjikistan, USSR.* Bulletin of the Seismological Society of America, 1981. **71**(5): p. 1561-1586.

44. Talwani, P. and S. Acree, *Pore pressure diffusion and the mechanism of reservoir-induced seismicity*, in *Earthquake Prediction*. 1985, Springer. p. 947-965.

45. Zoback, M.D. and S. Hickman, *In situ study of the physical mechanisms controlling induced seismicity at Monticello Reservoir, South Carolina.* Journal of Geophysical Research: Solid Earth, 1982. **87**(B8): p. 6959-6974.

46. Tao, W., et al., *Impoundment of the Zipingpu reservoir and triggering of the 2008 Mw 7.9 Wenchuan earthquake, China.* Journal of Geophysical Research: Solid Earth, 2015. **120**(10): p. 7033-7047.

47. Simpson, D., W. Leith, and C. Scholz, *Two types of reservoir-induced seismicity.* Bulletin of the Seismological Society of America, 1988. **78**(6): p. 2025-2040.

48. Simpson, D., *Triggered earthquakes.* Annual Review of Earth and Planetary Sciences, 1986. **14**(1): p. 21-42.

49. Snow, D. *Geodynamics of seismic reservoirs*. in *Proceedings of the symposium on percolation through fissured rocks*. 1972.

50. Rajendran, K. and P. Talwani, *The role of elastic, undrained, and drained responses in triggering earthquakes at Monticello Reservoir, South Carolina.* Bulletin of the Seismological Society of America, 1992. **82**(4): p. 1867-1888.

51. Harris, R.A., *Introduction to special section: Stress triggers, stress shadows, and implications for seismic hazard.* Journal of Geophysical Research: Solid Earth, 1998. **103**(B10): p. 24347-24358.

52. King, G.C., R.S. Stein, and J. Lin, *Static stress changes and the triggering of earthquakes.* Bulletin of the Seismological Society of America, 1994. **84**(3): p. 935-953.

53. Stein, R.S., *The role of stress transfer in earthquake occurrence.* Nature, 1999. **402**(6762): p. 605.

54. Liu, L. and M.D. Zoback, *The effect of topography on the state of stress in the crust: application to the site of the Cajon Pass Scientific Drilling Project.* Journal of Geophysical Research: Solid Earth, 1992. **97**(B4): p. 5095-5108.

55. Jeffreys, H., *The Earth: its origin, history and physical constitution*. 1924: University Press.

56. Love, A.E.H., *A treatise on the mathematical theory of elasticity*. 2013: Cambridge university press.

57. Styron, R.H. and E.A. Hetland, *The weight of the mountains: Constraints on tectonic stress, friction, and fluid pressure in the 2008 Wenchuan earthquake from estimates of topographic loading.* Journal of Geophysical Research: Solid Earth, 2015. **120**(4): p. 2697-2716.

58. Sibson, R.H., *Frictional constraints on thrust, wrench and normal faults.* Nature, 1974. **249**(5457): p. 542.

59. Sibson, R.H., *A note on fault reactivation.* Journal of Structural Geology, 1985. **7**(6): p. 751-754.

60. Reasenberg, P.A. and R.W. Simpson, *Response of regional seismicity to the static stress change produced by the Loma Prieta earthquake.* Science, 1992. **255**(5052): p. 1687-1690.

61. Mulat, A.G. and S.A. Moges, *Assessment of the impact of the Grand Ethiopian Renaissance Dam on the performance of the High Aswan Dam.* Journal of Water Resource and Protection, 2014. **6**(06): p. 583.

62. IPoE *International Panel of Experts (IPoE). Grand Ethiopian Renaissance Dam Project, Final Report.* 2013.

63. Jameel, A.L., *The Grand Ethiopian Renaissance Dam: An Opportunity for Collaboration and Shared Benefits in the Eastern Nile Basin.* World Water and Food Security Lab, Amicus Brief, 2014: p. 1-17.

Chapter 3: Automated Water Level Monitoring at the Continental Scale from ICESat-2 ATLAS Photons

Abstract

Of the approximately 7,200 lakes and reservoirs larger than 1 km^2 in the Contiguous United States (CONUS) only ~430 (~6%) are actively gaged by the United States Geological Survey (USGS) or their partners and are available for download through the National Water Information System database. Remote sensing analysis provides a means to fill in these data gaps in order to glean a better understanding of the spatiotemporal water level changes across the CONUS. This study takes advantage of nearly two years' of NASA's ICESat-2 (IS-2) ATLAS photon data (ATL03 products) in order to derive water level changes for ~6,200 overlapping lakes and reservoirs (> 1 km^2) in the CONUS. Interactive visualizations of large spatial datasets are becoming more commonplace as data volumes for new Earth observing sensors have markedly increased in recent years. We present such a visualization created from an automated cluster computing workflow that utilizes tens of billions of ATLAS photons which derives water level changes for all of the overlapping lakes and reservoirs in the CONUS. Further, users of this interactive website can download segmented and clustered IS-2 photons for each individual waterbody so that they may run their own analysis. We examine ~56,000 IS-2 water level changes that are spatially and temporally coincident with water level changes from USGS gages and find high agreement with our results as compared to the *in situ* gage data. Around 86% (~48,000) of all overlapping IS-2 water

level change measurements are within ±25 cm of their gaged counterparts and the mean (median) absolute residual between the two products is 14 cm (7 cm).

1. Introduction

Lakes and reservoirs provide an important water resource for human use. These range from recreational activities, power generation, drinking water, agricultural irrigation, or other commercial and industrial uses. They are also notable indicators of climatic changes [1, 2] as well as local and regional drought events [3, 4]. Further, monitoring changes in lake and reservoir water levels are of a benefit to both local and regional water managers so that they may make more informed decisions about water management policies. This is especially true at the continental scale where the spatiotemporal changes in water levels are notably diverse across the landscape [5, 6]. To this end, continental scale monitoring of lake and reservoir water level changes is particularly difficult to accomplish solely by the utilization of *in situ* water level gages. This statement holds true for countries that have a meaningful *in situ* gaging and monitoring system in place. The United States and the United States Geological Survey's (USGS) National Water Information System (NWIS) is a notable example. To that end, Figure 1 highlights the spatial distribution of the ~7,200 lakes and reservoirs > 1 km^2 in the contiguous United States (CONUS). The USGS monitored water levels for only 430 (~6%) of those waterbodies within the past three years. In comparison, the water level monitoring technique described herein provides lake and reservoir water elevation measurements for 6,168 (~86%) waterbodies. This highlights a stark need to

utilize other methodologies and datasets for monitoring water level changes in the CONUS.

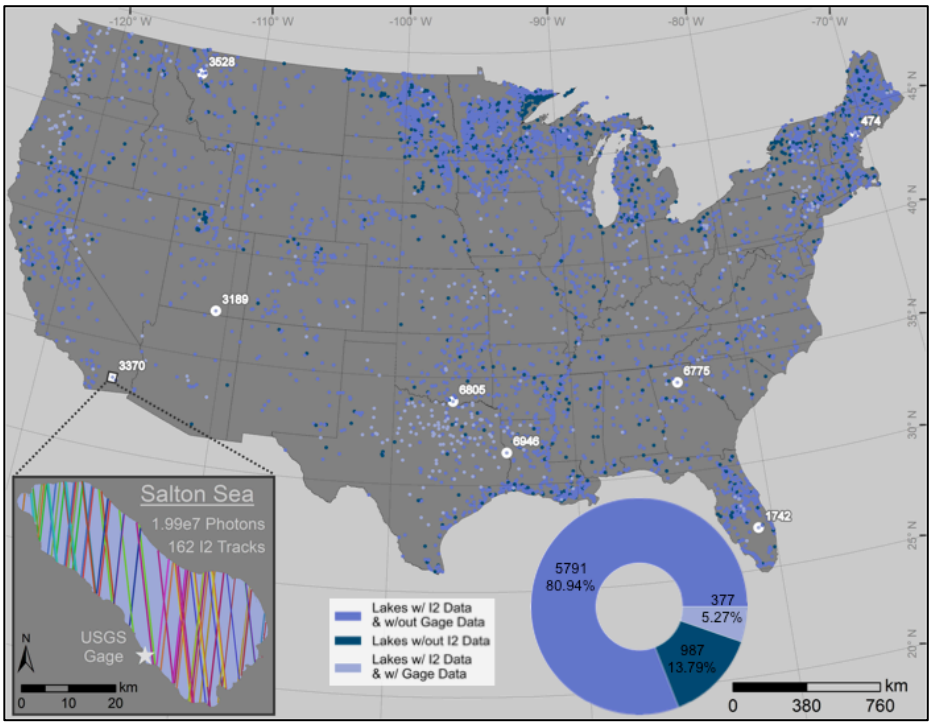

Figure 1. Waterbodies examined in this study classed by data availability. Centroids for all lakes and reservoirs > 1 km^2 within the CONUS are plotted and are classed by whether or not they have overlapping ICESat-2 data and/or *in situ* gage data. A donut plot shows the percentage breakdown of these waterbodies by their associated data availability. An inset map is present at the lower-left which displays an example lake within our waterbody mask along with its corresponding gage location and all spatially overlapping ICESat-2 tracks. The location of eight different example waterbodies are labeled by their ID and marked by white circles.

Remote sensing techniques have been used for many years to augment the use of *in situ* surface water level and storage measurements [7, 8]. For example, [9] used

early spaceborne radar altimetry data from the United States Navy's Geosat platform to monitor temporal changes in water levels within large lakes and inland seas. Further, more recent work utilizes a multi-platform approach for longer temporal scale lake level and storage changes [10-13] at notably larger spatial scales. However, most spaceborne altimeters are limited in their ability to meaningfully resolve water level changes for a large quantity of lakes. This is mostly due to spatial and temporal gaps in data coverage as well as the ground footprint size of the altimeter's energy source. The latter is especially true for radar altimeter platforms (e.g. Topex/Poseidon's ~1 km footprint). Spaceborne laser altimeters (like NASA's first ICESat mission) have notably smaller footprint diameters (~70 m) in comparison to their radar altimeter counterparts. The reduced footprint size of the altimeter allows for water level changes to be derived for waterbodies with smaller areal extents. This of course increases the number of lakes and reservoirs where meaningful measurements can be acquired and allows for a more complete picture of surface water changes. Several researchers have successfully utilized highly accurate ICESat laser altimetry products to monitor water level and storage changes over the period of the sensor's lifetime [14-17].

In 2018, NASA launched ICESat's successor, ICESat-2 (IS-2) into polar orbit. Like it's predecessor, IS-2's main scientific objectives revolve around cryospheric measurements in the polar regions [18]. However, secondary mission objectives do involve the monitoring of inland surface water height changes. The Advanced Topographic Laser Altimeter System (ATLAS) is the primary sensor onboard the IS-2 platform and is a notable improvement over ICESat's Geoscience Laser Altimeter System (GLAS). The ATLAS sensor utilizes three different pairs of beam tracks (six in

total), which enables an increased spatial coverage as compared to the single track of the GLAS sensor onboard the first ICESat mission. Further, the ATLAS sensor utilizes a novel photon counting approach that allows for an increase in both the precision and the accuracy of the vertical time-of-flight elevation measurements [19]. The ground footprint and the laser posting for the IS-2 platform have both been vastly improved from the GLAS sensor as well. The ATLAS sensor's footprint is ~17.5 m with an along-track posting of about 70 cm [18]. The specifications of the ATLAS sensor allow it to resolve more and smaller waterbodies than its predecessor. This is especially true when comparing it to spaceborne radar altimeter platforms with their notably larger footprints.

Recently, more water level and storage analyses have begun to utilize IS-2 ATLAS datasets into their studies. For example, [20, 21] employ ATLAS products to accurately monitor water level and storage changes for ~3,700 global reservoirs and for several lakes on the Tibetan Plateau (TP), respectively. [21] note that utilizing IS-2 data increases the quantity of measurable lakes on the TP by a factor of two as compared to ICESat datasets. An accuracy comparison of *in situ* water level gage readings with levels derived from IS-2 and a modern spaceborne altimeter (Satellite with ARgos and ALtika - SARAL) for around 30 reservoirs in China shows that the relative altimetric accuracy from IS-2 data is nearly two decimeters better than SARAL's [22]. These studies further highlight the quality of lake and reservoir monitoring products from IS-2 data as compared to current and previous spaceborne altimeters.

This study seeks to provide a novel automated workflow that utilizes the latest spaceborne altimetric products in order to monitor lake and reservoir water level changes for all waterbodies > 1 km^2 in the CONUS. An added objective of this work is to

provide accuracy assessments of these remotely sensed water level products as compared to thousands of temporally and spatially overlapping water level changes from USGS gage readings. Further, another goal of this study is to disseminate these results via an interactive website where an interested reader may better understand the spatiotemporal differences in lake and reservoir level changes at this scale. Lastly, this work seeks to provide these IS-2-based water level products to other users in the community in hopes that they will be of a benefit for future studies. This research was undertaken in order to provide baseline water level monitoring on a much larger scale than is traditionally possible with *in situ* monitoring. Further, knowledge of the accuracy of these remotely sensed spaceborne laser altimeter water level products validates the quality of the IS-2 ATLAS platform for use in future water level monitoring studies. We utilize careful processing techniques and cluster computing workflows with a validated waterbody extent product and all spatially overlapping ATL03 photons for lakes and reservoirs > 1 km^2 in the CONUS along with Landsat Dynamic Surface Water Extent (DSWE) products in order to satisfy our goals as laid out above.

2. Data and Methods

2.1 ICESat-2 ATLAS ATL03

This study uses photons from the IS-2 ATLAS platform in order to derive water level changes for all overlapping lakes > 1 km^2 in the CONUS. The spaceborne laser altimeter platform was launched in 2018 and the first available products were acquired on October 12 of the same year. The ATLAS sensor uses a beam splitting approach to separate photons into three different pairs of beams (six in total). These individual

beams have been named GT1L/GT1R, GT2L/GT2R, and GT3L/GT3R. The beams in each pair (e.g. GT1L/GT1R) are separated by ~90 m in the across-track direction and by ~2.5 km in the along-track direction and each of the three beam pairs are separated by ~3.3 km. Each pair consists of a "strong" beam and a "weak" beam where the "strong" beams have ~4 times the energy as the "weak" beams [18]. The ground footprint size and along-track spacing of the photons is ~17.5 m and ~70 cm, respectively. Photon data from the ATLAS sensor is provided to the scientific community in different data products at different levels of post-processing. There is an inland water surface height Level-3A product (ATL13) derived by the IS-2 science team that provides along-track water surface heights from overlapping lakes, reservoirs, bays, estuaries, and rivers [23]. This ATL13 data is derived from a Level-2 global geolocated photon data product (ATL03). The ATL13 dataset consists of estimated mean water surface heights within different segment lengths (~100 m and ~1 to 3 km). These segmented heights were derived from individual ATL03 photons that are within an inland body mask used in their processing workflow [24]. Users of this ATL13 product are reliant on the inland waterbody mask used in that workflow for the actual bodies of water that can be investigated using the ATL13 surface water heights. Previous versions of the ATL13 product did not allow for a complete analysis of all lakes > 1 km^2 in the CONUS due to their selection of that particular waterbody mask. We have not examined the most recent version of the ATL13 product (Version 3) to see if that is still the case. This study utilizes individual photons from the more robust ATL03 Level-2 product so that we have complete control over which photons will be processed in our water level workflows. The ATL03 products for this study were acquired from the

National Snow and Ice Data Center Distributed Active Archive Center (NSIDC DAAC) [25]. ATL03 photons are separated into 14 different data granules that encompass around 1/14 of a full IS-2 orbit. We acquired all ATL03 (Version 3) data granules overlapping the CONUS (Regions 01 and 02: ascending; Regions 06 and 07: descending) from the NSIDC servers. These consisted of 6,682 different ATL03 granules with a temporal range of October 2018 to July 2020. The ATL03 products consist of processed geolocated photons with the main fields of interest being the height above the ellipsoid (WGS84), time of photon event, various confidence flags, and geodetic latitude and longitude for the individual photons [26]. The IS-2 processing methodology employed for this research is further described in Section 2.3.

2.2 Waterbody Extents

This study uses spatial extents of all lakes and reservoirs larger than 1 km^2 in the CONUS as the initial waterbody mask for the ATL03 photons. The mask was derived from techniques described in [6] and underwent significant human-aided quality assurance and quality control in order to increase the quality of the waterbody extent product. The extents from this initial water mask were buffered inward by 30 m in order to reduce the quantity of edge photons (i.e. photons that capture elevation from the water/land periphery). This in-buffered extent file consists of 7,155 different waterbodies and the centroids from those extents are displayed in Figure 1. Using a custom lake mask allows complete control over the size and location of waterbodies used as an initial filter for the ATL03 photons. This is in comparison to the segmented photons of the ATL13 product that rely on their own proprietary waterbody masks. Our custom

waterbody mask is used in the water level workflow as described in Section 2.3 to initially filter ATL03 photons within full IS-2 granules into their spatially overlapping water boundaries.

The dynamics of surface water hydrologic systems (e.g. lakes and reservoirs) necessitate a need to further spatially filter ATL03 photons by waterbody extents that are as temporally coincident to each IS-2 data acquisition date and time as is possible. The waterbody mask described in the previous paragraph can be thought of as an initial static extent filter for lakes > 1km^2 in the CONUS. Landsat Level-3 Dynamic Surface Water Extent (DSWE) datasets are used in this study to further spatially filter ATL03 photons into their actual active bodies of water. DSWE data is a gridded Landsat Level 3 science product derived from Landsat Analysis Ready Data (ARD) that provides cell-by-cell information pertaining to the existence and condition of surface water extents [27]. Landsat ARD products consist of the most geometrically accurate Landsat 4-5 Thematic Mapper (TM), Landsat 7 Enhanced Thematic Mapper Plus (ETM+), and Landsat 8 Operational Land Imager (OLI)/ Thermal Infrared Sensor (TIRS) data that are processed to the highest scientific standards and level of processing required for direct use in assessing and monitoring landscape changes [28]. These DSWE products are used in the water level workflow as described in Section 2.3 to better spatially filter ATL03 photons into the actual water boundaries of the temporally closest DSWE grid.

2.3 Altimeter Water Levels

Each of the 6,682 ATL03 granules acquired from the NSIDC that overlap the CONUS were used as the basis of the IS-2 ATL03 processing workflow described in

this subsection. A parallel computing and spatial indexing approach was used to spatially filter the IS-2 granules due to the vast quantities of ATL03 photons as well as the number of vertices in the waterbody mask. To this end, each granule was sent to its own core within UCLA's Hoffman2 Cluster in an embarrassingly parallel computing workflow in order to split the granule photons into their respective spatially overlapping waterbody extents using the lake/reservoir mask as described in the first portion of Section 2.2. To speed up processing times the mask is clipped based on the buffered extent of the granule that is being processed prior to the assignment of the photons into their corresponding overlapping waterbody. This step uses spatial indexing techniques to rapidly determine which of the waterbodies in the mask are likely to contain the photons in the granule. This tremendously speeds up the precise spatial determination of the intersecting photons into their respective waterbodies. This initial photon intersection analysis is done for each of the six tracks (three "weak" and three "strong") for the granule and only photons with land, inland ice, and inland water "signal_conf_ph" values flagged as high confidence (i.e. 4) are saved for further processing. The outputs of this initial processing step are arrays of high confidence photons from all of the 6,682 granules for every track for each waterbody in the mask.

Several waterbodies in the lake/reservoir database exhibit notable inter- and intra-annual variations in areal extent. However, the initial waterbody mask provides only a snapshot of these dynamic areal extents. That said, care must be taken in order to filter out ATL03 photons that made it through the initial static spatial filtering process but do not actually fall within regions in which surface water was present during the time of the individual IS-2 granule acquisitions. These photons should be further filtered

using a dynamic waterbody extent mask in order to remove the false surface water photons from the database so that the final water level products will have an increased accuracy. Each waterbody that has photons within its extent after the initial static spatial filter was then passed to its own core for the dynamic spatial filtering process. This parallel filtering approach dramatically speeds up processing times. The individual ATL03 track photons for every date for a given waterbody were looped through and the temporally closest DSWE scene where less than 20% of that track's photons fell within the "cloud, cloud shadow, and snow" flagged regions were used to filter out photons that did not fall within the DSWE "water – high confidence" and "water – moderate confidence" flagged regions. The DSWE scene with the lowest percentage of cloudy photons was utilized for tracks where the 20% cloud threshold was not met by any DSWE scene acquired within ±4 years of that particular track's acquisition date. This dynamic spatial extent filtering process was utilized in order to remove as many of the false surface water photons over waterbodies that see larger spatial extent changes.

The individual tracks were then processed into "weak" beam and "strong" beam water levels for each date for every lake or reservoir in the database using an outlier filtering, segmenting, and clustering technique. To that end, photons in a given waterbody's track were converted from WGS84 ellipsoidal height into orthometric height using the EGM2008 geoid model. Next, outlier photons were filtered out using the "dem_h" data within the ATL03 product where all photons outside of the "dem_h" mean value - 200 m and the "dem_h" mean value + 100 m elevation range were excluded from further processing. These photons were then histogrammed into 1 m bins and the water level for the most-frequent bin was attained. This max bin level was used to

further filter out photons where only those that were within +3 m and -2 m of the max bin level were kept for further processing. The photons were then quantitatively and spatially segmented based on a maximum number of photons in a segment and a ~100 m distance threshold value. Segments consist of 50 photons for "strong" beams and 25 photons for "weak" beams where the photons in each segment are within ~100 m from each other. Segments containing less than 50 ("strong" beam) or 25 ("weak" beam) photons were removed from further processing. A histogram peak filter was run on each set of segmented (50 or 25) photons in order to remove false subsurface water signals (displayed in Figure 2). This peak filter entails histogramming the photons for each segment into 5 cm bins and then determining the three highest frequency bins. The bins containing less than 33% of the maximum frequency bin were removed. The water level of the maximum frequency bin of the remaining three bins was selected in order to utilize the bin that is typically associated with the actual surface reflectance (and not the sub surface reflectance photons). However, the water level of the second most frequent bin was selected if it was > 55 cm than the most frequent bin. This was done in case the segment's photons exhibited a higher number of pulses within a sub-surface return bin as compared to the actual surface return bin. Only photons in this segment that were within ±50 cm of the water level from the selected maximum frequency bin were kept for additional processing. A subsequent filtering step was applied on the segments where the photons with an absolute deviation outside of the median absolute deviation were removed from further processing. The final segment water levels were assigned by taking the mean of the remaining photons within each segment.

These segments were then clustered by along-track distance and water level using a density-based spatial clustering of applications with noise (DBSCAN) method with an epsilon value of 50 and a minimum segment sample setting of 1 [29]. The epsilon value is analogous to the maximum distance between two segments for one segment to be considered within the neighborhood of the other segment. Prior to clustering, the segments' latitudes were normalized such that an along-track distance of ~500 m was akin to ~50 in the data. This allowed the epsilon value of 50 to appropriately cluster the segments by their spatial distance values of 50 cm (water level) and ~500 m (along-track distance). Clusters consisting of only one segment were removed from the processing workflow. The mean cluster water levels were determined from the individual segments within each cluster. Clusters whose means that were outside of two standard deviations from the all-segment mean and outlier clusters that bring the all-cluster standard deviation above 20 cm were removed from further processing. Clusters with a mean absolute deviation greater than 2.5 cm were further filtered such that segments in a cluster whose water levels were outside of ±5 cm from the water level at the peak of the Gaussian-smoothed non-parametric kernel density estimation derived from the intra-cluster segment water levels were removed and a new cluster mean was derived. Otherwise, the previous cluster mean was used. The final lake level for the track was determined by the median of all remaining cluster water level values for each beam type. Figure 2 highlights the output of this workflow and displays photons, segments, and clusters for two example "strong" beam tracks.

2.4 In situ Gage Level and Altimeter Water Level Comparison

USGS surface water gage locations and their IDs were acquired from the USGS NWIS for twenty parameter codes related to surface water levels (61055, 62615, 00062, 72292, 99064, 72277, 62600, 72293, 62614, 99065, 72264, 99020, 62617, 00065, 72214, 72020, 30211, 62616, 30207, 72275). These 765 different gages were manually matched to their corresponding lake or reservoir in the initial static waterbody mask that was described at the beginning of Section 2.2. An automated spatial matching approach was considered, but a manual approach was eventually decided upon. This was mostly due to the occasional poor accuracy of the reported gage coordinates used as an input into the minimum distance based spatial matching approach. The 377 different centroids for each lake in our custom static waterbody mask that have both IS-2 and gage water levels are plotted in light blue within Figure 1. All available temporally coincident *in situ* water level readings for each waterbody with an active water level gage were acquired from the NWIS via the *hydrofunctions* python package from Martin Roberge and contributors (<https://github.com/mroberge/hydrofunctions>). Initial analysis of the gage levels sought to convert the many different water height datums to a uniform vertical datum to directly compare to the spatially and temporally overlapping water levels derived from the IS-2 processing workflow. However, this method was abandoned due to the poor quality of many of the gages' metadata. Most of the gages' vertical datum offsets were not precise or accurate enough to directly compare to the IS-2 water levels. Instead, we compared temporally coincident relative water level changes from the gages and the IS-2 water level products. Relative water level changes were derived for each of the gages' temporally overlapping IS-2 date pairs. The IS-2 acquisition times were converted to local gage times in order to acquire the proper

coincident gage readings. Further, only gage readings acquired within 24 hours from their corresponding IS-2 granule's acquisition time were utilized in the comparison. Lastly, when both daily values (DVs) and instantaneous values (IVs) were available for a water level gage the temporally closest between the two IVs and DVs as compared to the IS-2 data acquisition time was used. This allowed for the utilization of the temporally closest gage readings to be compared to their IS-2 water level counterparts. These relative water level changes from temporally overlapping USGS gage data were ultimately used to compare to the IS-2 relative water level changes in order to assess the accuracy of our ATL03-derived water level changes as described in the workflow in in the previous section.

3. Results

3.1 Altimeter Water Levels and Storage

Water levels were successfully derived using the workflow described in Section 2.3 for 6,168 different lakes within the CONUS. Approximately 79% (4,845) of those lakes had more than a single day's IS-2 water level measurement allowing for a time series of water level changes. It is not practical to display to the reader the entirety of our water level results from this study in static graphs. However, the results from all ~6,000 lakes and reservoirs examined in this study are viewable via an online interactive website where an interested reader may better understand the spatiotemporal differences in water level/storage changes at this scale <https://icesat2waterlevelmapping.s3-us-west-1.amazonaws.com/overViewMap.html>. The link provides an overview map showing the location of all 6,168 lakes in this study.

Selecting an individual lake allows the user to view the interactive water level change time series separated by track and beam type as well as the interactive daily data plots for each date in the time series. These daily plots display the ATL03 photons, the segments, and their clusters as described in Section 2.3 and are separated by track and beam type for a single date for the selected lake. Two static examples of the daily data plots are provided in Figure 2 for a "strong" beam of a single track for two separate waterbodies. This figure shows two example tracks broken down by their filtered photons, segmented photons, and clustered segments. Further, each individual daily date pages links to an interactive map where the beam segments for this date are overlaid on a true-color basemap. We also provide sample water level time series from four reservoirs and four lakes examined in this study along with their *in situ* gage water levels in Figure 3. The location of the waterbodies plotted in Figures 2 and 3 are denoted within Figure 1 (white circles). The complete IS-2 derived water level results from our processing workflow are available at the previously mentioned link. An examination of lake IDs 1742 and 3370 within Figure 3 provides evidence that our processing methodology is capable of resolving water level changes at least at the decimeter scale.

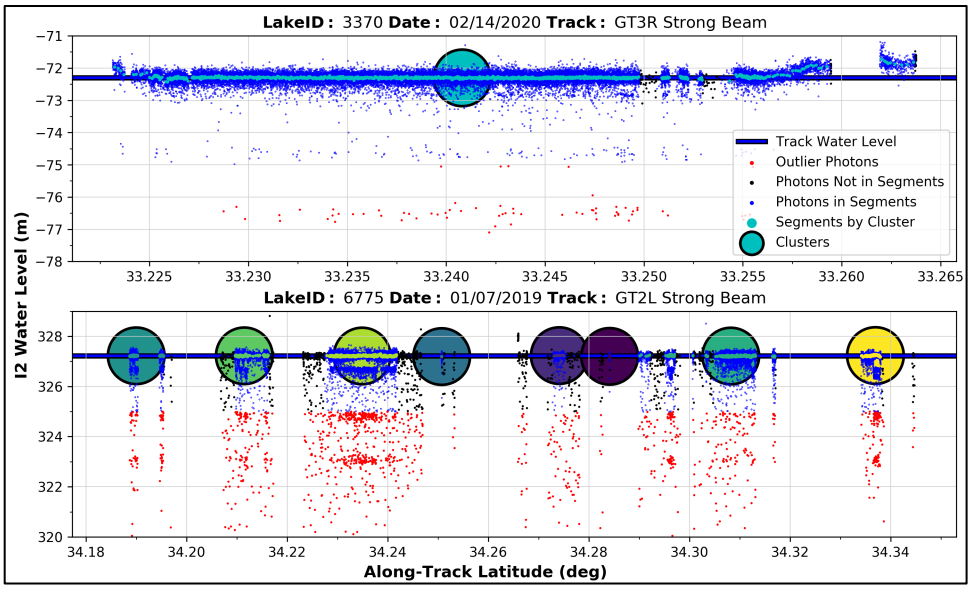

Figure 2. Example ATL03 photons, segmented photons, and clustered segments for a daily data plot at an example lake and reservoir. Each subplot is for a single "strong" beam track and visually shows the photon to cluster hierarchy of our processing workflow. Red photons are filtered outliers, black photons are not used in the segmentation, blue photons are assigned to a segment, segments are colored based on their assigned cluster, and clusters consist of those segments of the same color. The thick blue/black horizontal line is the assigned water level for that track based on the cluster median.

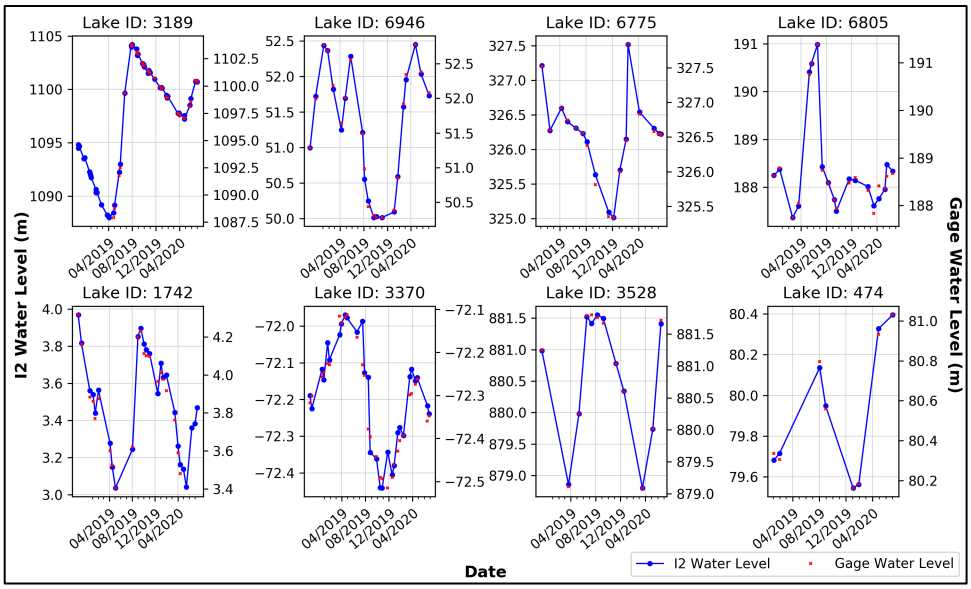

Figure 3. Comparison of IS-2 and gage derived water level time series for eight selected reservoirs and lakes. The first row consists of reservoirs and the second row consists of natural lakes. IS-2 water levels (blue) are orthometric (EGM2008) and gage water (red) levels are based on the individual gages' reporting datum. IS-2 water levels are plotted on the first y-axis (left) and the gage water levels are plotted on the second y-axis (right).

3.2 In situ Gage Level and Altimeter Water Level Comparison

There are 55,909 temporally overlapping *in situ* and IS-2 derived ("strong" beam only) relative water level change measurements from 611 unique dates and 347 different gaged lakes in our database. A scatter plot showing the relative water level measurement comparisons for all ~56,000 of these points is plotted in Figure 4 (R^2 = 0.96) with a notable positive correlation. Two zoomed insets (-1 m to 1 m and -0.5 m to 0.5 m) are provided in order to show a more focused comparison centered on the origin. The IS-2 water level changes were less than their *in situ* gages counterparts in roughly

52% of the gage and "strong" beam IS-2 comparisons while around 48% were more than the gaged water level measurements. The mean (median) absolute residual difference between the two products is ~14 cm (~7 cm) with a standard deviation of ~25 cm. Further, these residuals match quite well with other IS-2 water level studies [20]. This provides further evidence about the quality of our ATLAS derived water level products described herein.

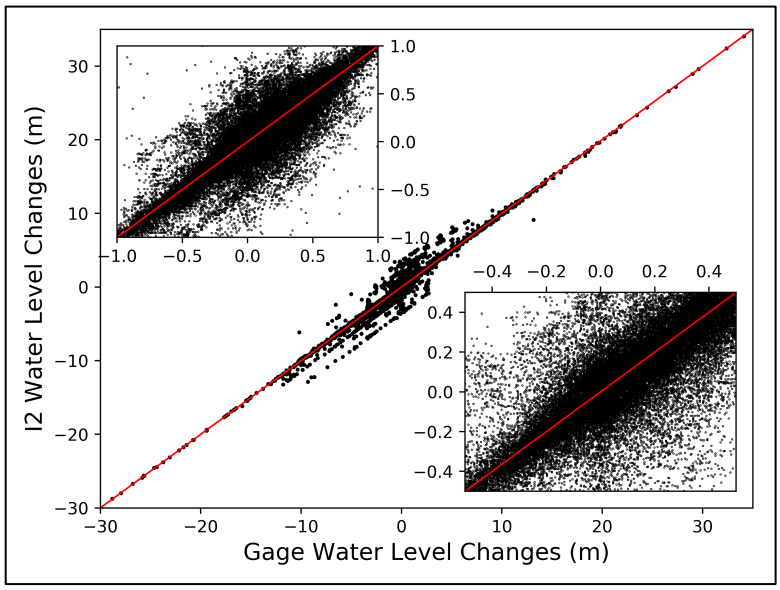

Figure 4. Gage derived relative water level changes versus "strong" beam IS-2 derived relative water level changes. The units for the main plot and the two subplots are in meters. The one-to-one line is plotted in red. Two zoomed inset maps are present and are focused at the origin point 0,0. The water level comparisons in the upper-left inset range from -1 m to 1 m and the comparisons in the lower-right range from -0.5 m to 0.5 m. The IS-2 water level changes are from the ATLAS "strong" beams only.

We plot a frequency histogram of those differences in Figure 5 in order to better examine the spread of the relative water residuals. This plot shows that ~86% (47,914)

of the 55,909 temporally overlapping "strong" beam IS-2 derived water level change measurements are within ±25 cm of their gaged counterparts. Further, ~60% (33,522) and ~37% (20,735) of the IS-2 water level changes are within ±10 and ±5 cm of their corresponding *in situ* gaged measurements, respectively. It is evident that the vast majority of our IS-2 derived water level changes are quite accurate as compared to their temporally overlapping *in situ* gaged counterparts. These results are proof positive that IS-2 ATLAS photons can meaningfully monitor water level changes at the continental scale for a variety of surface waterbody types.

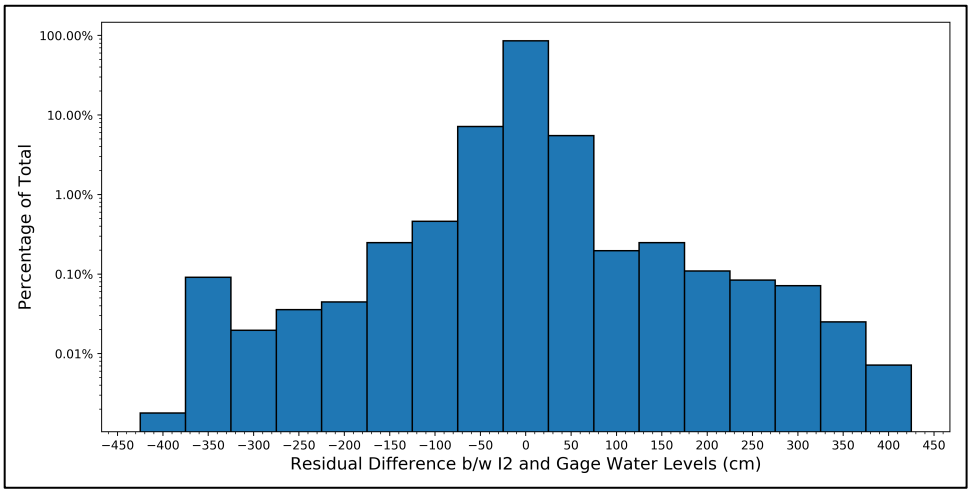

Figure 5. Frequency histogram of the residual differences from the "strong" beam IS-2 and gaged relative water level changes. Each bin is 50 cm wide and is centered on the 0 cm residual difference. Note the y-axis unit is the percentage of IS-2 and gaged comparisons with residual water level differences within each particular bin's range. The y-axis is on a base 10 logarithmic scale in order to show the lower frequency bins at the tails. The IS-2 water level changes are from the ATLAS "strong" beams only.

4. Discussion

4.1 Altimeter Water Levels

Water levels were successfully determined for 6,168 lakes within the CONUS using the methodology described in Section 2.3. We note that this methodology uses the global geolocated ATL03 photons as the main IS-2 input and that these photons are the basis for higher level IS-2 products (e.g. ATL08 and ATL13). The ATL03 photons were utilized in this study as it allows for complete control over the associated waterbody mask used as the initial photon spatial filter as well as for control over segmenting and clustering of the photons. However, this does come with drawbacks as the shear volume of ATL03 data is much larger than the post-processed and segmented higher-level products (e.g. ATL08). These higher-level IS-2 products would be less computationally expensive to download and process as compared to the ATL03 data. However, the user would then be reliant on their post-processing segmenting algorithms (e.g. ATL08 or ATL13) as well as their waterbody mask (e.g. ATL13). We note that some researchers have had success using the ATL08 products for water level studies [20]. Using the ATL08 product still allows for the utilization of a custom waterbody mask. However, the user is dependent on the segmented photons provided in that product.

We note that water level errors can occur during the second spatial filtering step in our workflow where the temporally closest DSWE product is used to further filter out ATL03 photons that do not fall within areas actively classified as surface water. These errors can appear for waterbodies that see large fluxes in areal extent between IS-2 data acquisitions and their temporally closest DSWE acquisition (e.g. some reservoirs and ephemeral lakes). In particular this can happen when ATL03 photons fall on regions of inactive surface water within the initial waterbody mask and those regions

subsequently fill in with water during the time between the IS-2 photon acquisition and the temporally closest DSWE acquisition. In those cases, the DSWE will not filter out the photons because the workflow believes that they are over active water regions. Future work involves increasing the number of remotely sensed datasets (e.g. Planet and Sentinel) used in the secondary spatial filtering step in order to reduce the temporal lag between the IS-2 data acquisition and the acquisition of the satellite derived active surface water check data. This will help to alleviate the aforementioned issue.

The benefits of our photon filtering, segmenting, and clustering technique are highlighted in Figure 2. These two different examples show how this methodology is able to determine the individual track water level by automatically removing outlier photons and appropriately grouping the remaining photons into meaningful segments and clusters. For example, the bottom plot shows the along-track water levels for a single "strong" beam acquired over a reservoir in Georgia. The data gaps present in the along-track direction of the IS-2 path for this track denote regions where the IS-2 overpass goes through several "fingers" of the reservoir where the pulses received at the sensor alternate between water photons and land photons. These types of overpasses are more complicated than a single continuous track through water (as in the top plot within the same figure). This alternating land-water overpass example highlights the robustness of our segmenting and clustering methodology. It is also evident in both plots within Figure 2 that there are multiple surface returns apparent around -2 m and -4 m from the actual water level. These double echoes are a known issue that often occurs over smooth open water surfaces and is likely caused by after-

pulses or electronic noise after the primary surface return [30]. These two plots within Figure 2 further highlight the robustness of our IS-2 water level workflow.

Our workflow separates water level change products into both "strong" and "weak" beams. We compared the IS-2 water level from both the "strong" and "weak" beams for the 88,046 different water level measurements that overlap with the gage data and found that the mean (median) absolute residual difference between the "strong" and "weak" beam water levels is ~4 cm (~2 cm) with a standard deviation of ~8 cm. Figure 6 shows a frequency histogram of the spread of "strong" and "weak" beam water level residuals. This plot shows that ~95% (83,219) of the 88,046 overlapping "strong" and "weak" beam IS-2 derived water level measurements are within ±10 cm of each other. Further, ~53% (46,540) and ~25% (22,086) of these "strong" and "weak" beam IS-2 water levels are within ±2.5 and ±1 cm of each other, respectively. The "strong" beam water levels are less than their "weak" beam water level counterparts in around 65% (56,822) of these beam comparisons. The majority of the "strong" beam water levels are likely lower than their "weak" beam counterparts due to the increased energy (~4x) of the "strong" photons as compared to the "weak" photons. This increased energy likely allows for more penetration into the water's subsurface and slightly decreases (or pulls down) the water levels for the "strong" beams. This comparison provides strong evidence for the utilization of both beam types for water level change analyses, assuming that the potential several centimeter difference between the two beams is acceptable for the particular use case.

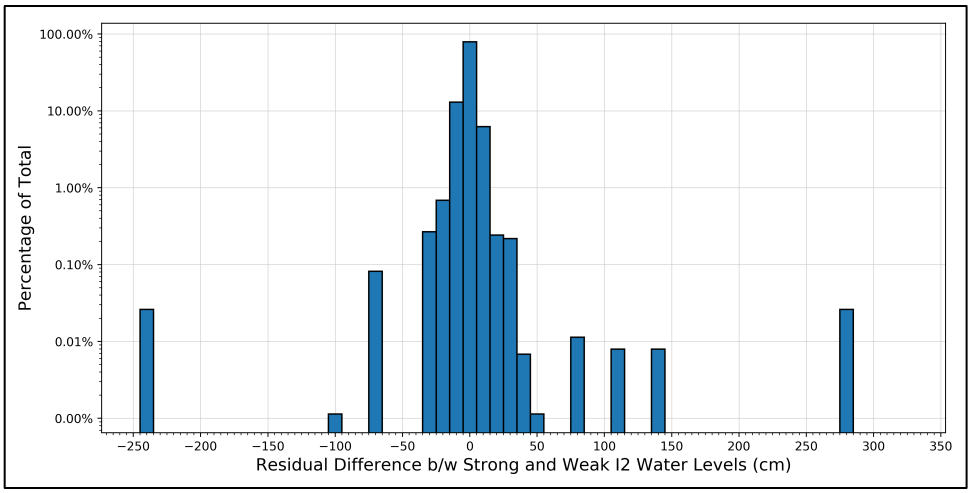

Figure 6. Frequency histogram of the residual differences from the "strong" beam and "weak" beam IS-2 derived water levels. Each bin is 10 cm wide and is centered on the 0 cm water level difference. Note the y-axis unit is the percentage of "strong" beam and "weak" beam comparisons with residual water level differences within each particular bin's range. The y-axis is on a base 10 logarithmic scale in order to show the lower frequency bins at the tails.

4.2 In situ Gage Level and Altimeter Water Level Comparison

Figures 4 and 5 show a scatter plot of the relative water level changes from *in situ* gages and IS-2 derived water levels from "strong" beams only as well as a frequency histogram of those relative water level changes, respectively. We compared the relative water level changes instead of the individual water levels due to the fact that the absolute water level readings from many of the gages were not precise enough to directly compare to their IS-2 derived water level counterparts. For example, many gage readings are given in a local vertical datum, and in the best cases, the datum offsets are provided in the gages' metadata. These offsets would allow those measurements to be

directly comparable to the IS-2 derived water levels that are in a known vertical datum. However, we find that even in the gages that do provide vertical datum offsets the accuracy of those offsets is not known or is not precise enough for a trustworthy IS-2 comparison. Therefore, we have chosen to compare the relative water level differences between the temporally overlapping gage measurements and our IS-2 water level change results. These gage datum differences are evident in Figure 3 where the IS-2 water level and gage water level time series are plotted for eight bodies of water. The second y-axis (right) shows the gage water level and it is evident that the gage datums are offset from the orthometric heights of the IS-2 time series. We expect these two y-axes to be offset as the gage datums have not been converted due to the issues mentioned at the beginning of this paragraph. Using the relative water level differences between two coincident dates allows us to disregard this datum-offset issue and still provides for a meaningful and direct accuracy assessment between the gage derived and the IS-2 derived water levels. Further, since we are comparing the relative water level change accuracy (i.e. the water level change from Time A to Time B) the actual water level differences are likely less than the reported 14 cm (mean) and 7 cm (median) as the uncertainty and error of the direct water level comparisons are effectively doubled when comparing the relative water level changes.

In order to glean a better understanding of the relative gage and IS-2 derived water level change differences we separated the waterbodies into two different categories: 1) natural lakes and 2) reservoirs. Comparison statistics for these two types of waterbodies were then calculated and we found that the mean (median) absolute residual differences between the two IS-2 waterbody categories and the gage products

are ~19 cm (~7 cm) and ~13 cm (~5 cm) for the "natural lake" and "reservoir" classifications, respectively. We note that ~87%, ~60%, ~37% and ~91%, ~75%, ~51% of the temporally overlapping "strong" beam IS-2 derived water level change measurements are within ±25, ±10, and ±5 cm of their corresponding *in situ* gaged measurements for the "natural lake" and "reservoir" classifications, respectively. This analysis shows that waterbodies classed as reservoirs tend have more accurate results as compared to their gage-derived relative water level changes. Future work entails classifying waterbodies using a more detailed classification scheme and taking into account seasonality of these waterbodies.

Further, in many cases we do not expect the water level changes from the IS-2 data and the *in situ* gage data to be the same. The gage readings are merely a water level snapshot at a single location on the waterbody's surface. Lake and reservoir water levels are highly dynamic across the water's surface and this dynamism leads to uneven water elevations for the waterbody. To that end, along-track IS-2 photons are collecting surface water return photons through a cross-section of the waterbody, and these surface water photons will have different water elevations as caused by the multitude of factors that allow for the uneven surface water levels. These factors include wind speed and direction, gravity effects, seiches, pressure oscillations, as well as lake connectivity and are the cause for uneven water levels and slopes across a given body of water. A waterbody is not expected to have a uniformly flat surface and a water level measurement at one location within a lake or a reservoir is not expected to be the same measurement at a different location within the same body of water. So, we expect there

to be some differences in the IS-2 water levels and the gage water levels presented in Figures 3 – 5.

The gage and IS-2 comparisons shown in Figures 4 - 5 and discussed in the preceding paragraphs as well as in Section 3.2 utilize IS-2 water level changes from ATLAS "strong" beams only. In comparison to those results, there are 44,308 temporally overlapping *in situ* and IS-2 derived ("weak" beam only) relative water level change measurements from 607 unique dates and 340 different gaged lakes in our database. A scatter plot showing the relative water level measurement comparisons for all ~44,000 of these "weak" points is plotted in Figure S1 (R^2 = 0.96). Similar to the "strong" gage comparisons, the IS-2 water level changes were less than their gaged counterparts for roughly 52% of the gage and "weak" beam comparisons, while around 48% were more than the gaged water level measurements. The mean (median) absolute residual difference between the two products is ~15 cm (~8 cm) with a standard deviation of ~26 cm. These results are around 1 cm greater than their "strong" beam gage comparison counterparts. Figure S2 shows a frequency histogram of the spread of relative water level change residuals. This plot shows that ~85% (37,874) of the 44,308 temporally overlapping "weak" beam IS-2 derived water level change measurements are within ±25 cm of their gaged counterparts. Further, ~59% (26,001) and ~35% (15,430) of the IS-2 water level changes are within ±10 and ±5 cm of their corresponding gaged measurements, respectively. This comparisons between the "weak" beam and gage derived relative water level changes as well as the IS-2 derived "strong" and "weak" beam water level residual comparisons in Figure 6 show that the methodology presented herein is capable of providing accurate water level changes

from both types of ATLAS beams. This is important as it means that both "strong" and "weak" beams can be utilized to derive water level changes, which implies that more waterbodies can be investigated and that more water level data points can be derived as compared to a single "strong" beam analysis only.

5. Conclusion

This research has highlighted an automated cluster computing workflow that utilizes IS-2 ATLAS ATL03 photons to accurately determine water level changes for all waterbodies > 1 km^2 in the CONUS. To this end, water levels were successfully derived for 6,168 different lakes and reservoirs using the methodology described herein. A comparison of relative water level changes between *in situ* gage measurements and our IS-2 water level changes showed an absolute mean (median) residual of ~14 cm (~7 cm) with a standard deviation of ~25 cm. Around 86% of the temporally overlapping "strong" beam IS-2 derived water level change measurements were within ±25 cm of their gaged counterparts. Further, ~60% and ~37% of these IS-2 water level changes were within ±10 and ±5 cm of their corresponding *in situ* gaged measurements. A comparison of the "strong" and "weak" beam water level measurements showed that the mean (median) absolute residual differences between the two beams was ~4 cm (~2 cm) and had a standard deviation of ~8 cm. Around 95% of the "strong" and "weak" beam IS-2 derived water level measurements were within ±10 cm of each other. An interactive website was created so that interested readers may better understand the spatiotemporal differences in lake and reservoir level changes at this scale. This research was undertaken in order to provide baseline water level monitoring on a much

larger scale than is traditionally possible with *in situ* monitoring. Further, knowledge of the accuracy of these remotely sensed spaceborne laser altimeter water level products validates the quality of the IS-2 ATLAS platform for use in future water level monitoring studies.

Acknowledgments

This work used computational and storage services associated with the Hoffman2 Shared Cluster provided by the UCLA Institute for Digital Research and Education's Research Technology Group. We thank Martin Roberge for hosting his hydrofunctions project on github (<https://github.com/mroberge/hydrofunctions >). We thank Frank Madson for his help in figure creation.

Supplementary Material

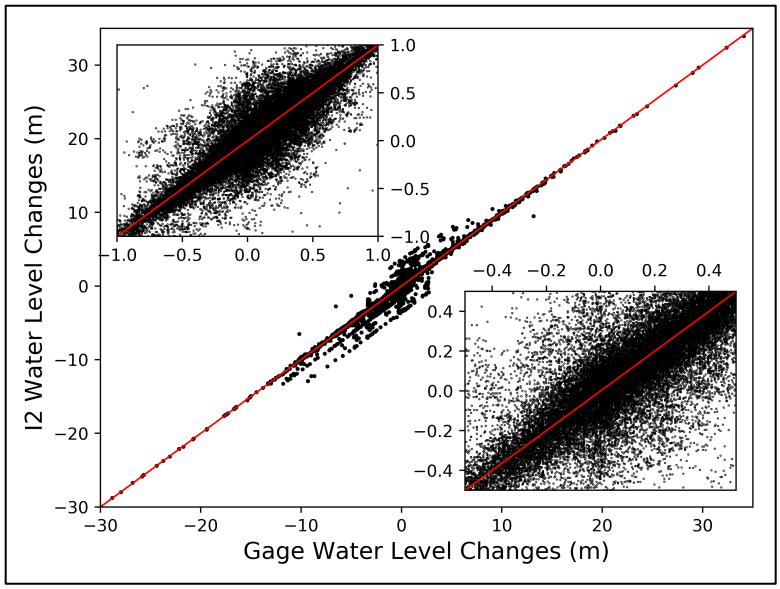

Figure S1. Gage derived relative water level changes versus "weak" beam IS-2 derived relative water level changes. The units for the main plot and the two subplots are in

meters. The one-to-one line is plotted in red. Two zoomed inset maps are present and are focused at the origin point 0,0. The water level comparisons in the upper-left inset range from -1 m to 1 m and the comparisons in the lower-right range from -0.5 m to 0.5 m. The IS-2 water level changes are from the ATLAS " weak " beams only.

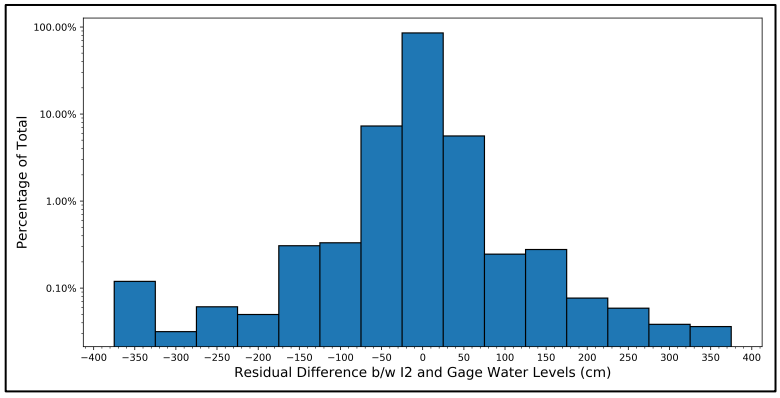

Figure S2. Frequency histogram of the residual differences from the "weak" beam IS-2 and gaged relative water level changes. Each bin is 50 cm wide and is centered on the 0 cm residual difference. Note the y-axis unit is the percentage of IS-2 and gaged comparisons with residual water level differences within each particular bin's range. The y-axis is on a base 10 logarithmic scale in order to show the lower frequency bins at the tails. The IS-2 water level changes are from the ATLAS "weak" beams only.

References

1. Vörösmarty, C.J., et al., *Global water resources: vulnerability from climate change and population growth.* science, 2000. **289**(5477): p. 284-288.
2. Lei, Y., et al., *Response of inland lake dynamics over the Tibetan Plateau to climate change.* Climatic Change, 2014. **125**(2): p. 281-290.
3. Birkett, C., *Synergistic remote sensing of Lake Chad: Variability of basin inundation.* Remote sensing of environment, 2000. **72**(2): p. 218-236.
4. West, H., N. Quinn, and M. Horswell, *Remote sensing for drought monitoring & impact assessment: Progress, past challenges and future opportunities.* Remote Sensing of Environment, 2019. **232**: p. 111291.
5. Song, C., B. Huang, and L. Ke, *Modeling and analysis of lake water storage changes on the Tibetan Plateau using multi-mission satellite data.* Remote Sensing of Environment, 2013. **135**: p. 25-35.
6. Sheng, Y., et al., *Representative lake water extent mapping at continental scales using multi-temporal Landsat-8 imagery.* Remote Sensing of Environment, 2016. **185**: p. 129-141.
7. Birkett, C., *Radar altimetry: a new concept in monitoring lake level changes.* Eos, Transactions American Geophysical Union, 1994. **75**(24): p. 273-275.
8. Birkett, C.M. and I.M. Mason, *A new global lakes database for a remote sensing program studying climatically sensitive large lakes.* Journal of Great Lakes Research, 1995. **21**(3): p. 307-318.
9. Morris, C.S. and S.K. Gill, *Variation of Great Lakes water levels derived from Geosat altimetry.* Water Resources Research, 1994. **30**(4): p. 1009-1017.

10. Birkett, C., et al., *From research to operations: The USDA global reservoir and lake monitor*, in *Coastal altimetry*. 2011, Springer. p. 19-50.

11. Crétaux, J.-F., et al., *Lake volume monitoring from space.* Surveys in Geophysics, 2016. **37**(2): p. 269-305.

12. Crétaux, J.-F., et al., *SOLS: A lake database to monitor in the Near Real Time water level and storage variations from remote sensing data.* Advances in space research, 2011. **47**(9): p. 1497-1507.

13. Duan, Z. and W. Bastiaanssen, *Estimating water volume variations in lakes and reservoirs from four operational satellite altimetry databases and satellite imagery data.* Remote Sensing of Environment, 2013. **134**: p. 403-416.

14. Song, C., et al., *Heterogeneous glacial lake changes and links of lake expansions to the rapid thinning of adjacent glacier termini in the Himalayas.* Geomorphology, 2017. **280**: p. 30-38.

15. Yuan, T., et al., *Mapping forested floodplain topography using InSAR and radar altimetry.* IEEE Journal of Selected Topics in Applied Earth Observations and Remote Sensing, 2019. **12**(12): p. 5189-5198.

16. Zhang, G., et al., *Monitoring lake level changes on the Tibetan Plateau using ICESat altimetry data (2003–2009).* Remote Sensing of Environment, 2011. **115**(7): p. 1733-1742.

17. Madson, A., Y. Sheng, and C. Song, *ICESat-derived lithospheric flexure as caused by an endorheic lake's expansion on the Tibetan Plateau and the comparison to modeled flexural responses.* Journal of Asian Earth Sciences, 2017. **148**: p. 142-152.

18. Markus, T., et al., *The Ice, Cloud, and land Elevation Satellite-2 (ICESat-2): science requirements, concept, and implementation.* Remote Sensing of Environment, 2017. **190**: p. 260-273.

19. Neumann, T.A., et al., *The Ice, Cloud, and Land Elevation Satellite–2 Mission: A global geolocated photon product derived from the advanced topographic laser altimeter system.* Remote sensing of environment, 2019. **233**: p. 111325.

20. Ryan, J.C., et al., *Global Characterization of Inland Water Reservoirs Using ICESat‐2 Altimetry and Climate Reanalysis.* Geophysical Research Letters, 2020. **47**(17): p. e2020GL088543.

21. Zhang, G., W. Chen, and H. Xie, *Tibetan Plateau's lake level and volume changes from NASA's ICESat/ICESat‐2 and Landsat Missions.* Geophysical Research Letters, 2019. **46**(22): p. 13107-13118.

22. Yuan, C., P. Gong, and Y. Bai, *Performance Assessment of ICESat-2 Laser Altimeter Data for Water-Level Measurement over Lakes and Reservoirs in China.* Remote Sensing, 2020. **12**(5): p. 770.

23. Jasinski, M., et al., *ATLAS/ICESat-2 L3A Inland Water Surface Height, Version 3.[Indicate subset used]. Boulder, Colorado USA. NASA National Snow and Ice Data Center Distributed Active Archive Center.* https://doi.org/10.5067/ATLAS/ATL13.003*. [Accessed September 2020].* 2020.

24. Jasinski, M., et al., *Algorithm Theoretical Basis Document (ATBD) for Inland Water Data Products, ATL13, Version 3, Release Date March 1, 2020, NASA Goddard Space Flight Center, Greenbelt, MD,112 pp.* https://doi:10.5067/L870NVUK02YA*. (March 2020).* 2020.

25. Neumann, T.A., et al., *TLAS/ICESat-2 L2A Global Geolocated Photon Data, Version 3. Boulder, Colorado USA. NASA National Snow and Ice Data Center Distributed Active Archive Center. doi:* https://doi.org/10.5067/ATLAS/ATL03.003*. [Accessed on October 2020].* 2020.

26. Luthcke, S., et al., *Algorithm Theoretical Basis Document (ATBD) for ATL03g ICESat-2 Receive Photon Geolocation, NASA Goddard Space Flight Center, Greenbelt, MD, 53 pp. (October 2019).*

27. Jones, J.W., *Improved automated detection of subpixel-scale inundation—Revised dynamic surface water extent (dswe) partial surface water tests.* Remote Sensing, 2019. **11**(4): p. 374.

28. Dwyer, J.L., et al., *Analysis ready data: enabling analysis of the Landsat archive.* Remote Sensing, 2018. **10**(9): p. 1363.

29. Ester, M., et al. *A density-based algorithm for discovering clusters in large spatial databases with noise*. in *Kdd*. 1996.

30. Luthcke, S., et al., *ATL03 Version 3 Known Issues.* 2020.

Conclusion

This dissertation sought to provide a better understanding of some of the mechanisms, magnitudes, and effects behind large-scale lacustrine changes. This work utilized remote sensing datasets from spaceborne optical sensors and lidar altimeters, *in situ* water level measurements, and localized Earth models in order to increase that understanding. A combination of products derived from both *in situ* data and remotely sensed spaceborne datasets coupled with modern modeling and computational capabilities helped to provide the means to paint a more complete picture of the diverse connections between the magnitudes, mechanisms, and effects of large-scale lacustrine changes.

In particular, the first two chapters examined the magnitudes of change and their effects on the surrounding lithosphere at the Grand Ethiopian Renaissance Dam (GERD), a large reservoir in Ethiopia. The mechanisms behind these changes are related to direct anthropogenic impacts (e.g. Dam building and riverine impoundment). A number of remotely sensed digital surface models (DSMs) were analyzed and the most accurate surface model was determined by its comparison to spaceborne altimeter data. The areal extent and volumetric content for the GERD impoundment at 1 m water level increments (from 500 to 640 m) was calculated and hypsometric curves for water level versus areal extent and water load along with areal extent versus water load were derived. Cubic and quadratic fits of these curves were calculated, and very high R-squared values were found for each. The associated coefficients were used to derive areal extent and volumetric content at sub-meter water level changes (e.g., 0.001 m) for each day in the GERD filling and seasonal operational scenarios. To that end, daily

water level, areal extent, water storage, inflow, and outflow values were created for 55 different filling scenarios as well as for 5 different operational strategies at the GERD. The hydrologic load fluxes were found to be highly dependent on the chosen filling and operational strategies. The accumulated annual reservoir storage during the initial impoundment directly affects the time it takes to fill the reservoir to its maximum water level of 640 m, and seasonal reservoir operations have a large effect on the amplitude of seasonal hydrologic load fluctuations. The daily hydrologic load changes were used as the main inputs into cluster computing workflows where daily elastic deformation and Coulomb stresses were determined for the different impoundment and operational strategies.

The elastic responses to several filling and operational strategies for the GERD were modeled using a localized spherically symmetric, non-rotating, elastic, and isotropic (SNREI) Earth model. The amplitude and extent of the flexural response was mostly dependent on the underlying rheology as well as the timing and amount of the hydrologic forcing. The marked seasonal hydrologic regime at the GERD impoundment was found to play a major role in the temporal dynamics of the load-induced flexural response for the different filling scenarios that were investigated. The overall magnitude of the vertical and horizontal displacements for the five examined operational scenarios were highly varied. The deformation was found to be dependent on the input natural hydrologic variables (e.g., inflow, seepage, actual ET) as well as the different operational variables (i.e., outflow/reservoir releases as they are related to hydropower generation). Subsequently, the annual load density along with the varied reservoir inflow and outflow rates and release timings were found to affect the maximum accumulated

seasonal displacement as well as the distance with which the flexural response occurred away from the associated hydrologic load centroid. The magnitudes of the hydrologic-induced deformation are directly related to the size and timing of reservoir fluxes, and an increased knowledge of the extent and magnitude of this deformation provides meaningful information to stakeholders so that they may better understand the effects from many different impoundment and operational strategies.

The same hydrologic load arrays for the GERD were used to calculate the Coulomb stress on an optimal plane for each full-resolution cell (~30 m x ~30 m) in the model domain at 1 km depth increments from the surface (0 km) down to 25 km. All calculations were undertaken in an elastic half-space with a model domain of 300 km x 300 km x 25 km and at the full cell resolution. The stress fields were computed for the same impoundment and operational scenarios that were utilized in the elastic deformation calculations. Marked changes in hydrologic loads during impoundment and seasonal operations caused notable variations in the location of the weighted load centroids. These centroids mark the location of the maximum load for a given water level and are an important variable with respect to spatiotemporal changes in the stresses applied on the underlying rocks. The motion of the load centroid can be thought of as a proxy for the changes in the location of where the maximum stresses are applied on the Earth's crust. The load grids for each water level of the impoundment were used to calculate the individual load centroids using a weighted mean center algorithm where the weight of the cell was assigned the water level at that location. The daily water levels for each of the 55 different impoundment scenarios were employed to calculate the accumulated annual load centroid motion for each filling scenario.

Similarly, the daily-accumulated annual weighted load centroid motion was calculated for the five separate operational strategies.

The main driver behind the load centroid motion was the annual, accumulated daily reservoir storage change (both positive and negative) where an increased volume change caused an increase in the motion of the weighted hydrologic load centroid. It was found that the annual operational scenarios with a 590 m starting water level had larger stress regimes as compared to their 622 m water level start counterparts. These differences were attributed to the increased load per unit area for the 590 m data runs. The Coulomb stress from a more condensed seasonal reservoir load was found to be larger than the Coulomb stress as calculated from the same hydrologic load with less load per unit area. Further, there was also an increased load centroid motion for the 590 m water level start scenarios. This was attributed to the increased range of annual water level and areal extent changes as compared to the 622 m water level starts. Marked differences in the Coulomb stresses and load centroid motions were found for the five different operational scenarios. These variations were attributed to the hydrologic load per unit area of the seasonal reservoir loads for each of the annual operations, and, in part to the initial seasonal water level. In other words, a reduction in the seasonal hydrologic load per unit area or an increased initial seasonal water level would likely reduce both the number of cells with notable Coulomb stresses and the accumulated annual centroid motion. The spatial patterns and amplitudes of these stress tensors were closely linked to both the size and timing of GERD inflow/outflow rates, and an improved understanding of the magnitude and extent of these stresses provides useful

information to water managers in order to better understand potential reservoir triggered seismic events from several different operational and impoundment strategies.

The third chapter examined the magnitude of water level changes for all waterbodies > 1 km^2 within the contiguous United States (CONUS) as derived from spaceborne lidar altimeter data products using an automated cluster computing workflow. Here, the mechanisms behind these changes are related to both direct and indirect anthropogenic impacts and are quite diverse across the landscape. A static waterbody mask was used to spatially filter all ICESat-2 (IS-2) photons into their respective spatially overlapping waterbody extents. A dynamic spatial filtering process was then applied on the data such that photons that made it through the initial static spatial filtering process but did not actually fall within regions in which surface water was present during the time of the individual IS-2 granule acquisitions were removed. Outlier photons were removed based on their relationship to the local mean DEM value as well as a bin histogramming technique. The photons were then quantitatively and spatially segmented based on a maximum number of photons in a segment and a ~100 m distance threshold value. Segmented photons were then filtered using a histogram peak and median absolute deviation approach. The segments were then clustered by along-track distance and water level using a density-based spatial clustering of applications with noise (DBSCAN) method. Clusters were removed if they did not meet certain standard deviation and median absolute deviation criteria. The final water level for an individual photon track was determined by the median of all remaining cluster water level values for each of the two beam types ("strong" and "weak"). Finally, relative water level changes from USGS gage data were compared with their temporally and spatially

coincident IS-2 derived counterparts in order to assess the accuracy of the altimeter-based water level changes. An interactive website was created so that interested readers may better understand the spatiotemporal differences in lake and reservoir level changes at this scale. This research was undertaken in order to provide baseline water level monitoring on a much larger scale than is traditionally possible with *in situ* monitoring. Further, knowledge of the accuracy of these remotely sensed spaceborne laser altimeter water level products validates the quality of the IS-2 ATLAS platform for use in future water level monitoring studies.